Development and Application of High-speed and Wide-field Functional Swept Source Optical Coherence Tomography

Yaping Shi

A dissertation

submitted in partial fulfillment of the

requirements for the degree of

Doctor of Philosophy

University of Washington

2025

Reading Committee:

Ruikang K. Wang, Chair

Ivan M. Pelivanov

Ying Zheng

Program Authorized to Offer Degree:

Bioengineering

University of Washington

Abstract

Development and Application of High-speed and Wide-field Functional Swept Source Optical Coherence Tomography

Yaping Shi

Chair of the Supervisory Committee:

Ruiking K. Wang

Department of Bioengineering

Recent advances in optical coherence tomography (OCT) have significantly broadened their utility in biomedical imaging, particularly for the diagnosis and monitoring of vascular-related and microstructural diseases. However, clinical OCT systems remain constrained by limited imaging speed, shallow ranging distance, narrow field of view (FoV), and the lack of robust functional imaging capabilities. These limitations hinder broader *in vivo* clinical applications of OCT. In this study, we develop a high-speed, long-range, wide-field swept-source OCT (SS-OCT) system based on a 600 kHz micro-mlectro-mechanical system vertical-cavity durface-emitting laser (MEMS-VCSEL) laser, designed to deliver high-fidelity morphological and functional imaging. To overcome the depth limitation inherent in conventional k-clock

acquisition, we develop a multi-channel delay sampling technique that splits the analog OCT signal into N-channel time-delayed electrical paths. This method increases the effective k-space sampling density without altering k-clock triggering, thereby doubling the imaging depth without compromising acquisition speed or resolution. To further enhance imaging performance, we introduce the concept of electrical dispersion, which arises from the nonlinear phase response of electronic components operating under high-speed k-clock triggering. A global k-space compensation algorithm is proposed to mitigate this distortion, and a vector field-based distortion correction technique is implemented to restore spatial fidelity in wide-field scans. Together, these methods enable high-quality structural and optical coherence tomography angiography (OCTA) imaging across a lateral FoV of 42 × 42 mm^2 and an extended axial range of 36 mm. To address challenges in imaging samples with complex surface topography, such as the oral cavity, we propose an adaptive contour tracking and scanning strategy. This approach integrates an electrically tunable lens and motorized optical delay line with real-time surface profiling to maintain focus and SNR across curved surfaces. Experimental validation confirms improved image consistency and flow visualization across large and irregularly contoured regions. Finally, we incorporate a novel fiber-based polarization-sensitive OCT (PS-OCT) system based on the platform. To address the instability of the input state of polarization in single-input fiber configurations, we introduce a real-time Stokes vector feedback mechanism that dynamically stabilizes incident circular polarization at the sample surface. This innovation enables reliable birefringence imaging under wide-field and handheld conditions. Together, these system-level advancements result in an OCT platform capable of high-speed, long-range, wide-field, and functionally enhanced imaging. The

proposed system demonstrates significant potential for clinical applications in oral health assessment and other settings requiring comprehensive, real-time evaluation of tissue structure, microvasculature, and optical anisotropy.

ACKNOWLEDGMENTS

First and foremost, I would like to express my deepest gratitude to my advisor, Professor Ruikang K. Wang, for his support and guidance throughout my studies and research. His encouragement, enthusiasm, and profound knowledge have been invaluable to me over the past years. Under his mentorship, I have not only gained extensive knowledge and improved my research efficiency but also learned the essence of conducting meaningful research. I am immensely grateful for the opportunity to learn OCT techniques, and for access to the best resources to explore and advance my work. His patience, dedication, and meticulous revisions of my papers have significantly shaped my academic journey. This work would not have been possible without his continuous support. It has been a great honor to be part of Biophotonics and Imaging Laboratory (BAIL) group.

I am also deeply thankful to the rest of my thesis committee members: Professor Ivan M. Pelivanov, Professor Ying Zheng, and Professor Dan Fu, for their insightful advice, constructive feedback, and continuous support.

I would like to extend my sincere thanks to all my lab mates in the BAIL group. I have learned so much from each of you. Special thanks go to Dr. Qinghua He for his generous guidance and support during the initial stages of my research, to Zhaoyu Gong for helping me integrate into the BAIL group and introducing me to the OCT system and to Yi Zhang for . thoughtful suggestion regarding course enrollment. I would also like to acknowledge Dr. Yiming Lu, Dr. Nhan Lee, Dr. Duo Zhang, Dr. Peijun tang and Dr. Yuandong Li for their technical assistance; Dr. Yuxuan Cheng, Dr. Jie Lu, Dr. Qingqing Zhang, and Zhiying Xie for

their help in the OCT angiography and velocimetry research; and Dr. Jingjiang Xu, Dr. Qingliang Zhao, Dr. Agathe Marnin, Dr., Chao Qing and Dr. Athira B.S. for their collaboration in the polarization-sensitive OCT project. My thanks also go to Sivathanu Kumar, Ahmet Mesut Alpkilic, Shirley Xia, Jorryn Decker Clement, Yanfu Liu, and Milad Lashgari for their friendship and encouragement.

I extend my gratitude to Professor Steve Jacques for his insightful instruction in tissue optics and to Dr. Jian Liu for his invaluable collaboration and support across numerous projects.

I am grateful to the University of Washington for providing me with the platform and resources to pursue my research. I would also like to thank the staff of the Graduate School and the Department of Bioengineering for their technical support and helpful suggestions.

Finally, I would like to express my deepest gratitude to my family, particularly my beloved wife Guangxia Feng, for their unwavering encouragement and spiritual support throughout this journey. Without their belief in me, none of this would have been possible.

TABLE OF CONTENTS

LIST OF FIGURES

LIST OF TABLES

INTRODUCTION

1.1 Significance and Research Motivation

Optical Coherence Tomography (OCT) is a non-invasive imaging technique that visualizes tissue microstructures by measuring the echo time from different sample layers with micrometer-level resolution[1,2]. Since its inception, OCT has undergone significant advancements, evolving from time-domain to spectral-domain configurations, and more recently, to the swept-source OCT (SS-OCT) [3–6]. SS-OCT uses wavelength swept lasers and high-speed analog to digital conversion to achieve faster speeds and longer imaging ranges than spectral domain OCT. Optical coherence tomography angiography (OCTA) and polarization sensitive OCT (PSOCT), as functional extension of OCT (OCTF), provides detailed vascular and tissue specific information without the need for contrast agents[6,7]. These technological innovations have firmly established OCT/OCTF as an essential tool in various biomedical imaging applications, including ophthalmology [8–10], dentistry [11–13], dermatology [14–18], endoscopy [19–23], neuroscience [24–27] and others[28,29].

Recent advancements in OCT/OCTF have demonstrated great potential in biomedical imaging, particularly for diagnosing and monitoring vascular-related diseases[2,26,30]. Despite this progress, clinical OCT systems are limited by imaging speed, depth range, and field of view (FoV), which restricts their broader application in clinical settings[31,32]. High-speed OCT systems offer several key advantages that make them particularly valuable in medical diagnostics [33]. The increased imaging speed reduces acquisition time, which is critical in minimizing motion artifacts caused by patient movement. This is especially important in *in vivo*

biomedical applications like ophthalmology and endoscopy, where even slight movements can compromise image quality[33,34]. High-speed imaging also enables real-time volumetric scanning, allowing clinicians to perform three-dimensional assessments of tissue structures with greater efficiency and precision[35]. This capability enhances the diagnostic potential of OCT by providing comprehensive structural information in a shorter time frame, facilitating faster decision-making in clinical environments.

A large FoV further amplifies the utility of high-speed OCT systems. In clinical practice, small FoV probes require clinicians to manually scan over tissue areas, increasing the risk of missing diagnostically relevant regions, especially in complex anatomical structures such as the retina, skin, or oral cavity [11,36,37]. With a larger FoV, a single scan can capture a broader area, reducing the need for multiple scans and stitching together smaller images, which can lead to misalignment or gaps in data. The ability to capture a large area in one scan is particularly advantageous in dermatology, where wide regions of skin need to be examined, or in ophthalmology, where a large retinal area must be visualized for comprehensive analysis of conditions like diabetic retinopathy or age-related macular degeneration.

Additionally, the combination of a wide FoV and long ranging distance expands the applicability of OCT to areas with complex topographies. For instance, in oral imaging, the uneven surface of the oral cavity demands a system with a long-ranging distance (typically >20 mm) to capture both superficial and deeper structures without sacrificing image quality[38,39]. A long ranging distance ensures that detailed images of both shallow and deep tissue layers can be obtained in a single scan, enhancing diagnostic accuracy. In settings like facial and orthopedic imaging, where tissue structures may vary in depth, this feature allows for better

visualization of subsurface abnormalities that might otherwise be missed with standard OCT systems[31,40].

Finally, as OCT advances toward functional imaging, including vascular, metabolic, and polarization-based contrast, system demands increase further. Modalities such as PS-OCT require precise control of the input state of polarization (SOP), which is particularly challenging in fiber-based, handheld, or wide-area scanning probes. Maintaining consistent polarization fidelity across large scan areas and dynamic environments is necessary for reproducible and accurate functional measurements.

Thus, the development of OCT systems that simultaneously deliver high speed, extended ranging distance, wide field of view, and functional imaging capabilities is essential for broadening their clinical utility. Such systems not only enhance diagnostic precision and operational efficiency but also reduce patient discomfort by minimizing scan duration and repeat procedures. These improvements are particularly valuable in real-time imaging of complex anatomical structures and microvascular networks, where rapid and comprehensive visualization is critical for early diagnosis and treatment planning. However, current OCT/OCTF technologies continue to face significant limitations when attempting to integrate all four performance dimensions into a single platform. Advancements in speed often come at the expense of depth or polarization stability, and wide-field functional imaging introduces additional challenges in optical alignment, SOP control, and signal processing bandwidth. For example, achieving both high-speed acquisition and deep imaging requires broader k-clock bandwidth to match the swept laser's nonlinear tuning profile, which often exceeds the capabilities of existing digitizers and interferometric clocks. Furthermore, implementing

polarization-sensitive modalities like PS-OCT within compact fiber-based systems is hindered by input SOP variability, especially during handheld or large-area scanning. Addressing these multifactorial challenges requires coordinated innovations in optics, electronics, and signal processing. This thesis responds to that need by developing an integrated suite of methods to enable OCT systems capable of high-speed, deep-range, wide-area, and functionally robust imaging, thereby advancing OCT toward a more comprehensive and clinically deployable diagnostic technology.

1.2 Technology Background: Optical Coherence Tomography

Optical coherence tomography enables high-resolution tomographic imaging in the depth direction by utilizing low-coherence interference, measuring the echo time of infrared light reflections from various layers of tissue or materials. By scanning across the sample, OCT reconstructs three-dimensional images, providing valuable insights into the internal structure of biological tissues and materials.

The core components of OCT systems include a broadband light source, a Michelson interferometer, and a photodetector. The axial resolution of OCT is determined by the coherence length of the broadband light source, typically achieving resolutions of 1–10 μm. In contrast, the lateral resolution, which is independent of axial resolution, depends on the focused spot size within the sample and is generally on the micron scale.

OCT offers several advantages, including non-contact imaging, rapid acquisition speeds for real-time dynamic imaging, and high sensitivity. These attributes make OCT a unique imaging modality, filling a crucial gap in the field of biomedical imaging by providing micron-level

resolution at millimeter-scale depths. OCT has been widely adopted in clinical diagnostics, therapeutic monitoring, and various research fields.

Over the years, two main types of OCT systems have been developed: time-domain OCT (TD-OCT) and Fourier-domain OCT (FD-OCT). Despite their differences in implementation, both systems operate based on the same fundamental principle—low-coherence interferometry. In both TD-OCT and FD-OCT, the echo time of light reflected from different tissue layers is measured to generate high-resolution depth-resolved images. However, the methods they employ to extract this information differ, resulting in varying performance in terms of speed and resolution.

1.2.1 Principle of time domain OCT

Time-Domain OCT (TD-OCT) is the first-generation OCT technique and operates similarly to ultrasound imaging, though it uses light waves instead of sound waves [41,42]. While ultrasound detects reflected sound waves, TD-OCT detects backscattered light. Since the speed of light is too fast to be measured directly like sound, TD-OCT leverages the principle of low-coherence interferometry to detect backscattered signals from the sample[43].

The aim of TD-OCT is to interpret the amplitude and phase of light scattered from different positions both on the surface and within the sample. To achieve this, TD-OCT scans either in space or time to capture reflected or scattered light from various depths in the sample[44]. A typical schematic of a time-domain OCT system is shown in Figure 1-1. The light from a low-coherence broadband source is split into two beams by a beam splitter: one directed towards the sample arm and the other towards the reference arm. When the optical path difference

between the sample and reference arms is smaller than the coherence length of the light source, the two beams interfere when recombined at the beam splitter. This interference signal is then detected and collected by a single-point detector.

The coherence length of low-coherence light sources typically ranges from a few microns to tens of microns, allowing for micron-level axial resolution in TD-OCT. This enables highly detailed depth-resolved imaging of tissues and structures within biological samples.

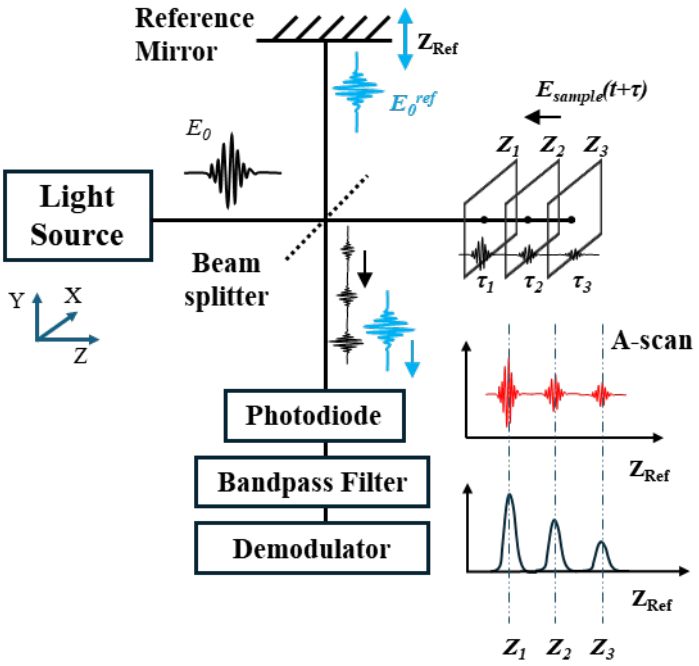

Figure 1-1. Schematic diagram of a typical time domain optical coherence tomography

1.2.2 Mathematical interpretation

Assuming that the reference mirror is ideal, and the beam splitter has reference and sample arm intensity transmittance T_r and T_s, respectively. Assume the electric field coming out of the light source $E_{in}(\omega, t)$ as a complex exponential plane wave[5,45]:

$$E(w,t) = s(w)\,exp[-i(wt+kz)] \tag{0-1}$$

where *s(ω)* is the source field amplitude spectrum, *ω* is the frequency, *t* is the time variation, *k* is the wavenumber, and *z* is the distance. Let the initial phase of the electric field from light source equal to zero. The electric field at the detector from reference arm and sample arm could be written as follows:

$$E_r(w,t,\Delta z) = \sqrt{T_r T_s}s(w)e^{-i(wt+\varphi(\Delta z))} \tag{0-2}$$

$$E_s(w,t) = \sqrt{T_r T_s}s(w)\,e^{-iwt}\cdot H(w) \tag{0-3}$$

where $\phi(\Delta z)$ is the phase accumulated resulted from reference mirror translation motion a distance, $\Delta z = \Delta t c/n_{air}$.

$$\phi(\Delta z) = \frac{2wn_{air}\Delta z}{c} \tag{0-4}$$

where Δt is the corresponding optical time of flight difference and as usual, *c* represents the speed of light in vacuum. n_{air} is the group refractive index of air. The factor, 2, arises from the round trip of light in the interferometry. $H(\omega)$ is the sample response function that describes the overall reflection from all structures distributed in the *z* direction within the sample.

$$H(w) = \int_{-\infty}^{+\infty} r(w,z)e^{i2n(w,z)wz/c}\,dz \tag{0-5}$$

where the function *r(ω, z)* is the backscattering coefficient of the structural in sample, and *n(ω, z)* is the frequency-dependent, depth-varying group refractive index. The exponential term explains the phase accumulated.

Then the overall electric field in the detector should be the summation of light from reference and sample arm.

$$E_{out}(w,t,\Delta z) = E_r(w,t,\Delta z) + E_s(w,t) \quad (0\text{-}6)$$

The detection of the interference signal is a time-average of electric field sum, express as:

$$I(w,\Delta z) = \langle |E_r + E_s|^2 \rangle = \langle E_r E_r^* \rangle + \langle E_s E_s^* \rangle + 2\Re\{\langle E_s E_r^* \rangle\} \quad (0\text{-}7)$$

where $\langle\ \rangle$ denotes time averaging and R denotes real part. The first two terms can be identified as "self-interference", whereas the last term is the real part of the complex "cross-interference". Substituting equation (1-2) to equation (1-6) into equation (1-7) obtains:

$$I(w,\Delta z) = T_r T_s S(w) + T_r T_s S(w)|H(w)|^2 + 2T_r T_s \Re\{S(w)H(w)e^{i\phi(\Delta z)}\} \quad (0\text{-}8)$$

where the S(w) is the power spectrum of the source field amplitude spectrum. The first two terms are result of self-interference, and it can be eliminated by a balanced detector that differentiates the in-phase and quadrature signals. By doing so it will double the value of the "cross-interference" term, increasing the signal-to-noise ratio (SNR) by about 3 dB. So, we ignore the DC term and analyze the cross term in detail. To be simple, assuming the $T_r = T_s = 0.5$, the cross-interference term of equation (1-8) could be expressed as:

$$\Gamma(\Delta z) = \frac{1}{2}\int_{-\infty}^{+\infty} H(w)S(w)\, cos\{\phi(\Delta z)\}\, dw \quad (0\text{-}9)$$

The time-domain OCT system uses the optical delay line to change the optical length of the reference arm to realize the axial scanning (A-scan) of the OCT. The interference signal of an A-scan could result in the depth information, as shown in Figure 1-1. On this basis, one-

dimensional and two-dimensional scanning is introduced into the sample arm to realize real-time two-dimensional imaging and three-dimensional volume imaging.

1.2.3 OCT specifications

According to equation (1-9), the depth information of OCT imaging is obtained by the cross-correlation term, which is expressed as the coherence function deconvolving the reflectance at different depths of the sample, so the axial resolution of the system is determined by the coherence function. Assuming that the light source spectrum is Gaussian, the axial resolution of the system is the full width at half maximum (FWHM) of the coherence function [5]:

$$\Delta l = \frac{2\,ln\,2}{\pi}\frac{\lambda_0^2}{\Delta\lambda} \tag{0-10}$$

where λ_0 is the center wavelength, and $\Delta\lambda$ is the spectral FWHM. Typically, a SLD source with a center wavelength $\lambda_0 = 820$ nm and spectral FWHM $\Delta\lambda = 20$ nm, has a theoretical axial resolution of ~ 15μm. The lateral resolution of an OCT system is determined by the Rayleigh spot size of the sample arm objective, which is affected by the spot size and the focal length of the scanning lens.

$$\Delta x = \frac{1.22\cdot\lambda_0}{2\cdot NA} = \frac{1.22\cdot\lambda_0\cdot f}{D} \tag{0-11}$$

Where *NA* represents the numerical aperture of the scanning lens, *f* and *D* are the focal length and diameter of the lens respectively. From the equation, when the laser is selected the lateral resolution could be improved by increasing beam diameter of the scanning beam and using a scanning lens with shorter focal length.

Although the axial and lateral resolution of OCT are decoupled, there is a constraint between the lateral resolution of the system and the depth of focus, which is usually defined as twice the Rayleigh distance:

$$b = \frac{\Delta x^2}{\lambda_0} \tag{0-12}$$

When an objective lens with a larger focal length (large NA) is selected, the lateral resolution of the system will increase accordingly, but the depth of focus will decrease, and the lateral resolution will decrease faster beyond the range of the focal depth, which limits the range to obtain clear image.

SNR of OCT is a key parameter, and it is the ratio between the signal power (square of the detector photo current) and the noise power. SNR can be written as[46]:

$$SNR = \frac{\eta \cdot P_{source}}{q_e \cdot B} \tag{0-13}$$

where η represents the detector quantum efficiency, P_{source} is the light source power, q_e is the photon energy, and B is the noise equivalent bandwidth that is determined by detector integral time and detector bandwidth.

1.2.4 Fourier domain OCT

Fourier domain optical coherence tomography extracts depth-resolved information from the sample tissue by detecting spectral interference fringes [1]. With advancements in light source and detection technologies, FD-OCT, which includes spectral-domain OCT and swept-source OCT, offers significant advantages in sensitivity and imaging speed [46]. It has become the

mainstream in OCT community, enabling functional imaging applications such as OCT angiography [47].

In FD-OCT, the interference signal is measured in the frequency domain. Each spectral component of the interference signal is recorded separately, and a depth-resolved image is reconstructed using a Fourier transform [48]. There are two primary methods for recording spectral data in FD-OCT: spectral-domain and swept-source. Their basic configurations are illustrated in Figure 1-2(a) and (b), respectively.

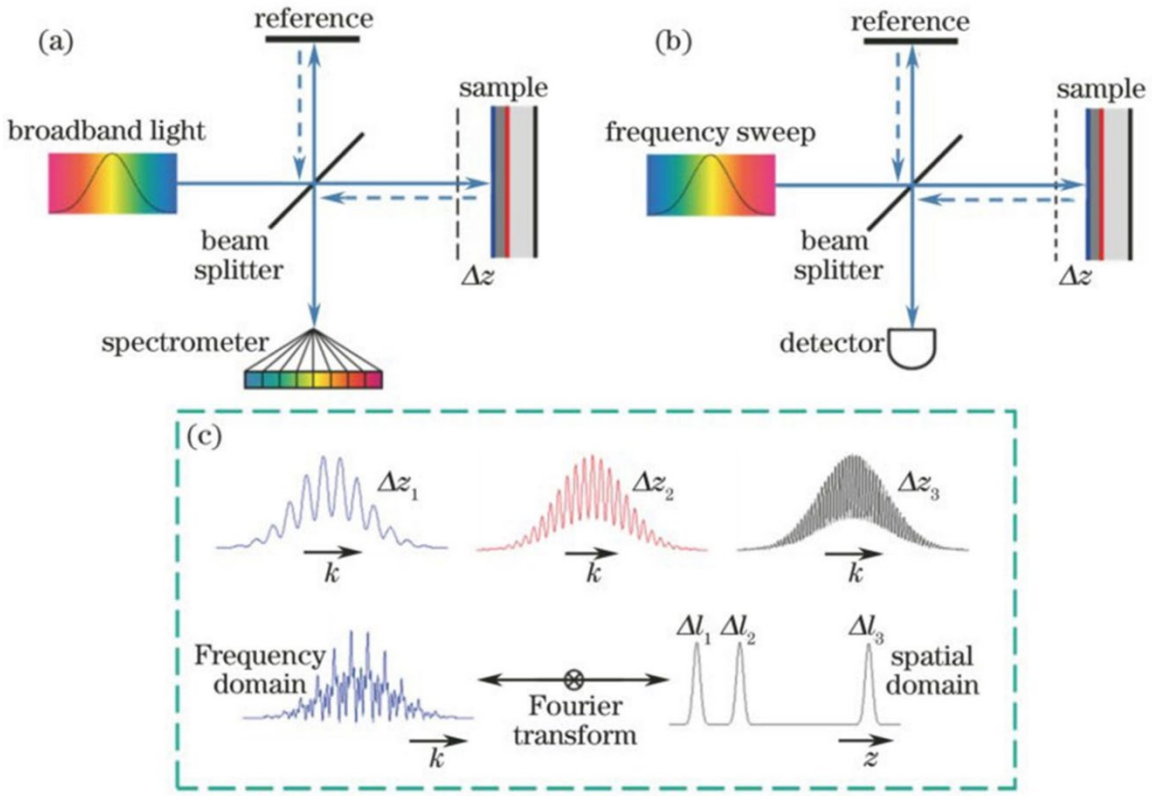

Figure 1-2. Schematic diagram of FDOCT detection. (a) Spectral detection; (b) Swept source detection; (c) Signal reconstruction from frequency domain to spatial domain.

In spectral-domain OCT, a broadband light source illuminates the sample, and a spectrometer disperses the spectral components spatially. These components are recorded in

parallel by a high-speed line array camera[49]. In contrast, swept-source OCT uses a wavelength-tunable light source [50], where the spectral components are dispersed temporally. As a result, they can be recorded sequentially with a single-point detector. Despite the differences in how spectral data are recorded, the signal reconstruction process in both methods is the same, as shown in Figure 1-2(c). The interference fringes corresponding to different depths $\Delta z1$, $\Delta z2$, and $\Delta z3$ are Fourier transformed in the frequency domain to retrieve spatial depth information. Since the mathematical derivation for FD-OCT closely parallels that of time-domain OCT, we omit further mathematical details here.

1.2.5 Advantages and disadvantages of FD-OCT

FD-OCT offers significantly faster imaging speeds compared to time-domain OCT [48,50]. In TD-OCT, depth information is obtained through point-by-point scanning of the reference arm, a mechanical process that severely limits imaging speed. In contrast, FD-OCT uses spectral detection to capture depth information in parallel, effectively performing progressive scanning and thus greatly enhancing imaging speed. For spectral-domain OCT, imaging speed is primarily determined by the line scan rate of the camera in the spectrometer, while in swept-source OCT, it depends on the sweep rate of the light source.

Another major advantage of FD-OCT is its high signal-to-noise ratio (SNR) compared to TD-OCT [49,51]. To facilitate comparison, consider three systems, SD-OCT, SS-OCT, and TD-OCT, with the same light source power, pixel number ($M/2$ pixels in the Z direction), and imaging speed (identical line scan rate, meaning the same axial scan time t). FD-OCT generally requires M channels for signal acquisition, which is significantly more than TD-OCT. As a

result, the SNR in FD-OCT is approximately *M/2* times higher than that in TD-OCT, primarily due to the parallel detection in the axial direction, which increases the integration time for each point by the same factor.

Sensitivity is the most significant advantage of FD-OCT over TD-OCT [51,52]. In FD-OCT, the spectra acquired must undergo a Fourier transform to generate a depth-resolved image, which introduces an averaging effect that further enhances SNR. For an A-scan with *N* pixels, the SNR improves by a factor of *N/2*. In SD-OCT, a 10-bit digitization per pixel achieves a dynamic range of 40-60 dB for an A-line, while the detection remains well below the saturation limit. Research has shown that the noise floor in SD-OCT is approximately 5.7 dB lower than in TD-OCT when using the same interferometer but different detection methods [1]. In SS-OCT, although relative intensity noise (RIN) is higher than in SD-OCT, balanced detection can effectively suppress it, allowing SS-OCT to achieve comparable SNR to SD-OCT.

Although FD-OCT offers significant advantages in imaging speed, SNR, and sensitivity, its sensitivity diminishes with depth, a phenomenon known as sensitivity roll-off [48,53]. In SD-OCT, this roll-off is due to the inability to accurately measure high-frequency modulation of the detected spectrum, which is affected by both the finite pixel size of the camera array and the spectrometer's limited spectral resolution. As a result, SD-OCT experiences a dramatic sensitivity drop (tens of decibels) at maximum depths, leading to blurred signals at long optical delays. In SS-OCT, sensitivity roll-off is influenced by the instantaneous linewidth of the light source and the detection bandwidth of the photodiode and digitizer. Advanced swept-source technologies, such as MEMS-VECSL, achieve narrow instantaneous linewidths, allowing for coherence lengths exceeding 1 meter [34,54,55].

Another drawback of FD-OCT is the occurrence of conjugate images [56,57]. Since FD-OCT records real-valued interference spectra, the Fourier transform of these signals produces conjugate images. This reduces the usable imaging depth to half, limiting the effective imaging range compared to TD-OCT.

Despite these limitations, FD-OCT, particularly SD-OCT, offers superior phase stability, which makes it ideal for phase-sensitive measurements [58,59]. These measurements are crucial for applications such as Doppler OCT, OCT elastography, and polarization-sensitive OCT. In phase-sensitive detection, axial motion can be quantified by measuring phase differences between corresponding points at the same depth in adjacent A-lines. This technique is also valuable for phase contrast microscopy and calculating phase retardation in polarization-sensitive OCT.

Compared to TD-OCT and SD-OCT, SS-OCT is increasingly becoming the preferred configuration due to its superior sensitivity roll-off performance, longer achievable imaging ranges, and higher imaging speeds [50]. However, SS-OCT faces challenges in phase-sensitive detection due to limitations in wavelength sweep repeatability and significant jitter in spectrum acquisition [60].

1.3 The Development of High-speed and Wide Field OCT

1.3.1 High-speed OCT

Imaging speed is a critical parameter that defines the performance of OCT systems [61]. Driven by advances in both technology and hardware, OCT imaging speed, typically measured in depth

scans per second (A-scans per second), has increased significantly, from several hundred hertz to kilohertz and even into the megahertz range [61,62]. To date, time-domain OCT was only capable of imaging speeds up to ~8,000 A-lines per second [63], mainly constrained by the use of a mechanically scanning mirror in the reference arm to obtain depth-resolved information. This relatively slow speed has limited its applicability, particularly in clinical *in vivo* 3D imaging where faster acquisition is crucial [5].

The development of Fourier-domain OCT marked a significant advancement in imaging speed compared to TD-OCT, as it eliminates the need for mechanical scanning in the reference arm [48,64,65]. FD-OCT comes in two primary variants: spectral-domain OCT and swept-source OCT. SD-OCT uses a broadband light source, such as a super-luminescent diode, along with a spectrometer to capture optical interference signals. However, its imaging speed and depth range are restricted by the limitations of the spectrometer. Current SD-OCT systems have achieved A-line rates as fast as 312 kHz, though at the cost of reducing the imaging range to approximately 2 mm [66]. Innovative approaches such as line-scan and full-field OCT systems have achieved ultra-high A-scan rates, reaching the megahertz range, by employing parallel acquisition techniques using 2D cameras [42,67,68]. However, these methods are not confocal, resulting in different image quality compared to standard OCT systems [68,69]. Consequently, they have not yet fully replaced conventional OCT systems in practice.

SS-OCT utilizing wavelength-swept lasers and high-speed analog-to-digital conversion, enables faster imaging speeds and longer imaging ranges than SD-OCT [22]. The performance of SS-OCT systems largely depends on the characteristics of the swept-source laser. Over the past few decades, various types of swept lasers have been developed to achieve ultra-high A-

scan rates, including short cavity lasers, Fourier domain mode-locked lasers (FDMLs) [70–72], dispersion-tuned lasers [73], amplified spontaneous emission sweepers (ASE), stretched pulse lasers [74,75], and MEMS-VCSELs [22,76]. Among these, FDML, stretched pulse, and MEMS VCSELs dominate high-speed OCT systems. FDML lasers have demonstrated A-scan rates in the tens of MHz by using multiple buffered sweeps, and commercial FDML systems are available with rates up to 3.5 MHz using 8X buffered sweeps [22]. While FDML lasers offer high sweep speeds, they are complex and difficult to miniaturize due to the requirement for kilometer-length fiber spools, optical amplifiers, and active polarization control [77]. Stretched pulse lasers operate at tens to hundreds of MHz A-scan rates, and they eliminate sweep-to-sweep variability. However, their coherence lengths are limited, and adjusting sweep rates is challenging because the rate is determined by the optical fiber length. MEMS-VCSEL technology, on the other hand, offers compelling advantages for SS-OCT implementation. VCSELs can be configured to achieve adjustable, multi-MHz A-scan rates without the need for sweep multiplexing [78,79]. The sweep rate and range are tunable, allowing the system to support different A-scan rates, resolutions, and imaging ranges, depending on the digitization rate of the analog-to-digital converter (ADC). This flexibility, combined with low cost, has made MEMS-VCSELs widely adopted in both research and clinical OCT devices. Commercially available MEMS VCSELs currently dominate high-performance OCT devices, offering imaging speeds up to 400 kHz under flexible configurations.

Currently many SS-OCT systems have demonstrated A-scan rates in the megahertz range, with imaging speeds exceeding 200 kHz and proven OCT imaging capabilities in research setting [34,61,79,80]. However, a common limitation is their constrained imaging depth,

typically restricted to less than 10 mm. This limitation arises from several factors, including insufficient coherence length of the swept laser source, limited electrical bandwidth of the analog-to-digital converter (ADC), and the need to maintain sufficient axial resolution over larger imaging depths. The challenge of balancing high-speed operation with deep imaging range remains a key area of focus in the ongoing development of SS-OCT systems.

1.3.2 Wide field OCT

In OCT imaging, the field of view (FoV) typically refers to the lateral area covered during 3D imaging [5]. A wide FoV is critical for providing coverage of larger tissue areas without sacrificing depth or imaging quality. The OCT FoV is influenced by several factors, including optical design, scanning mechanism, and, most importantly, imaging speed. As OCT technology has evolved from time-domain to Fourier-domain systems, the FoV has expanded significantly. Early OCT systems were limited to a small FoV due to the slow imaging speed of time-domain OCT. However, with the advent of Fourier-domain OCT, the imaging speed has increased substantially, allowing for larger FoVs, typically up to 10 by 10 mm.While this FoV is adequate for many applications, such as retinal and skin imaging, certain clinical scenarios require even larger areas to be examined, including cases of retinal and choroidal diseases [36], anterior eye imaging [79], skin assessments [37], and dental evaluations [13].

Wider FoV OCT imaging can be achieved either in a single scan or through mosaicking [31,81,82], where multiple individual scans are stitched together during post-processing. Acquiring a wider FoV in a single scan often requires longer scanning times to maintain sufficient scan density, which is crucial for high-quality imaging, particularly for OCT

angiography. This necessitates a high imaging speed to reduce the impact of uncontrollable motions, such as heartbeat, breathing, or micro-saccades, and sufficient imaging range to accommodate optical path length variations or uneven surfaces [34,36]. Additionally, field distortion and aberration must be addressed to ensure accurate imaging results [8].

Mosaicking, on the other hand, offers a wide FoV without extending the imaging range, by combining high-quality single scans [11,83]. However, this approach increases the overall measurement time and requires sufficient training to ensure accurate realignment. In addition, post-processing becomes more complex and time-consuming [84], as each scan volume must be translated, rotated, and aligned in three dimensions to ensure proper registration [85]. With recent advancements in imaging speed and optical design, wide-range scans exceeding 20 x 20 mm are now feasible. Current SS-OCT devices in ophthalmology can achieve single-scan coverage of up to 23 x 20 mm on the retina, and by mosaicking 4-5 scans, areas as large as 31 x 27 mm [86] can be visualized, enabling reliable evaluation of peripheral retinal conditions. These systems, however, typically operate at 100 kHz, which extends scanning time and degrades imaging quality due to patient motion, particularly in individuals who has difficulty to maintain steady eye fixation.

Beyond retinal imaging, OCT systems with centimeter- and meter-scale FoVs have been developed, capable of imaging areas larger than 20 by 20 cm [31,87]. Despite this promise, these systems face challenges in maintaining sufficient scan density or reducing imaging time due to relatively low A-line rates (~100 kHz), which restricts their ability to provide functional *in vivo* imaging in clinical settings, limiting them to morphological assessments.

1.3.3 Functional OCT and polarization-Sensitive OCT

While conventional optical coherence tomography (OCT) provides high-resolution structural imaging based on scattering contrast, the demand for richer diagnostic information in clinical and biological contexts has driven the development of functional OCT techniques. Functional OCT extends the utility of the OCT signal by analyzing additional physical properties of the tissue, such as flow, birefringence, absorption, and polarization state, beyond mere intensity. These modalities can reveal physiologically or pathologically relevant tissue parameters that remain inaccessible through structural OCT alone.

Among the diverse range of functional OCT technologies, Doppler OCT quantifies flow velocity by detecting phase shifts between sequential A-lines, enabling the visualization of microvascular networks or dynamic perfusion. Optical coherence angiography (OCTA) further exploits motion contrast from repeated scans to segment perfused vasculature noninvasively. Other extensions include spectroscopic OCT for molecular contrast and polarization-sensitive OCT (PS-OCT) for mapping tissue birefringence.

PS-OCT is particularly compelling for biomedical applications due to its ability to detect optical anisotropy, which arises from organized microstructures such as collagen, keratin, and muscle fibers. This modality enables noninvasive assessment of fibrous tissue integrity and orientation, offering clinical value in ophthalmology, dermatology, cardiology, and dentistry. PS-OCT systems typically extract Stokes vectors or Jones matrices across depth to reconstruct local birefringence, degree of polarization uniformity (DOPU), and optic axis orientation.

Initial PS-OCT implementations were largely based on free-space optics with bulk polarization control elements (e.g., quarter-wave plates, polarizing beam splitters) and multiple detection channels. These systems offered full access to the polarization states of incident and backscattered light, facilitating precise birefringence measurement. However, they suffered from alignment instability, large form factors, and poor adaptability to *in vivo* or handheld settings.

With the increasing push toward compact and clinical-use devices, fiber-based PS-OCT systems have gained prominence. These use polarization-maintaining (PM) or single-mode fiber links to guide light between system components and the sample. Compared to free-space configurations, fiber-based PS-OCT enables greater mechanical flexibility, portability, and potential for miniaturization. However, this shift introduces new complications. Recent advances in PS-OCT aim to combine the advantages of fiber-based portability with robust polarization characterization, enabling wide-field, high-speed, and functionally rich imaging

1.3.4 Challenges in high-speed and wide field functional OCT

High-speed functional OCT with a wide field of view holds immense promise for expanding the utility of OCT across clinical and industrial applications, especially in scenarios demanding large-area and rapid imaging. However, integrating high-speed performance, extended imaging depth, and wide-area functional coverage in a single OCT platform remains challenging due to several technical challenges.

The first challenge arise from the limited axial imaging range in high-speed swept-source OCT systems. As the A-line rate increases, the number of k-clock samples per sweep often

becomes sparse, especially in systems using external k-clock triggering. This leads to a reduced effective sampling rate and consequently a shallow imaging depth, often insufficient for applications involving curved or thick tissue structures. Enhancing one aspect, such as speed, often results in trade-offs, such as reduced imaging depth or compromised resolution. Addressing this limitation requires a method to enhance the sampling density without reducing acquisition speed or compromising spectral linearity.

The second challenge involves the nonlinear phase response and limited analog bandwidth of the digitizer and downstream electronics, which become prominent under high-speed and wide-field acquisition protocols. These issues introduce electrical dispersion, a form of nonuniform k-space distortion that accumulates across the field of view. As a result, structural images suffer from spatial distortion, and subtle features may be misrepresented or aliased. This is particularly evident when imaging large or highly curved anatomical regions, such as the oral cavity, where accurate geometric representation is crucial for diagnosis or quantitative assessment..

The third challenge is associated with imaging surfaces that exhibit large curvature or uneven topology. In such cases, the depth of field becomes insufficient to maintain lateral focus across the entire FoV. Combined with the natural sensitivity roll-off of OCT systems, this leads to localized degradation in image resolution and signal-to-noise ratio. When scanning across highly contoured surfaces, such as dental arches, facial skin, or surgical cavities, this challenge limits both structural and functional imaging fidelity.

The fourth challenge emerges in the context of fiber-based polarization-sensitive OCT systems, particularly those with single-input configurations aimed at compact, handheld, or wide-field operation. In these setups, the SOP of the incident beam can vary unpredictably due to mechanical perturbation of the fiber. These SOP fluctuations degrade the accuracy of birefringence measurements and reduce repeatability, especially under dynamic or handheld imaging conditions. Ensuring SOP stability across a wide FoV in real-time requires dedicated feedback or compensation mechanisms, which have been historically difficult to implement in fiber-based systems.

1.4 Scope of the thesis

The objective of this thesis is to address the challenge of integrating high-speed acquisition, extended imaging depth, wide FoV, and functional contrast into a swept-source OCT platform suitable for clinical deployment. The research spans optical, electrical, and algorithmic innovations to overcome the four key limitations outlined in the previous section.

Chapter 2 addresses the challenge of shallow imaging depth in high-speed swept-source OCT systems, where sparse k-clock sampling at high A-line rates limits the axial range. To overcome this, a multi-channel delayed sampling strategy is proposed. By splitting the analog interference signal into multiple delayed electrical channels and resampling them in k-space, the effective sampling rate is increased without reducing system speed. This approach extends the imaging depth while preserving signal integrity and enables large-volume imaging in a single sweep.

Chapter 3 tackles the issue of electrical dispersion and geometric distortion encountered in high-speed, wide-field OCT imaging. The nonlinear response of analog components and limited digitizer bandwidth distort the spectral content of the OCT signal, especially in the periphery of large scans. A global k-space compensation framework is developed to correct this electrical dispersion, and a vector field mapping algorithm is introduced to restore spatial fidelity across the field of view. This enables distortion-free structural imaging of complex anatomical regions such as the oral cavity.

Chapter 4 is devoted to resolving the imaging degradation caused by uneven surface topology. In wide-field scanning of curved or contoured samples, the fixed focus depth and system sensitivity roll-off lead to resolution loss and signal dropouts. To mitigate this, an adaptive contour-tracking and scanning method is implemented. This method dynamically adjusts the scanning trajectory based on estimated surface geometry, maintaining optimal focus and high-quality imaging across variable sample heights. The technique is validated on dental arches and other non-planar structures.

Chapter 5 responds to the limitation of polarization instability in single-input fiber-based PS-OCT systems, especially under wide-field or handheld scanning conditions. A novel real-time surface Stokes feedback mechanism is introduced, which dynamically monitors and corrects the incident SOP at the sample interface. By ensuring stable circular polarization delivery, the system achieves reliable birefringence imaging in compact fiber-based configurations. This development paves the way for functional OCT imaging with minimal hardware complexity.

Chapter 6 concludes the thesis by summarizing the key contributions, evaluating their integration potential in clinical OCT systems, and proposing directions for future research, including improved polarization calibration, GPU-based real-time processing, and compact handheld device implementation.

2 MULTI-CHANNEL DELAY SAMPLING TO EXTEND IMAGING DEPTH IN HIGH-SPEED SWEPT-SOURCE OCT SYSTEMS

2.1 Background and Motivation

Optical Coherence Tomography (OCT) is a non-invasive imaging technique that enables the visualization of tissue microstructures with micrometer-level resolution [1,47]. Over the last two decades, OCT has undergone evolution from time-domain OCT to spectral-domain OCT and swept-source OCT (SS-OCT). Today, SS-OCT, with its faster speed and higher sensitivity over longer ranging distance, has become a mainstream technology widely utilized in various fields, including ophthalmology [2,88,89], cardiology [90,91], and dermatology [18,92]. The SS-OCT system typically employs a laser source based on the vertical-cavity surface-emitting laser (VCSEL) to generate a series of continuously changing wavelengths with a specific spectral content and bandwidth. However, the depth information of the sample is a function related to the wave number (k), with the depth profile corresponding to the wavenumber (k) forming a Fourier transform pair. To obtain the sample's depth information, it is essential to convert the interference signal into a function of the wave number k (referred to as a k-space function) before performing Fourier transformation [55,93].

SS-OCT achieves a linearized k-space interference signal mainly using two methods: internal clock acquisition and k-clock-triggered acquisition. The internal clock acquisition method involves the use of an internal clock to uniformly sample the time domain interference signals of interest and a reference signal generated by an auxiliary Mach-Zehnder

interferometer (MZI). The interference signal of interest is calibrated and resampled using the MZI signal [22,94]. However, the resampling process inevitably introduces signal distortion, especially at longer ranging distance, leading to a reduction in system's sensitivity. Additionally, this method significantly increases the volume of acquired dataset, necessitating high-speed capabilities from the data acquisition card [87,95].

The k-clock triggering acquisition method involves the generation of a k-clock signal by the MZI to trigger the acquisition of interference spectrum [96]. Photodetectors convert the MZI signals into electrical signals. The electrical signals pass through a "zero-crossing detector," generating a k-clock trigger signal at the positions where the signal crosses zero. Then the k-clock trigger signal is used to trigger the acquisition of the OCT signal. This result in the generation of a digitized interference signal of interest that exhibits linearity in k-space and is not distorted. The k-clock triggering acquisition method eliminates the need for resampling interference spectrum signals of interest, reducing the burden on the acquisition card and simplifying post-data processing.

Nevertheless, this method is constrained by the speed of the MZI acquisition card and the zero-crossing detector [97]. If the sweeping speed of the swept-source is too fast, the k-clock trigger signals allocated to each spectrum would be sparse, leading to a shallow imaging depth. Therefore, there's a trade-off between imaging speed and depth due to this constraint. This limitation contradicts the desirable features demanded by a clinical imaging system. Clinical imaging often demands a system with 1) a faster scanning speed, aiming to reduce total imaging time for improved patient compliance [98,99], and 2) a longer ranging distance to handle complex scenarios where the target of interest exhibits significant height differences and

curvature within the field of view. Consequently, there is a demand for OCT systems to possess both high acquisition speed and long ranging capabilities [60,100].

Here we introduce a multi-channel delay data sampling method aimed at extending the imaging depth of high-speed SS-OCT systems. The interference signals are first captured by the balanced detector and become electrical signals. The electrical signal is then split into N channels, with each channel having a fixed time delay that is realized by the length of the electrical cables used, which are then digitized by the N-channel data acquisition card. With this treatment, however, the time delay would introduce non-uniform phase shifts in wavenumber for the signals formed by different wavelengths because the light source is broadband, leading to inconsistent k-clock offsets at different sampling points. To mitigate this electrical dispersion, a calibration procedure is employed to calculate the k-shift for each sampling point. After calibration for each channel, the N-channel signals are combined and resampled to achieve a linearized spectrum in k-space as if the sampling rate were N-times that of a single channel digitization. This approach would increase the ranging distance by N-times without altering the external k-clock triggering mode and without sacrificing other imaging performance.

2.2 Materials and Methods

2.2.1 System design and set up

The SS-OCT system (Figure 2-1) employed in this article was equipped with a 600 kHz MEMS-tunable VSCEL-type swept source, with a central wavelength of 1310 nm and a bandwidth of 20 nm. The theoretical lateral and axial resolutions of the system were 56 μm and 37.8 μm,

respectively, in air. The k-clock signal was generated through a built-in MZI with an optical path difference of 72 mm. The currently available k-clock triggering swept sources operated at an average frequency of ~1 GHz, resulting in ~ 860 sampling points per spectrum. The interference signal was collected using a 1.8 GHz digitizer (ATS9360, AlazarTech Inc., USA).

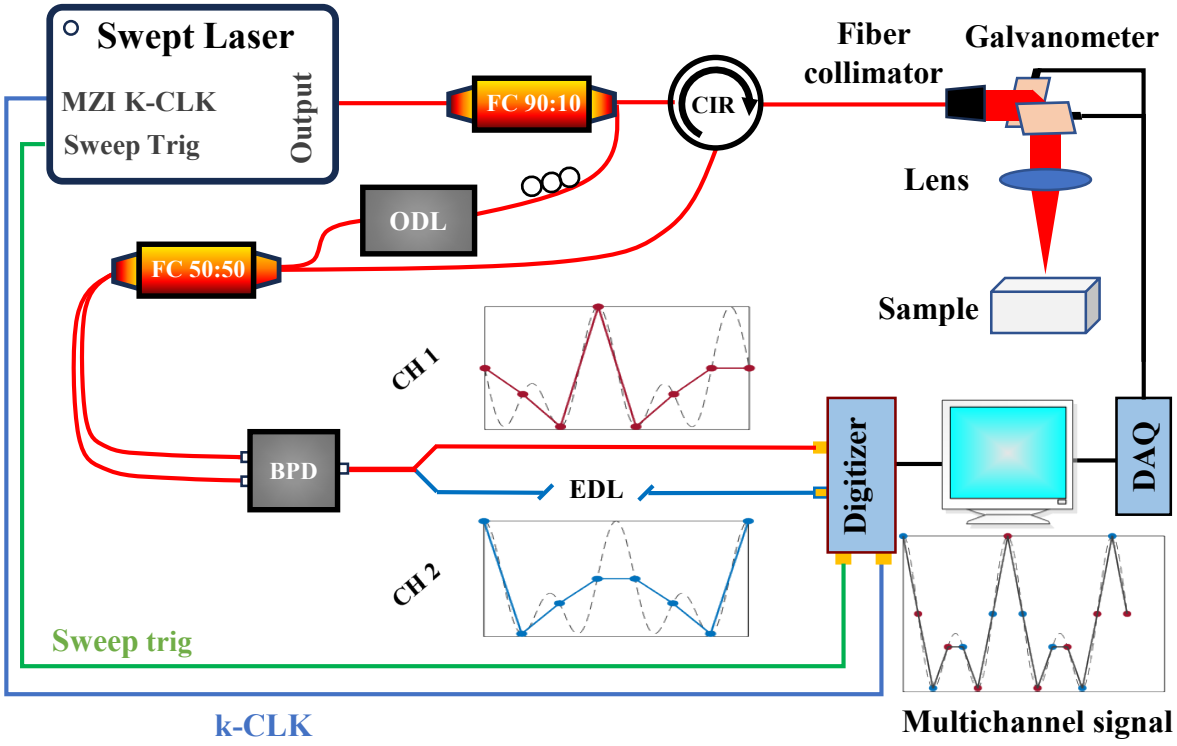

Figure 2-1 Schematic of the multichannel delayed sampling SS-OCT system setup, where two channels were realized in the demonstration. FC: fiber coupler; CIR: circulator; ODL: optical delay line; PC: polarization controller; BPD: balanced photodetector; DAQ: data acquisition. EDL: electrical delay line.

The scanning protocol was comprised of 1500 × 1500 A-lines to cover an ~42 × 42 mm² field of view, requiring 4.75 seconds to complete. In the demonstration of the proposed method, we used N=2 as an example because the digitizer only possesses 2-channel data-input ports (but it should be applicable to N channels, depending on the digitizer's channel availability). In single-channel sampling mode using the MZI to trigger the acquisition, the system's theoretical

imaging depth is limited to 18 mm. The balanced detector transforms the optical interferometric signal into electrical signals, which are then divided into two electrical paths (CH1 and CH2). These two-channel signals were then digitized using the two-channel digitizer. CH2 is delayed by a longer length of 10 cm of 50-Ω coaxial cable compared to that of CH1. This results in an approximate delay of ~0.5 ns (given a speed of 2×10^8 m/s). This delay introduces a phase difference of approximately half a sampling interval in the interference spectrum. The k-clock signal generated by the MZI was employed to concurrently trigger the acquisition of interference spectra for both channels. Subsequently, the data from the two channels were combined in k-space and resampled before being transformed into depth information through Fourier transformation.

2.2.2 Simulation of two-channel delay sampling

Multi-channel delay sampling requires precise control of the time delay for each channel within a reasonable range to ensure that the reconstructed spectrum closely matches the ground truth. Taking two channels as an example, the delay phase should be set at the middle of the wavenumber sampling interval (Δk), i.e., Δk/2. If the phase difference between the two signal paths cannot be strictly maintained at Δk/2, it may introduce artifacts in the depth profile. To clarify the relationship between phase differences and potential artifacts, we employ computer simulations to illustrate the signal recovery process, as depicted in Figure 2-2. In this simulation, we assumed the presence of two reflecting interfaces at depths of 5 mm and 28 mm (Figure 2-2A) in the sample arm, representing the low-frequency and high-frequency components of the interference signal, respectively. Figure 2-2B displays the simulated interference spectra,

with a closer view of the region inside the orange box showing the periodic coupling of two frequencies. We digitized the simulated spectra using a single channel with 1024 sampling points, resulting in the depth profile shown in Figure 2-2C. The reason for using 1024 sampling points is that it is the integer power of 2 closest to the actual number of pixels. Furthermore, to avoid confusion, nonlinear issues are not introduced in numerical simulations.

With single-channel sampling, the imaging depth is limited to 18 mm, which is insufficient for accurately identifying the reflecting interface at 28 mm. Additionally, an obvious artifact appears within this result (indicated by the blue arrow), due to under-sampling. Subsequently, we digitized the simulated spectra using two channels. Figure 2-2D to H represent the outcomes of dual-channel sampling with phase differences of 0.1Δk, 0.3Δk, 0.5Δk, 0.7Δk, and 0.9Δk, respectively. Before performing the Fourier transform, signals from two channels were directly combined without undergoing resampling. We found that dual-channel sampling extends the imaging range and allows for the identification of the reflecting interface at 28 mm. When the phase difference equals 0.5Δk (Figure 2-2F), it perfectly reproduces the true sample signal as expected. Otherwise, artifacts (indicated by the red arrows) are introduced due to non-uniform sampling, and the intensity of these artifacts increases with the increased degree of deviation relative to 0.5Δk. Figure 2-2I to L represents the results obtained after resampling the combined signals from two channels. Resampling means estimating the signal value at 0.5Δk position based on the information provided by the two channels. It can be observed that resampling helps to suppress artifacts to some extent, but the farther the deviation from the 0.5Δk position, the more difficult it is to eliminate the artifacts.

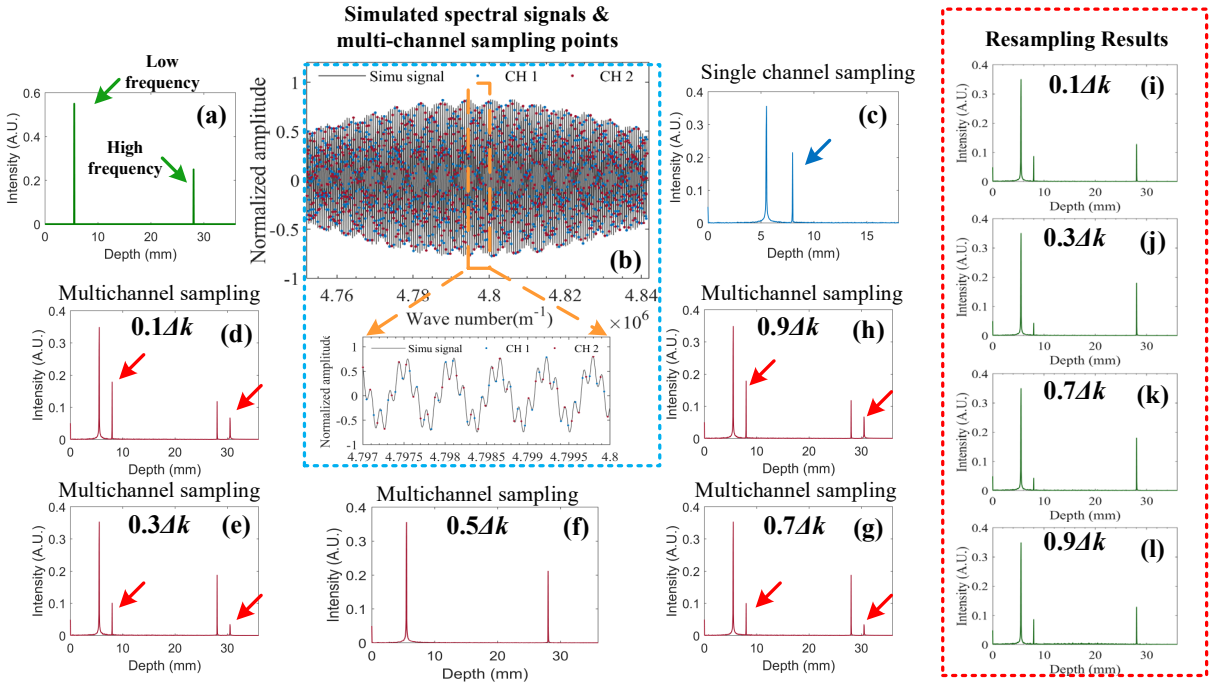

Figure 2-2. Dual-channel delay sampling signal simulation. (A) Reflecting interfaces are placed at depths of 5 mm and 28 mm, respectively. (B) Simulated corresponding interference spectra. The insert below shows an enlarged view of the region inside the orange box. (C) Result of single-channel sampling, with artifacts indicated by the blue arrows. (D)~(h)Results of dual-channel sampling with phase differences of 0.1Δk, 0.3Δk, 0.5Δk, 0.7Δk, and 0.9Δk, respectively. Red arrows point to artifacts. (I)~(L) The results after resampling.

2.2.3 Calibrate the nonlinear phase delay

The simulation above assumes that the introduced delay causes a uniform phase shift in k-space for the interference signal of Channel 2. However, it should be noted that while the k-clock signal generated by MZI interferometry exhibits linearity in k-space, its behavior in the time domain is non-linear. This non-linear relationship between k and time results in a non-uniform k-shift at each sampling point when a fixed delay is applied in the time domain. Therefore, it is imperative to estimate the k-shift (δk) in Channel 2 before resampling the combined signal.

Assuming the interference signal from a mirror is represented as:

$$I(k) = S(k)\cdot cos(2d\cdot k+\emptyset_{disp}) \quad (2\text{-}1)$$

where *S(k)* represents the optical power density of the light source, *d* is the path difference of the sample arm and reference arm, and $\emptyset_{disp}$ is the phase error induced by optical dispersion. The mirror signal of Channel 1 and delayed Channel 2 from the same location could be written as:

$$ICh1\ (k) = \mathrm{S}(k)\cdot cos(2d\cdot k+\emptyset disp) \quad (2\text{-}2)$$

$$I_{Ch2}\ (k) = S(k+\delta_k)\cdot cos(2d\cdot(k+\delta_k)+\emptyset_{disp}) \quad (2\text{-}3)$$

where, the vector δ_k represents the non-uniform k-shift at each sampling point. To estimate this non-uniform k-shift (δ_k), the phase change of the interference signals from the two channels $\Delta\theta$ can be estimated using the Hilbert transform.

$$\Delta\theta_k = ang\ (Ha\ (I_{Ch2}(k))) - ang\ (Ha\ (I_{Ch1}(k))) \quad (2\text{-}4)$$

Where $Ha\{f(t)\} = f(t) + j/\pi \cdot \int f(\tau)/(t-\tau)\, d\tau$ and *ang(·)* denotes the phase unwrapping process. Subsequently, δ_k can be calculated by taking the phase difference of the two channels:

$$\delta_k = \Delta\theta_k/2d \quad (2\text{-}5)$$

where, $\Delta\theta_k$ represents the phase difference between the two channels. Using the calculated δ_k, we can precisely determine the timing stamps of Channel 2 signals in k-space.

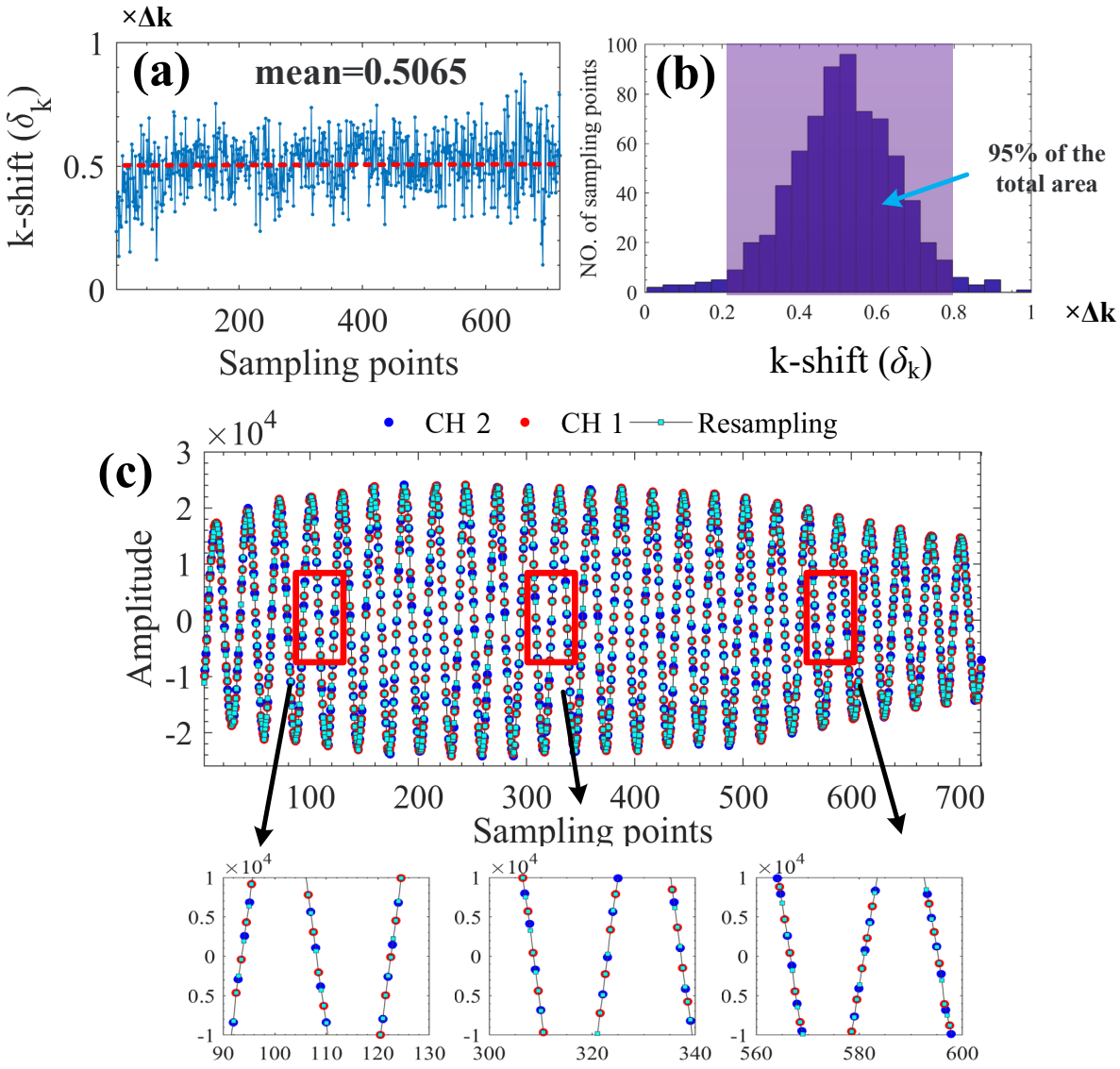

Figure 2-3. k-shift values for each sampling point of the two channels and the interpolation results. (A) δk for each sampling point, with a red dashed line indicating the mean position. (B) Distribution of δk, with the shaded area representing the interval containing 95% of the total area. (C) Interpolation results. The lower subgraphs depict magnified views of the red boxed regions.

We employed a mirror as the sample in the sample arm and collected the mirror's spectral signal using the proposed system. We adjusted the length of the electrical delay line to ensure that δk closely approximates 0.5Δk at each sampling point, as shown in Figure 2-3A. The extra-cable length was 10 cm in the electrical delay line. Figure 2-3B illustrates the distribution of δk, with a mean close to 0.5Δk. The highlighted area encompasses 95% of the total area, signifying that 95% of the sampling points fall within the interval [0.2Δk, 0.8Δk]. Most of the artifacts generated by this k-shift distribution can be eliminated through resampling. Figure 2-3C presents the combination of the digitized spectra of the two channels based on δk, along with the interpolated results using a sampling interval of 0.5Δk (cyan dots). The signal from Channel 1 (red dots) remains unchanged, while interpolation is performed using the information provided by Channel 1 and Channel 2 (blue dots). The three enlarged views show the details in interpolation at various positions. It is evident that the majority of Channel 2's sampling points are close to 0.5Δk, providing highly accurate information for interpolation at 0.5Δk, which leads to interpolation results that closely match the actual values. Results shown in Figure 2-3 indicate that the selection of a 10 cm electrical delay line was reasonable for the system in this paper. A resampling process was applied to all the acquired data from both Channels to generate a 2-fold upsampled spectrum through interpolation. Then, the regenerated spectrum underwent windowing and dispersion compensation before performing a fast Fourier transform to produce the depth OCT signals.

2.3 Results

2.3.1 System performance

To assess the system's performance, we collected reflected signals from different positions on a mirror using an optical attenuator with a 60 dB attenuation level. Figure 2-4 illustrates the point spread function (PSF) roll-off for both the single-channel system and the dual-channel delay sampling system. We observed that the imaging depth of the single-channel system is limited to 18 mm, with a PSF roll-off of -15 dB across the entire ranging distance. By implementing the dual-channel delayed sampling method, the system's ranging distance is extended to 36 mm, and the PSF roll-off at the 18 mm position is only -5 dB, where the SNR has improved because of the upsampling rate provided by dual-channel sampling, enabling the recovery of high-frequency signals at 18 mm. Table 1 summarizes a detailed performance comparison between the two systems.

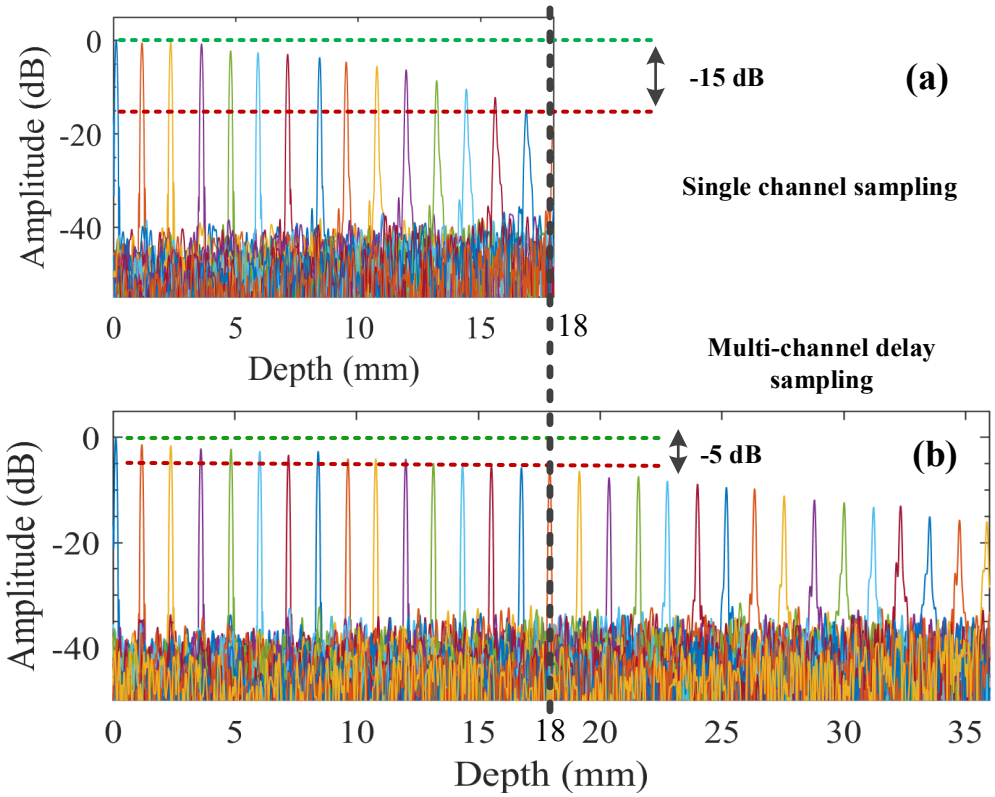

Figure 2-4. Point spread function roll-off in single-channel sampling (A) and multi-channel delayed sampling system (B).

Table 2-1 Performance comparison between single-channel sampling and dual-channel delayed sampling

Mode	Single channel	Dual channel
Roll-off at 18 mm	−15 dB	−5 dB
Roll-off at 36 mm	--	−15 dB
SNR at 18 mm	85 dB	95 dB
SNR at 36 mm	--	82 dB

2.3.2 Imaging of phantom and human teeth

To demonstrate the extended imaging capabilities of the proposed system, we conducted 3D imaging of both a relatively transparent Plexi-box (a container that was used from Thorlabs purchases) and human teeth *in vivo*. Figure 2-5A is a photograph of the Plexi-box with a height of 28 mm and with barcode labels affixed to both the upper and lower surfaces. Figure 2-5B shows the result obtained using single-channel sampling, where the artifact appears (as indicated by the blue arrow) and overlaps with the signal from the upper surface, due to the barcode situated beneath the box beyond the system's imaging depth. However, the whole box with barcode labels is successfully recovered by the dual-channel system. Figure 2-5C and D depict the results obtained using the dual-channel delayed sampling system, where the upper and lower surfaces of the box can be clearly distinguished without any ambiguity, as highlighted by the green arrows.

High-speed, long-range SS-OCT has the potential to play a significant role in clinical applications. In recent years, the utilization of OCT in the field of dentistry has been greatly expanding, offering a range of potential applications [101]. These include the observation of periodontal tissues such as gums, periodontal pockets, and alveolar bone, which information is important in assisting the health assessment such as inflammation, periodontal pocket depth, and changes in subgingival bone tissue [102]. Due to its capacity to deliver high-resolution imaging of the microstructural aspects of dental tissues, OCT also finds extensive use in the examination of various dental components such as enamel, dentin, and dentin-like structures [103]. Here, we demonstrate the potential of multi-channel delayed sampling SS-OCT systems to enable comprehensive and high-speed detection of human teeth. Healthy volunteers were

recruited to test the performance of the proposed system. The study follows the tenets of the Declaration of Helsinki and was conducted in compliance with the Health Insurance Portability and Accountability Act. Ethical approval was obtained from the Institutional Review Board of the University of Washington and written consent for imaging was obtained from each participant.

Figure 2-5E shows a photograph of teeth of imaging interest, while 5(g) and 5(i) display the 3D image results obtained using the two systems. In the case of single-channel sampling, it cannot correctly reconstruct the teeth from deeper regions due to the limited imaging range. The cross-sectional images corresponding to the blue dashed line from both systems (Figure 2-5F and E) clearly demonstrate that more teeth are accurately reconstructed with the extended imaging depth by the multi-channel sampling. This approach extends the depth of tooth imaging to cover dental arch curvatures without compromising scanning time.

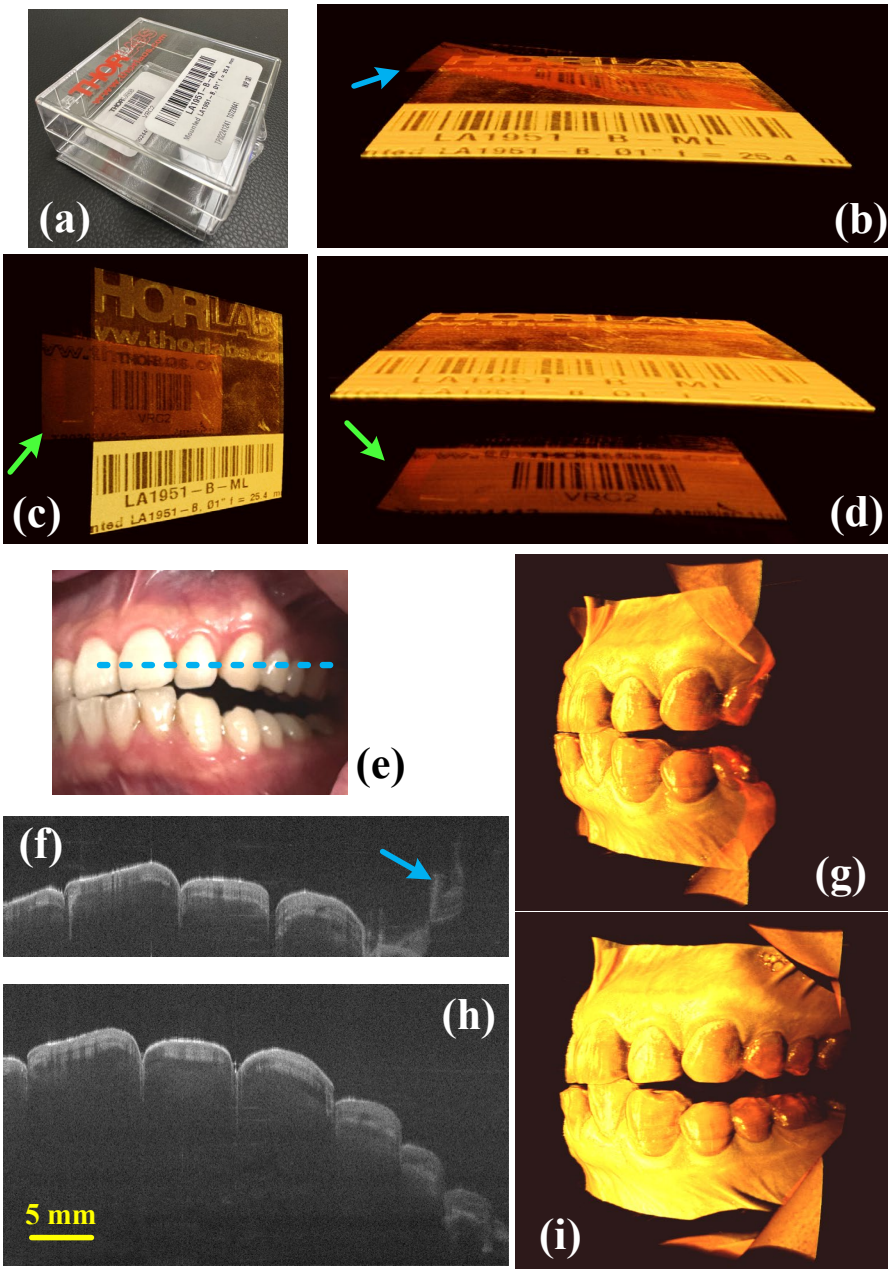

Figure 2-5. Imaging results of multi-channel delayed sampling system. (A) photograph showing the physical Plexi-box from Thorlabs purchases. (B) The result obtained using single-channel sampling (C) and (D) show the results obtained using the multi-channel delayed sampling system. The location indicated by the blue arrow is artifact, while the locations indicated by the green arrows are true sample position of interests. (E) Photograph of the teeth of imaging interest. (F) and (H) are B-scan images taken at the locations indicated by the blue dashed line in (E), obtained using a single-channel sampling system and a multi-channel sampling system,

respectively. (G) and (I) are 3D rendering of the results obtained by the two systems, respectively.

A technique that can enhance imaging depth without altering k-clock triggering or sacrificing other imaging performance holds promise for the future OCT advancement. A recent study reported a circular interferometric ranging method [104], eliminating the sparsity of scattering signals in long-range measurements. While promising, the method relies on a new ultrafast, time-stretched frequency comb laser, which unfortunately is not widely available.

In our SS-OCT system, when compared to internal clocks, k-clock trigger acquisition typically has less sampling points for a spectrum, leading to reduced ranging distance and the potential of aliasing artifacts from the deeper ranges. However, k-clock trigger acquisition eases the burden of data acquisition and storage, in addition to avoiding signal distortion. In many SS-OCT systems using this acquisition mode, the full potential of the acquisition card is not fully realized. This opens a door to multi-channel delayed sampling, given the available hardware setups in the existing system.

Multi-channel acquisition enhances the efficient use of digital acquisition card capabilities. This approach is not limited by the power of the light source since the split signals are electrical. If many channels are used, a signal amplifier at the output of the balanced detector can be used to then split the signal into several channels. There may be slight amplitude shifts due to the multi-channel signals passing through different electrical delay units, but these can be corrected through post-processing with amplitude compensation. One limitation of the paper is that, due to the constraints of the number of acquisition card channels, we have only demonstrated the results of dual-channel sampling. With an acquisition card with more than 2-channel capacity,

the imaging depth can be further extended. Of course, if affordable, multiple acquisition cards can be used in parallel to implement the proposed multi-channel time-delay sampling method. It is worth noting that while multi-channel delay sampling can extend imaging depth, the theoretical maximum imaging depth of OCT is limited by the analog bandwidth of the balanced detector. The analog bandwidth of the balanced detector used in this study was from 30 kHz to 1.6 GHz. The maximum theoretical imaging depth achievable is therefore 57.6 mm. Thus, the maximum number of channels that can be used to improve the imaging depth is 4 with the system setup described in this study.

2.4 Discussion and Conclusion

We introduce a multi-channel delayed sampling method aimed at extending the imaging depth in high-speed swept-source optical coherence tomography (SS-OCT). The technique utilizes a balanced detector to capture interference signals, which are then converted into electrical signals and split into N channels. Each channel is assigned a fixed time delay, achieved through the use of electrical cables of varying lengths. These signals are subsequently digitized by an N-channel acquisition card.

To address non-uniform phase shifts caused by these fixed time delays, a calibration procedure is applied. The signals from all channels are merged in k-space and resampled to produce a linearized spectrum, effectively increasing the sampling rate by a factor of N. This extension in sampling rate allows for an increase in the ranging distance by N times, without requiring modifications to k-clock triggering or other imaging parameters.

In addition to extending the imaging depth, this method also enhances the signal-to-noise ratio (SNR) and sensitivity within the original depth range, significantly improving the overall performance of SS-OCT systems. The multi-channel delayed sampling approach is validated and shown to effectively extend the imaging depth without compromising imaging speed. It holds potential for expanding the application of high-speed SS-OCT, particularly in the realm of biomedical research.

3 HIGH-SPEED, LONG-RANGE AND WIDE-FIELD OCT FOR *IN VIVO* 3D IMAGING OF ORAL CAVITY ACHIEVED BY 600 KHZ SWEPT SOURCE LASER

3.1 Background and Motivation

Since its inception, optical coherence tomography (OCT) has undergone remarkable progress, evolving from time-domain to spectral-domain configurations and, more recently, embracing the sophisticated swept-source OCT (SS-OCT) [105–108]. These continuous technological innovations have firmly established OCT as an indispensable tool in various biomedical imaging applications, spanning clinical fields such as ophthalmology [9,10,109,110], dentistry [11,103,111,112], dermatology [18,113–116], endoscopy[115,117–121], neuroscience[116,122–124], and more.

Recently, OCT has garnered significant attention for its application in imaging the oral cavity [103], owing to its capability of providing 3D microstructural and microcirculation information that can aid clinical assessments in dentistry. Notably, its non-radiative nature positions it as a safe imaging modality for oral cavity examinations in pregnant women and children [125]. Moreover, OCT has demonstrated efficacy in detecting tooth demineralization and cavities by observing changes in backscattered signals from enamel and dentin [126]. Even in the early stages of enamel demineralization, OCT excels in identifying the locations of white spot lesions [127,128]. Additionally, OCT can be employed for diagnosing tooth fractures, manifesting as clear bright lines in OCT images [126]. Enamel thickness, a reflection of tooth

wear, can be quantified using OCT, offering a valuable tool for assessing enamel loss. Beyond hard tissues, OCT has shown applicability in examining soft tissues, addressing conditions such as gum diseases [129], oral mucosal lesions [130], and oral tumors [131].

Despite these successes, existing OCT systems in dentistry face challenges, primarily stemming from slow imaging speed and a limited imaging field of view (FoV). Additionally, the uneven topology of the oral cavity demands OCT to have a relatively long-ranging distance (>20mm). Currently, most existing OCT systems designed for dental applications have an A-scan rate typically ranging from 20 kHz to 200 kHz and a ranging distance of <12mm, providing a FoV generally smaller than 10×10 mm^2 that covers only one to two teeth [11,132,133]. These limitations hinder the efficiency of data acquisition, impacting the workflow in imaging practice, especially in situations where a rapid overall visualization and examination of a patient's oral cavity is required. An ideal OCT system for dentistry should possess enhanced imaging capabilities, overcoming the current challenges. Therefore, the development of dental OCT should prioritize: 1) improved imaging speed, crucial for real-time clinical applications and patient comfort; 2) expanded field of view to capture comprehensive images of the entire oral cavity in a single scan, facilitating more efficient and thorough examinations; and 3) increased ranging distance to cope with uneven surface topology in the oral cavity. Previous studies have attempted to achieve a large FoV by montaging multiple scans [11]. Although this approach mitigates the oral curvature, it would prolong the time required to complete an imaging session, significantly affecting patient compliance for imaging.

With the current rapid development of swept laser sources, it is theoretically straightforward to meet the requirements for an OCT system to achieve oral cavity imaging with a wide FoV

and long-ranging distance. For example, a 1310nm vertical-cavity surface-emitting laser (VCSEL) has been reported to achieve a cubic meter volume imaging for OCT applications but realized with the assistance of a high-speed oscilloscope with a 16 GHz analog bandwidth that sampled the data at 50 GS/s and underwent post-data processing [87]. While exciting, achieving fast scanning speed, long imaging range, and a wide FoV simultaneously in practice pose a significant challenge for current OCT hardware, particularly when considering electrical signal collection and handling. This is simply because the signals with high-frequency and high-bandwidth must be dealt with, including both the OCT interference signals of interest and the k-clock signal used to trigger data acquisition. As a note, the bandwidth mentioned here refers to the frequency range of the generated interference signal. To avoid confusion, we refer to the wavelength range of the light emitted by the laser source as spectral bandwidth, whereas the frequencies range of the interference signal as frequency bandwidth.

The signal handling unit, including photodetectors, transmission cables and acquisition cards, typically assumes a linear frequency response within a designated frequency bandwidth. If the signal frequency is close to or beyond the limit of this bandwidth, a non-linear phase response would occur, introducing a time delay. The situation worsens for OCT signals because the spectral broadband swept source generates an interference signal with a frequency bandwidth that is consequently converted into a broadband electrical signal, imposing different time delays for different wavelengths. This process is akin to the optical dispersion phenomenon observed in OCT imaging. Here, we refer to this electrical time delay as electrical dispersion when a high-frequency OCT signal with broad frequency bandwidth travels through the system

hardware before being sampled by the data acquisition card. This electrical dispersion would inevitably affect the imaging performance of the OCT system.

Frequently when designing an OCT imaging system for most applications, for example retinal imaging, the frequency bandwidth of the hardware may be adequate to cope with the OCT interference signals due to the requirement of relatively short ranging distance where a ranging distance of 6 mm may be sufficient[6,30]. To digitally sample this OCT signal, an efficient way is to sample it in a linearized k-space through a k-clock triggering acquisition, facilitated by an auxiliary Mach-Zender interferometer (MZI). This is because compared to the internal clock acquisition [22,94], this method eliminates the need for resampling interference spectrum signals of interest, reducing the burden on the acquisition card and simplifying post-data processing [96]. In this case, to properly generate the k-clock signal to trigger the sampling, the frequency of the MZI signal is required to be at least twice that of the OCT signal of interest (per Nyquist theorem), determined by the optical delay set at the MZI, resulting in an expanded frequency bandwidth of the k-clock signal that likely goes beyond the designated frequency bandwidth for the hardware, leading to a noticeable phase shift for each sampling point (zero crossing point) due to the non-linear phase responses. Consequently, the k-clock triggered acquisition would inevitably deteriorate the system imaging performance, e.g., broadening the system point-spread function, especially in the regions with long-ranging distances. As a result, minimizing the influence of non-linear frequency phase response is crucial for developing high-speed, long-range, and wide FoV OCT imaging systems.

In this paper, we propose a high-speed and long-range solution applied to oral cavity examinations under the constraints of the existing data acquisition unit. This system operates at

a scan speed of 600 kHz, providing a wide imaging field of 42×42 mm² and a ranging distance of 36 mm, effectively matching the physiological curvature of the oral cavity. To address the issue of k-clock non-linear phase errors, we propose a global k-clock calibration method to compensate for the electrical dispersion, verified by the analyses of system sensitivity roll-off curve and point spread function before and after compensation. Furthermore, this paper analyzes and compensates for spatial discrepancies resulting from long-range and wide-field imaging. In addition, when a detailed examination of a specific area of interest is desired, the system is designed with a function to achieve high-precision imaging by switching scanning protocols and objective lenses. This system bridges the gap between ultra-high-speed (multi-MHz) and conventional 100 kHz level SS-OCT systems and meets various requirements for oral cavity examinations, expanding OCT applications for oral health inspection and making it a powerful tool for comprehensive oral cavity examinations in dentistry.

3.2 Materials and Methods

3.2.1 System setup and scanning protocol

Figure 3-1shows a schematic diagram summarizing a representative SS-OCT system that was constructed, featuring high-speed, long-distance ranging, and wide FoV capabilities. The system incorporated a cutting-edge 600 kHz MEMS VCSELs swept laser source, centered at 1310 nm with 20 nm bandwidth. This configuration provided a theoretical axial resolution of approximately 41.5 μm in air (equivalent to ~29.6 μm in tissue, assuming a refractive index of 1.4). Notably, the laser featured a built-in sweep trigger and linear k-clock, serving as the initiation signal for an external clock to synchronize the interference fringes and subsequent

data acquisition. The laser output was directed through a 90/10 fiber coupler, splitting 90% power to the sample arm, and allocating 10% to the reference arm. In the sample arm, the laser was coupled to a fiber collimator, generating a collimated beam with a diameter of approximately 2.8 mm. This collimated beam was then guided to the sample using a pair of synchronized galvo scanners (6210H, Cambridge Tech Inc. USA) triggered by the sweeping mechanism. The delivery of light to the sample was facilitated by an f-theta lens with a 100 mm focus length, achieving a lateral resolution of ~60 μm.

In the reference arm, an optical delay line was employed to align the optical path difference between the sample arm and reference arm. The backscattered light from the sample arm via a fiber circular (CIR-1310-50-APC, Thorlabs Inc., USA), and the matched reference light were coupled to a 50/50 fiber, subsequently directed to a balanced photodetector. To optimize the time delay between the trigger and k-clock and reduce the phase jitter arising from swept-to-swept variations [134], a function generator was employed to introduce a controlled delay to the swept trigger signal. The interference signal was sampled by a 1.8 GHz digitizer with a designed frequency bandwidth from DC to 0.8 GHz (ATS9360, AlazarTech Inc., USA). We carefully considered the electrical cable layout in the system design and construction, which makes the signal frequency bandwidth of the entire system dominated by the digitizer employed, meaning the system frequency bandwidth was also from DC to 0.8 GHz.

The designed ranging distance of the OCT system was 18mm in the air, given the MZI with a 72 mm optical path difference (OPD) and the digitizer operating at single edge sampling mode. With this ranging distance, the laser operating at 600 kHz and 20nm spectral bandwidth would generate a highest frequency OCT interference signal at maximum ranging distance that

estimates to have an averaged frequency of ~0.5 GHz and a frequency bandwidth of ~0.4 GHz. While such a signal would experience electrical dispersion when it travels from the detector to the digitizer, the effect would be negligible because the signal frequency bandwidth of interest is well within the capacity of system frequency bandwidth of 0.8 GHz. This is likely the reason why prior SS-OCT system developments reported in the literature did not notice this electrical dispersion issue. However, it may not be true when handling the MZI interference signals to generate k-clock signals for triggering the data acquisition, which will be discussed in detail in next Section. In order to increase the ranging distance with the k-clock signal generated by the MZI with a fixed OPD of 72 mm, the digitizer was operated with a dual edge sampling (DES) mode in this study. This DES sampling leads to an actual imaging range of 36 mm from the originally designed 18 mm.

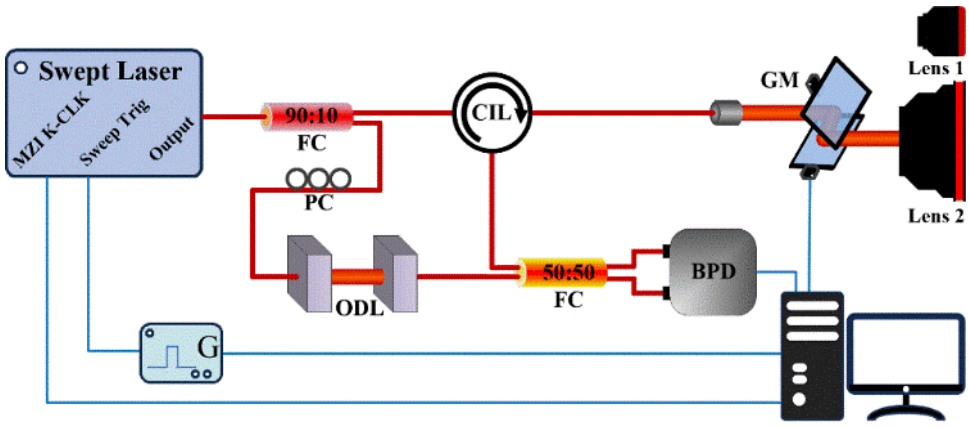

Figure 3-1. Representative schematic of the proposed 600 kHz swept source optical coherence tomography system. FC: fiber coupler; CIR: circulator; ODL: optical delay line; PC: polarization controller; BPD: balanced photodetector; G: function generator; GM: galvanometer.

For *in vivo* demonstration of the system performance to image oral cavity, healthy volunteers were recruited. The study adheres to the principle of the Declaration of Helsinki and complies with the Health Insurance Portability and Accountability Act. Ethical approval was granted

from the Institutional Review Board of the University of Washington and written consent for imaging was obtained from each participant. During the imaging session, the participants were instructed to rest their head on a chin rest for stability. To facilitate wide-field imaging, a mouth opener was employed to maximally expose the oral cavity to the OCT scans. The scanning protocol consisted of 1500 × 1500 (OCT imaging mode) and 1500 × 1500 × 4 A-lines (OCT angiography (OCTA) mode), covering a ~42 × 42 mm2 FoV. One single 3D scan took a duration of ~5 sec and ~19 sec to complete for OCT and OCTA mode, respectively.

While the wide-field imaging mode is advantageous for swift and comprehensive oral cavity examinations, the proposed system offers an additional flexibility for localized fine scanning when detailed observation of suspicious localized lesions is required. For this purpose, the system was designed to have an optional high-resolution scan mode. In this mode, we utilized a telecentric lens with a focal length of 36 mm, providing a lateral resolution of ~22 μm. To stabilize subjects during imaging, a bite bar was utilized. The scanning protocol consisted of 1000 × 1000 (OCT imaging mode) and 1000 × 1000 × 4 A-lines (OCTA mode), covering a ~7 × 7 mm2 FoV. One single 3D scan took a duration of ~2.2 sec and ~8.7 sec to complete for OCT and OCTA mode, respectively.

An eigen-decomposition optical microangiography (OMAG) algorithm was applied to extract blood flow signals from four repeated B-scan images [47]. The resulting blood flow signals at different depths were color-coded with the depth information from tissue surface and projected onto a two-dimensional plane, generating en-face OCTA images for visualization.

3.2.2 System k-clock calibration and practical considerations

While the analysis in this section is equally applicable to the OCT interference signals of interest, we will focus on the discussion of k-clock signal generation and the effect of its non-linear phase response on imaging performances. In conventional SS-OCT systems, a k-clock trigger signal is commonly employed to clock the acquisition of the interference signal in order to mitigate the mechanical sweep-to-sweep variations inherent in VCSEL's operation [87,96]. The k-clock trigger signal is typically generated by an auxiliary MZI with a predetermined OPD, tailored to the specific requirements of the system design. Subsequently, a zero-crossing detector is employed to convert the MZI interference signal into the k-clock signal, aligning its frequency with that of the MZI signal. The mathematical representation of the MZI signal, characterized by an OPD of ΔZ_{MZI}, is:

$$I_{MZI}(k) = S(k)cos\ (\Delta Z_{MZI} \cdot k) \tag{3-1}$$

where $S(k)$ represents the laser source power spectrum, and k indicates the wavenumber. Consequently, the generated k-clock frequency (f_{clk}) can be expressed as:

$$f_{clk} = \frac{\Delta Z_{MZI} \cdot \delta_k}{2\pi} \tag{3-2}$$

where δ_k denotes the sweep rate of wavenumber during the laser source operation. Assuming an ideal linear wavenumber change in the time domain, δ_k is given by:

$$\delta_k = \frac{\Delta k \cdot f_{sweep}}{D} = \frac{2\pi\Delta\lambda}{{\lambda_c}^2} \cdot \frac{f_{sweep}}{D} \tag{3-3}$$

where Δk is the variation in k within a sweep, fsweep is the sweep rate of the laser source, D is the sweep duty cycle (typically ranging from 0.3 to 0.7), $\Delta\lambda$ is the optical wavelength bandwidth, and λ_c is the central wavelength. Thus, considering a linear sweep of wavenumber, the expression for an averaged f_{clk} becomes:

$$f_{clk} = \frac{\Delta Z_{MZI} \cdot \Delta\lambda \cdot f_{sweep}}{{\lambda_c}^2 \cdot D} \tag{3-4}$$

where the generated k-clock trigger would be a signal with its frequency proportional to MZI OPD (ΔZMZI), spectral bandwidth (Δλ), and laser sweep rate (f_{sweep}).

In practical applications, achieving a perfectly linear sweep of wavenumber in the time domain poses challenges due to the mechanical tuning of the mirror in the MEMS VCSEL laser source. The inherent nonlinear wavenumber sweep over time is unavoidable [135]. Assuming a deviation range of Bk (i.e., the frequency bandwidth of δ_k), the frequency of the k-clock signal would also vary within a specific range according to equation 3-2, referred to as the k-clock frequency bandwidth, which is scaled with the MZI OPD that determines the OCT ranging distance.

For example, for the system described in this paper, if an OPD is set to 36 mm, each interference spectrum can theoretically generate a k-clock trigger signal with an average frequency of ~0.5 GHz, under a linear wavenumber sweep rate with a setting of $\Delta\lambda$ = 20 nm, λ_c = 1310 nm, f_{sweep} = 600 kHz and D = 0.5. However, the wavenumber changes nonlinearly in time domain will give rise to an estimated k-clock frequency bandwidth of ~0.4 GHz. Transmitting a k-clock signal through the electronic devices essential in the system introduces

frequency dependent phase instability due to the nonlinear phase response of electronic devices, including the transmitting electrical cables. Essentially, the higher the k-clock frequency bandwidth produced by each MZI interference spectrum, the greater the phase error would be. It is important to note that this phase instability may not be noticeable when the ranging distance is relatively short, as in the conventional system setup where the ranging distance is typically less than 12 mm simply because they are within the capability of the system frequency bandwidth.

In our system design tailored for dental imaging applications involving uneven surfaces, maximizing the measurement range necessitates generating as many k-clock trigger signals as possible for each MZI interference spectrum. Consequently, the optical path difference in the MZI was set to 72 mm in our design, theoretically generating 920 trigger signals per interference spectrum (actually available 850). At this limit, each interference spectrum can theoretically generate an average frequency of ~1 GHz k-clock trigger signals, with a frequency variation range from 0.5 to 1.3 GHz (beyond the system bandwidth of DC to 0.8GHz). Under this circumstance the electrical dispersion would occur, leading to a non-linear phase error in the acquired interference signals, which would degrade OCT imaging performance.

To visually demonstrate the impact of k-clock phase errors on the system, reflection signals were collected at various depths using a mirror as the sample, with the implementation of a 52 dB attenuator to mitigate strong reflections. In Figure 3-2A, the measured point spread function (PSF) roll-off curve across the 36 mm ranging distance, employing the MZI-generated k-clock for triggering and DES sampling, is depicted, where an average SNR is approximately 97.7 dB. The PSF exhibits a relatively symmetrical profile with a narrow peak within a ranging distance

of less than 10 mm, attributed to negligible phase errors from electrical dispersion for low-frequency interference signals. However, with the increase of the ranging distance, the PSF tends to broaden asymmetrically, accompanied by an elevation of side lobes on the left. This phenomenon primarily arises from the same phase drift but results in a larger phase difference in the high-frequency signal region. The axial resolution, assessed by the full width at half maximum (FWHM) of the PSF marked by black dots, experiences a gradual decline within the initial 16 mm of the ranging distance, followed by a rapid deterioration beyond this point. This decline significantly impacts the performance of the OCT system, particularly in capturing images beyond 16 mm, leading to diminished image quality as the ranging distance increases. In essence, the nonlinear phase effect in the generated k-clock signal begins to affect the acquired OCT signal around a ranging distance of approximately 16 mm (with an average frequency of ~0.4 GHz). Interestingly, this value coincides with half of the frequency bandwidth of the system, which warrants further investigation.

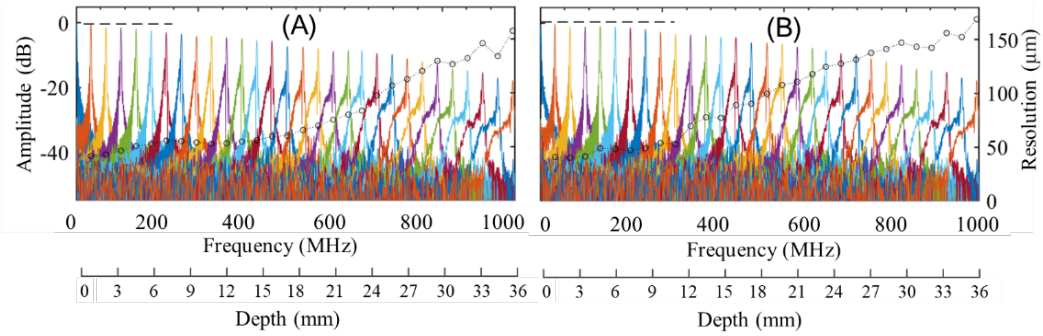

Figure 3-2. The system sensitivity roll-off and axial resolution measurements of the 600 kHz SSOCT system: (A) without optical dispersion compensation and (B) with optical dispersion compensation. Shown are the point spread functions (PSFs) measured at each ranging distance that are plotted with different colors, and the dash lines with circle markers show the corresponding axial resolution measured by the FWHM of the PSFs using gaussian fitting.

While the OCT interference signal is sampled in a linear k-space, there may still be residue of optical dispersion effect in the acquired interferogram. For this reason, numerical optical dispersion compensation methods are often effective to further minimize this effect on the PSF performance [136]. After employing the numerical optical dispersion compensation, the PSF performance (Figure 3-2B) is improved, but only within a narrow imaging range of less than 11 mm. The system sensitivity -3 dB roll-off is improved from 7 mm to 11 mm. The SNR has increased from 97.7 dB to 98.1 dB. However, it does not yield a global improvement in the PSF performance, particularly at deeper-ranging distances, where the effect of electrical dispersion in the generated k-clock signal gradually becomes non-negligible in the sampled interference signal of interest.

To rectify the nonlinear phase shift in the k-clock signal and improve the PSF performance throughout the entire ranging distance, we introduced a polynomial equation to model and compensate for the nonlinear phase error. Considering an OCT signal from mirror in air at depth z as I(k)= S(k)cos(φz), the phase evolution of the interference signal can be expressed as

$$\varphi_z = 2z(k - k_0) + 2z\Delta_{k-k_0} + \sum_{u=2}^{v} a_u \, (k - k_0)^u \qquad (5)$$

here z represents the depth, k is the wavenumber, k0 denotes the central wavenumber, Δk-k0 signifies the nonlinear k shift at the wavenumber of (k- k0), au represents the optical dispersion coefficients, and v is the highest dispersion order. The first term of the equation accounts for a linear k-clock induced phase component, and the second term represents a nonlinear k shift induced component, both of which are depth related. The last term accounts

for phase distortion from system's optical dispersion, which is approximately depth independent.

To accurately model the nonlinear k shift, the optical dispersion-induced phase error is computed by the difference of the phase evolution from a mirror at two adjacent positions:

$$\varphi_{z_1} - \varphi_{z_2} = 2\Delta z_{1,2}(k - k_0) + 2\Delta z_{1,2}\Delta_{k-k_0} \quad (6)$$

where $\Delta z_{1,2} = z_1 - z_2$. To determine the k shift, a polynomial equation was employed to approximate the change in k with $\Delta_{k-k_0} = \sum_{\mathrm{p}=0}^{m} C_p\,(k - k_0)^p$, where Cp represents p-order coefficients, and m is the highest order. To optimize across the entire ranging distance from multiple measurements, the minimum phase residual:

$$Loss = \sum_{\mathrm{q}=2}^{n} \frac{1}{\Delta z_{\mathrm{q}-1,\mathrm{q}}} \cdot \left| \varphi_{z_{\mathrm{q}-1}} - \varphi_{z_{\mathrm{q}}} - 2\Delta z_{\mathrm{q}-1,\mathrm{q}} \cdot \left[(k - k_0) + \sum_{\mathrm{p}=0}^{6} C_p\,(k - k_0)^p \right] \right| \quad (7)$$

is utilized as the merit function to find a globally optimized nonlinear k shift vector, Δk- k0. In this study, a six-order polynomial curve was employed to fit the electronic phase frequency response from three measurements. The impact of the nonlinear k shift was subsequently eliminated by resampling the interference signal with the subtracted nonlinear shift from the raw k vector.

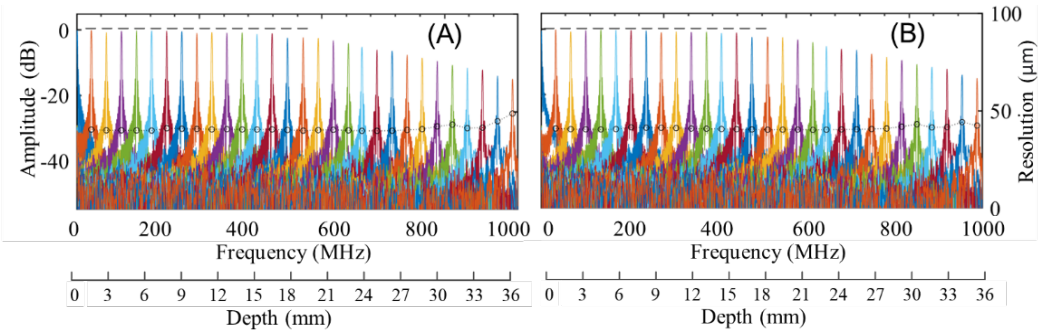

Figure 3-3. The system sensitivity roll-off and axial resolution measurements of the 600 kHz SSOCT system with k-clock calibration: (A) without optical dispersion compensation and (B) with optical dispersion compensation. The system point spread functions (PSFs) measured at each optical delay are plotted with different color, and the dash lines with circle markers show the corresponding axial resolution measured by the FWHM of the PSFs using gaussian fitting.

Upon applying the k-clock calibration method as described above, a notable enhancement in the PSF performance was achieved, as depicted in Figure 3-3A. The measured FWHM of the PSF exhibits a consistently flat profile across the entire ranging distance, resulting in a mean resolution of 42.3 μm (close to theoretical value of 41.5 μm). The average SNR increased from 97.7 dB to 101 dB. In contrast to the PSF roll-off without calibration (Figure 3-2A), the -3 dB roll-off distance is expanded from 7 mm to 18 mm, while the total sensitivity remains consistently above 104.9 dB throughout the -3 dB roll-off distance post-compensation. These improvements in PSF performance and sensitivity demonstrate the effectiveness of the k-clock compensation in enhancing the imaging capabilities of OCT system. When combined with optical dispersion compensation, the PSFs roll-off closely resembles its profile prior to dispersion compensation, with a very slight axial resolution improvements in longer ranging distances (Figure 3-3B). The improvement in SNR is also no longer significant. This observation further attests to the fact that the phase error originating from k-clock nonlinearity,

attributed to electrical frequency responses, is effectively addressed by the proposed compensation process.

3.2.3 Field of view calibration and lateral resolution assessment

Wide-field imaging inevitably introduces image distortion. This distortion may stem from non-uniformities in lenses including optical aberration or other optical elements in the system, leading to varying degrees of distortion across the imaging FoV during scanning. Additionally, differences in the focusing performance of the beam at the edges of the lens compared to the central portion can cause a distortion in the resulting images, especially in the periphery. To accurately estimate the FoV and calibrate this image distortion, we employed a target with a grid pattern of circular dots as the calibration reference. This target featured black dots with a radius of 50 μm, spaced 2 mm apart on a white background. Precise alignment with the OCT system was achieved using a translational stage and a kinematic mount, ensuring the target's center was perpendicular to the output probing beam. The total size of the target was ~50 × 50 mm^2. A 3D scan consisting of 1500 × 1500 A-lines was performed using the designed system described in the last Section to generate an *enface* image of the target using maximum intensity projection along the depth direction (Figure 3-4A). The estimated FoV was approximately 42 × 42 mm^2. The dot-grid pattern locations (red dots in Figure 3-4A) were detected, and a distortion vector map was calculated by comparing them to the prior-known pattern.

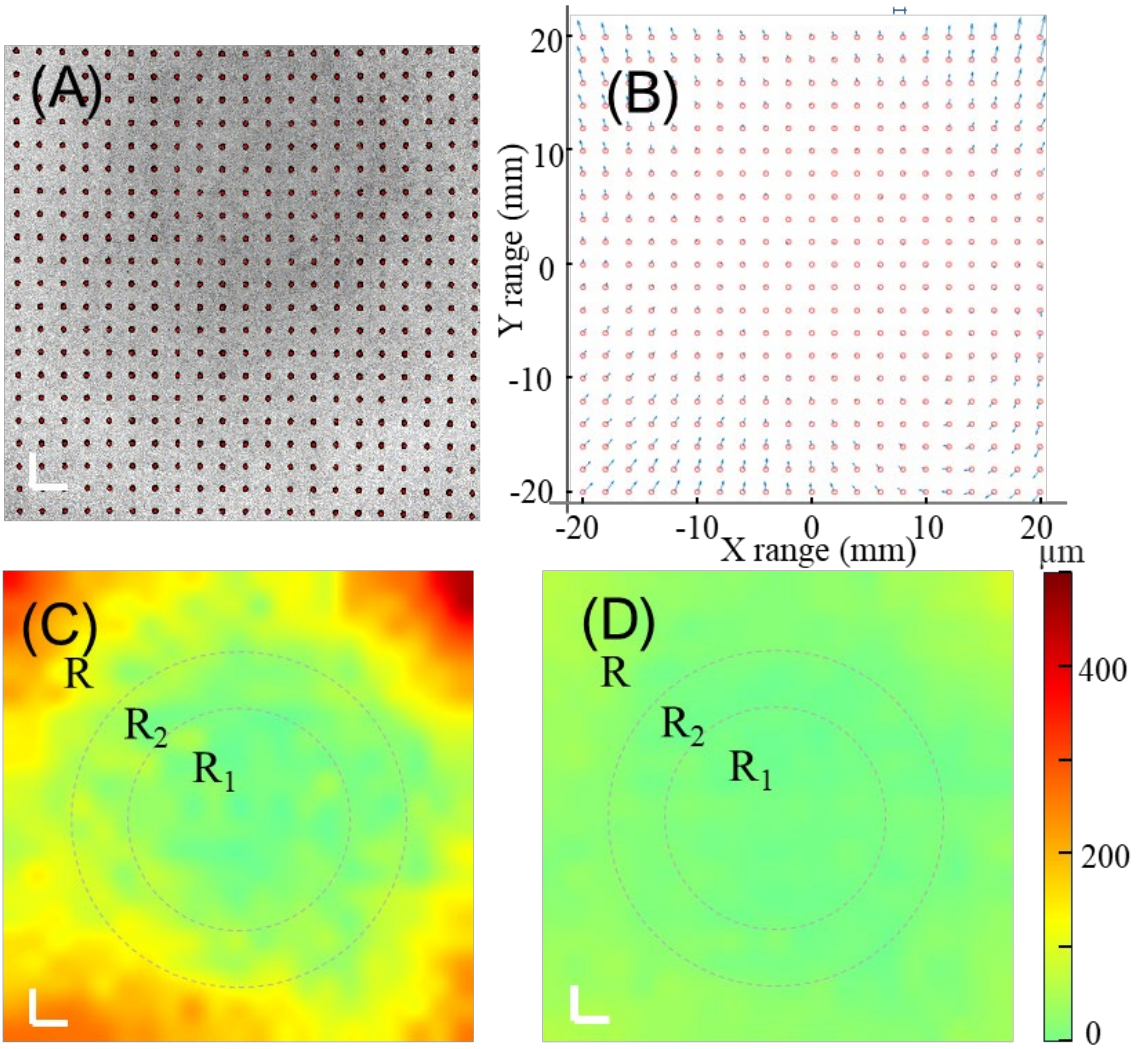

Figure 3-4. Calibration of field of view distortion. (A) *En-face* projection image generated from a circle-grid target with a field of view (FoV) of 42 × 42 mm^2. Red dots indicate the detected locations of the circle-grid pattern. (B) Distortion vector map calculated from (A). (C) Absolute distortion map generated from (B), where R1 and R2 represent the circle regions with diameters of 20 mm and 30 mm, respectively, and R represents the entire FoV. (D) The absolute distortion map after correction. The scale bars for all images are 3 mm, unless otherwise indicated.

To better visualize the FoV distortion, we calculated an absolute FoV distortion map based on the distortion vector map (Figure 3-4C). R1 and R2 represent the circle regions with diameters of 20 mm and 30 mm, respectively, and R represents the entire FoV. The peripheral regions exhibited larger distortion, attributed to the relatively significant optical aberration of

the f-theta lens at large angles. Most of the FoV regions displayed a distortion less than 200 μm, with an average distortion of 104.9 μm across the entire FoV. To correct this distortion, a post-resampling of the enface image was therefore performed using a compensation distortion map derived from even interpolation of the distortion vector map, resulting in Figure 3-4D where most of the distortions are seen to be corrected. Table 3-1 summarizes the statistics of FoV distortion in different regions of interest before and after correction. The FoV distortion correction would help provide a more accurate and reliable imaging in wide-field imaging mode.

Table 3-1. The Statistics of FoV distortion in different regions of interest before and after distortion correction

Regional distortion	**Before correction**		**After correction**	
/μm	Mean	Max	Mean	Max
R_1	28.6	99.8	18.8	37.6
R_2	46.7	159.7	21.2	44.7
R	104.9	506.3	33.5	117.8

The practical lateral resolution of the proposed wide field OCT system was evaluated using a knife-edge technique. The blade was fixed with its edge-oriented perpendicular to the OCT beam. Two imaging modes, namely wide-field imaging and high-resolution imaging were employed to capture images of the blade. Figure 3-5C A and B illustrate the maximum intensity projection images of the blade generated by both imaging modes, respectively. The zoomed-in images on the right side of Figure 3-5C A and B provide a closer view of the image region marked by the blue box. The hollow circles in Figure 3-5C C and D indicate the signal intensity at the cyan line positions corresponding to Figure 3-5C A and B. The estimated focal spot size was approximately 56.7 μm. The red curves represent the intensity fitting curves obtained through a point spread function analysis. The derivatives of these curves are depicted by the

yellow dashed lines in Figure 3-5C and D. The lateral resolution of the system was then determined by measuring the FWHM of the derivatives. Multiple measurements yielded a spot size of 60.4 ± 5.2 μm in wide-field imaging mode and 22.3 ± 1.6 μm in local imaging mode. Table 3-2 provides a summary of the system parameters under both the imaging modes.

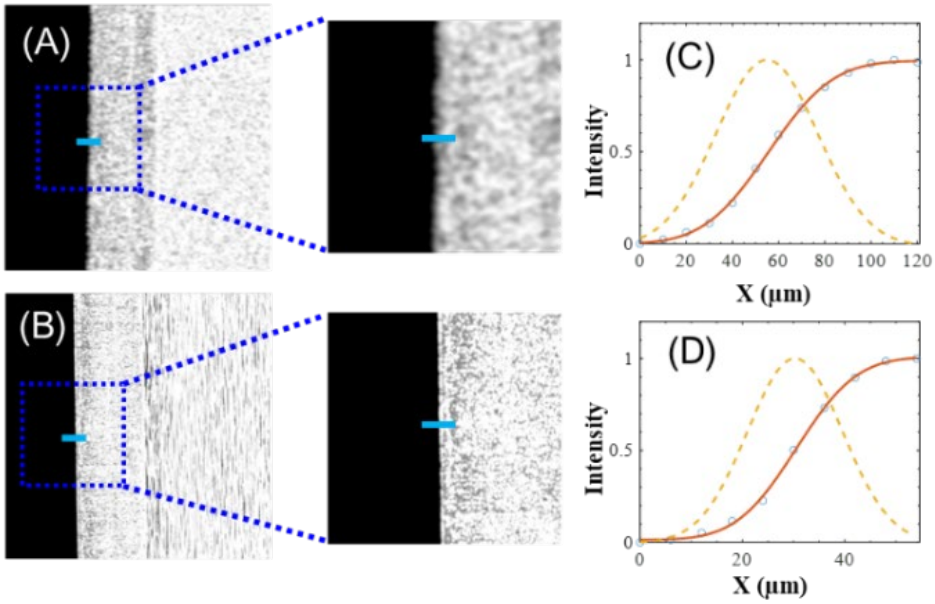

Figure 3-5 Assessment of the lateral resolution of the proposed high-speed, long range and widefield OCT using knife-edge. A. Maximum intensity projection *en-face* image in wide-field imaging mode with scale bars denoting 1mm. B. Maximum intensity projection *en-face* image in local imaging mode. The zoomed-in images on the right side of A and B are magnified images of the blue box positions. C and D show the intensity fitting curves and corresponding derivative curves of the blue solid line positions in A and B, respectively.

Table 3-2. System parameters in two imaging modes

Imaging Mode	**Spot size** (μm)	**FoV** (mm^2)	**DOF** (μm)	**Scanning protocol**	**Acquisition time** (s)	**Axial resolution** (μm)	**SNR** (dB)	**-3dB Roll off distance** (mm)
Wide-field	60.4 ± 5.2	42×42	~5000	1500× 1500×4	19.0 s	37.8	101	18.0
High-resolution	22.3 ± 1.6	7×7	~800	1000× 1000×4	8.7 s	37.8	101	18.0

3.3 Results

3.3.1 *In vivo* OCT imaging of oral cavity

In vivo imaging of the human oral cavity was conducted using the proposed OCT system. Figure 3-6A showcases a 3D volume rendering of the anterior oral cavity using the developed prototype in the wide field imaging mode, offering an expansive FoV of approximately 42 × 42 mm^2. This image provides detailed morphological information of the anterior oral cavity, encompassing fourteen teeth, labial frenum, and gingiva with one single scan. Generally, OCT proves effective in distinguishing enamel caries by detecting the enhanced backscattering signal resulting from microporous structures formed by localized tooth demineralization. With light penetration within the enamel region, the depth-resolved information unveils a distinct map of enamel health. While it requires clinical expertise to confirm, the cross-sectional view of the enamel corresponding to the red arrow region of Figure 3-6 highlights a suspicious enamel carious lesion, exhibiting increased backscattering in Figure 3-6B and C (red arrows).

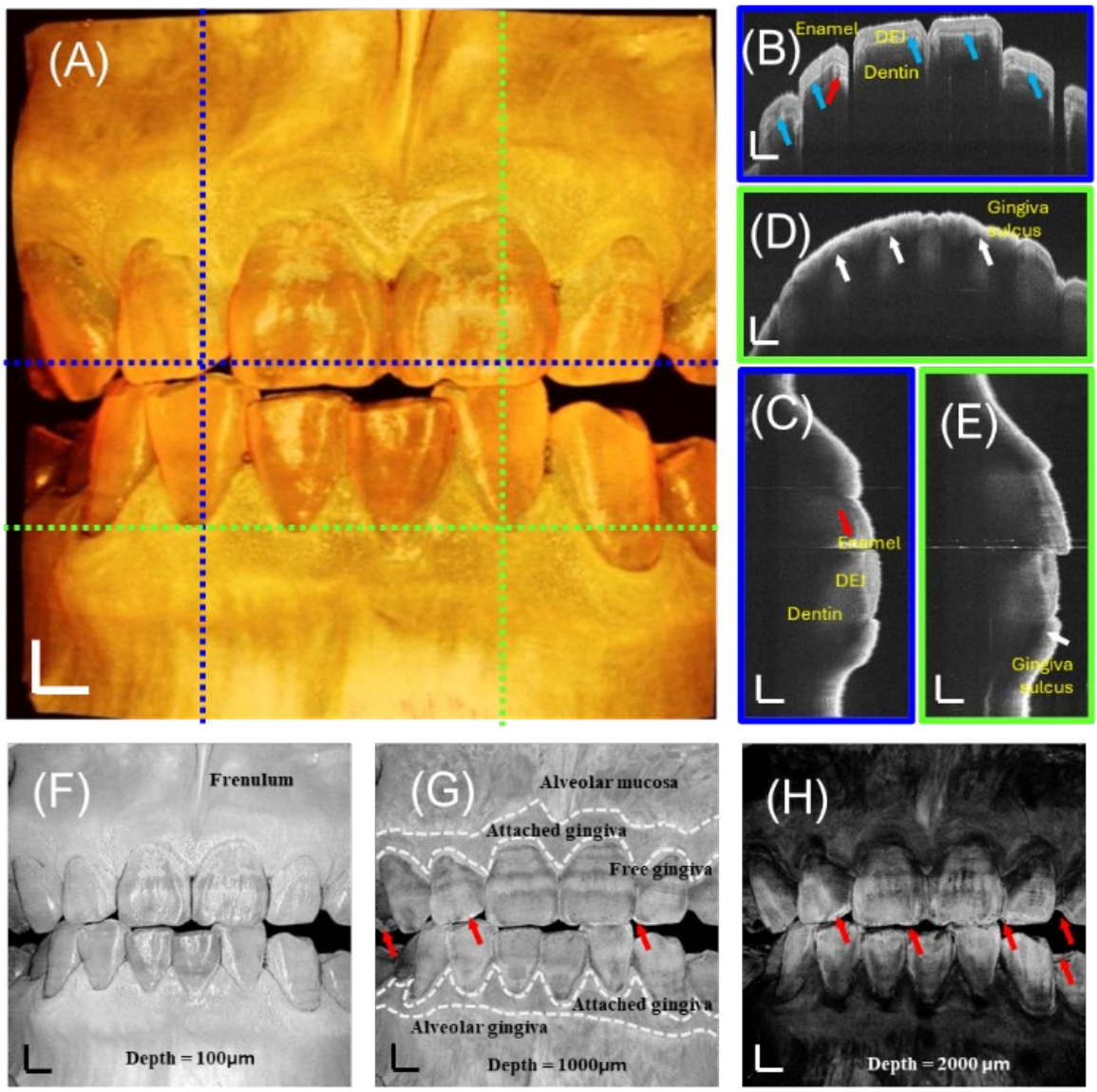

Figure 3-6. OCT structural imaging shows the oral anatomy in a wide field of view at 42mm x 42mm. (A) The 3D renders of anterior oral cavity; (B-E) Cross-sectional B-frames corresponding to the blue (B-C) and green (D-E) dash lines in (A); (F-H) En-face OCT slicing views at the depth of 100 μm, 1000 μm and 2000 μm with respect to the tissue surface. The scale bars for all the images (A-H) are 3 mm. DEJ: dentin enamel junction; Red arrows: suspicious enamel carious region; Blue arrows: DEJ; White arrows: gingiva sulcus.

Leveraging the extensive imaging range offered by the proposed OCT system, *en-face* views at depths of 1000μm (Figure 3-6G) and 2000μm (Figure 3-6H) present a comprehensive distribution map of dental wear, effectively revealing suspicious enamel carious lesions that

were not as distinct in the volume rendering (Figure 3-6A) or superficial slicing (Figure 3-6F). This detailed insight may be clinically useful to aid in the early diagnosis of potential enamel caries and offer a precise assessment of cavitated enamel caries.

Furthermore, the oral epithelium, with its high scattering property, results in increased intensity within the superficial gingival region. As depth increases, the *en-face* view distinctly delineates boundaries among various gingival units (Figure 3-6G-H). Notably, the attached gingiva region exhibits slightly elevated intensity (Figure 3-6H), likely attributed to its close attachment to the underlying bone structure. Various features, including dentin, enamel-dentin junction (blue arrows in Figure 3-6B), and gingival sulcus (white arrows in Figure 3-6D and E), are clearly distinguished in the OCT cross-sectional B-images. These visualizations offer invaluable information for clinical assessment and diagnosis. The ability to differentiate between general and suspicious lesion characteristics within the oral cavity underscores the potential of the proposed OCT system for providing *in vivo* oral anatomy for dental diagnosis.

3.3.2 *In vivo* OCTA imaging of gingiva

With the capabilities of OCTA to capture dynamic blood flow, we also conducted *in vivo* OCTA imaging of the oral cavity to visualize the vascular networks. Figure 3-7A illustrates a depth-color encoded 3D projection of the anterior oral cavity, obtained through OCTA under wide-field imaging mode, covering a depth of 2 mm, which vividly depicts a dense distribution of capillaries, small connective vessels, and larger blood vessels across the wide FoV of the human gingiva. Notably, dense capillaries and small connective vessels dominate the superficial layers of the gingival tissue, while larger blood vessels are situated in deeper regions. The *en-face*

view at a depth of 200 μm (Figure 3-7B) accentuates the distribution of capillaries and small connective blood vessels. Despite capillary sizes exceeding the lateral resolution achievable in wide-field mode, the lower density of large blood vessels and the distinct, well-spaced arrangement of capillaries facilitate effective imaging of capillary networks within the free and attached gingiva region, as shown in the inset of Figure 3-7B.

A detailed analysis at different depths reveals notable variations in the distribution of blood vessels across various gingival regions. At a depth of 200 μm with respect to the surface, capillaries and small connective blood vessels are prominent, particularly within the attached gingiva and free gingiva regions. Remarkably, the attached gingival region displays a lower density of large blood vessels in its superficial layers (Figure 3-7B-C), with a slight increase in deeper layers (Figure 3-7D). In contrast, the free gingiva region features capillaries and small connective blood vessels predominantly in the superficial layers, transitioning to larger blood vessels at deeper layers.

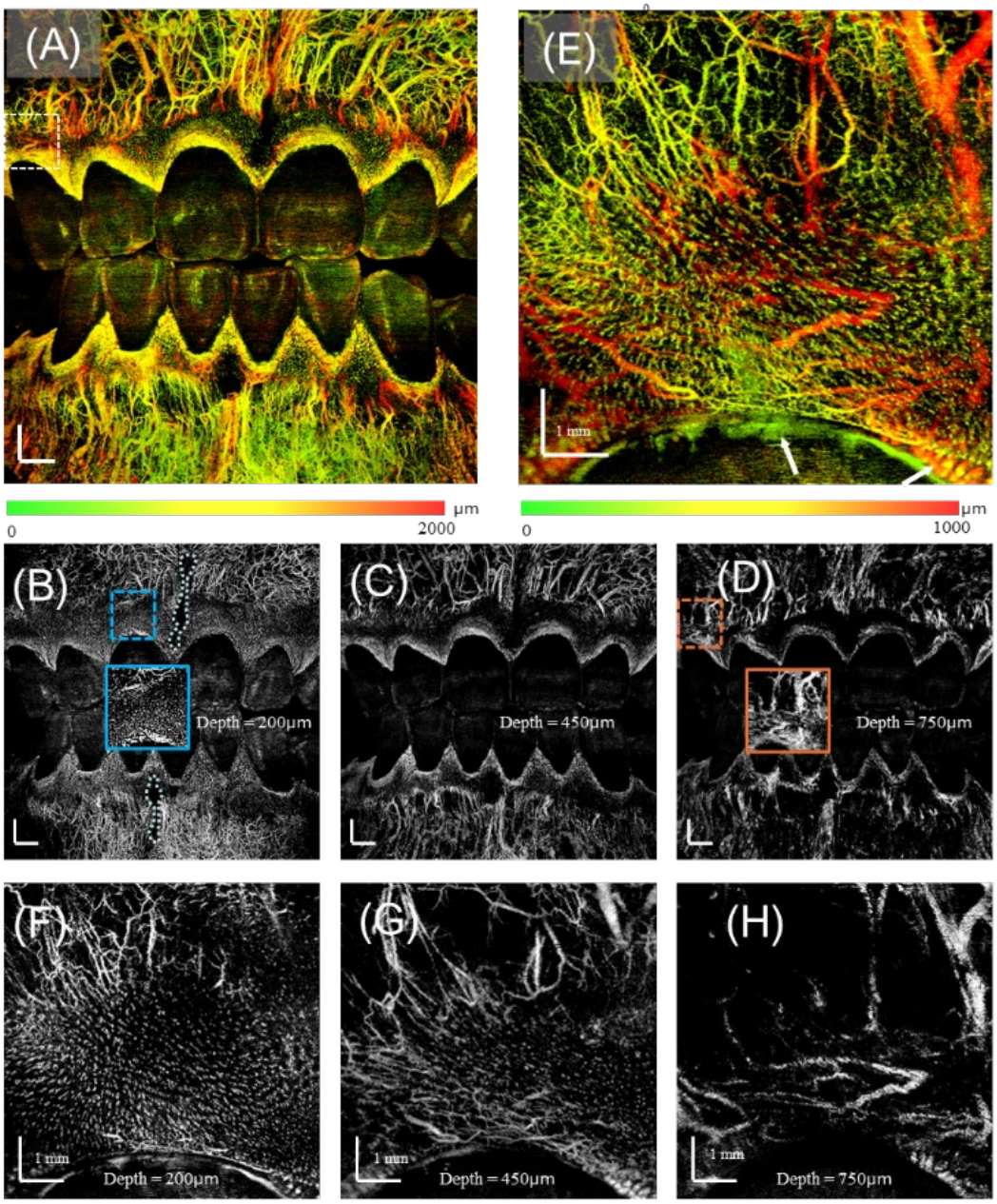

Figure 3-7. *In vivo* OCTA imaging of microcirculations within the gingival tissue of the oral cavity. (A) Depth-color encoded OCTA projection image over a 2 mm depth within the oral cavity. (B-D) *En-face* OCTA views at various depths: 200 μm, 450 μm, and 750 μm, with respect to the tissue surface. Insets in (B) and (D) are zoomed-in views of the dashed rectangular and dashed orange rectangular areas, respectively. (E) Depth-color encoded OCTA (over 1 mm) corresponding to the white rectangular area in (A) using the high-resolution imaging mode. (F-H) *En-face* OCTA views at various depths corresponding to the white rectangular area in (A) using the high-resolution imaging mode: 200 μm, 450 μm, and 750 μm, with respect to the tissue surface. The scale bars for images (A-D) are 3 mm.

Conversely, the alveolar mucosa region displays a higher prevalence of connective blood vessels and larger blood vessels, with the larger vessels predominantly located in deeper layers (Figure 3-7B-D). Additionally, *en-face* views illustrate the progressive merging of capillaries and small connective blood vessels into larger vessels as one moves from superficial to deep layers, connecting with larger blood vessels from the superficial to intermediate layers. Notably, the superficial blood perfusion in the region marked by white dots (Figure 3-7B) is subdued, attributed to the tension exerted by the frenulum when the oral cavity is exposed to the probing beam through a mouth opener during imaging, resulting in some blood to be squeezed out.

Figure 3-7E zooms into a specific region of interest from Figure 3-7A (indicated by a rectangular box) obtained with the high-resolution imaging mode. This mode, distinguished by its heightened detail, is evident in the *enface* maps at depths of 200 μm, 450 μm, and 750 μm, respectively (Figure 3-7F-H), offering a nuanced map of vessel network distribution. At a depth of 200 μm, dense capillaries are prevalent across the entire ROI, encompassing the free gingiva, attached gingiva, and alveolar mucosa regions. These results accentuate an increased distribution of connective vessels and large vessels at 450 μm, followed by a decline in connective vessels at 750 μm. Meanwhile, the prevalence of large vessels continues to expand, consistent with our observations in wide-field imaging. Moreover, high-resolution imaging reveals local features such as plaque and vessel loops (depicted by white arrows in Figure 3-7E), which can be crucial for precise diagnosis and treatment of oral diseases.

3.4 Discussion and Conclusion

In this study, we presented an SS-OCT system suitable for comprehensive oral examinations, featured with an imaging speed of 600kHz, a field of view of 42mm × 42mm and a ranging distance of 36mm. Since the increase of the optical path difference in a MZI progressively increases the interference signal frequency bandwidth that may challenge the system bandwidth, leading to an electrical dispersion that presents in the generated k-clock signal, we proposed a method to compensate for this dispersion after the OCT interference signal of interest is digitized by the data acquisition card. This is the unique contribution of this study to the development of SS-OCT system for wide field imaging applications. We have shown that such compensation is effective and necessary when imagining a target with complex topology features, for example in the imaging of oral cavity.

While recent advancements have produced swept sources with multi-MHz line speeds (up to 40 MHz), the imaging speed of SS-OCT has not kept pace with the development of laser sources. Beyond scanning speeds, data acquisition speed is another limiting factor. If an external-triggered k-clock acquisition method is chosen, the generation speed of the k-clock signal becomes a limiting factor, creating a competitive relationship among imaging speed, imaging range, and laser source bandwidth. Enhancing either of these parameters inevitably diminishes the third. All three parameters are required to consider synergistically when designing a SS-OCT imaging system that meets the purpose for specific applications.

In this work, we designed an optimal parameter configuration scheme for oral examinations. We chose to sacrifice a portion of axial resolution (i.e., spectral bandwidth) to maximize the

requirements for imaging speed and imaging range. This is mainly because there are competing factors among various parameters of the SS-OCT system under the constraints of limited performance of the existing hardware, including digital acquisition card. Considering the necessity for rapid and comprehensive oral examinations, which demand OCT systems to possess both a high scanning speed and an extensive imaging range, the only aspect that can be adjusted is the axial resolution (spectral bandwidth). In reality, based on the information available in the literature about physiological and pathological teeth and gums, it is found that the structure of oral tissues is not as complex as that of retinal tissues. The resolution requirements are relatively modest. The resolution of commonly used X-ray imaging in dentistry is typically between 75 and 200 μm [137]. In contrast, the axial resolution of commonly used SS-OCT is generally much higher than that. Therefore, there is considerable room for adjustment in the axial resolution of SS-OCT. Thus, while meeting the requirements for axial resolution in oral imaging, it is indeed possible to increase other performance parameters of SS-OCT by reducing spectral bandwidth.

To maximize imaging speed and ranging distance, the k-clock trigger signal must maintain its maximum output frequency. The proposed k-clock calibration strategy effectively mitigates the nonlinearity of electronic devices in generating high-frequency k-clock signals. It should be noted that while using a more advanced acquisition card with broader bandwidth capabilities can reduce nonlinear phase errors during OCT signal sampling, this approach will increase costs and does not address electrical dispersion from the k-clock transmission process. Furthermore, with advancements in hardware manufacturing, the proposed strategy can further enhance system performance, even beyond the current bandwidth limitations.

The choice of the laser source spectral bandwidth was deliberate; a 20 nm bandwidth can provide ~29.6 μm axial resolution in tissue, which is significantly higher than the resolution of X-rays commonly used in dentistry. It is fully capable of handling tasks related to tooth or soft tissue detection. It's worth noting that the narrowband spectrum is less affected by k-clock nonlinearity than the broadband spectrum. This is one of the reasons why a narrowband laser source was chosen in this study. The imaging field of 42 × 42 mm^2 can cover 14 human teeth, meaning the entire oral cavity can be covered in two scans. The acquisition time for a single structural image is only 4.75 seconds, allowing the majority of patients to remain stable in such a short time. The depth-resolved *en-face* and cross-sectional structure images enabled the observation of general oral cavity features, including the ability to distinguish enamel health, detect carious lesions, and visualize distinct boundaries of different types of gingival. With OCTA capabilities, we successfully visualized the blood perfusion by delivery of a macroscopic distribution map of capillaries, small connective blood vessels, and large blood vessels. When precise examination of local lesions is needed, the system can provide excellent high-precision resolution by switching objective lens and scanning protocols.

The system presented in this study is not limited to dental imaging; it is equally applicable to other fields with demanding requirements for imaging speed, field of view and ranging distance, such as dermatology, orthopedic surgery, or intraoperative applications in general surgery, and so on. Although the proposed system can achieve long-range imaging, it has limitations. At the maximum imaging distance, image resolution severely decreases due to defocusing. Combining this system with a tunable lens might be a solution to maximize image quality throughout the entire oral cavity [138,139]. Moreover, while the proposed system can

quickly scan comprehensive OCT images, the wide-field long range imaging mode increase also results in larger data sizes and longer computational times for reconstructing 3D results. This challenge underscores the need for efficient data processing solutions. Recent advancements in compressed sensing algorithms with optimized sampling strategies offer promising solutions. These algorithms can reconstruct 3D OCT image volumes from as little as 10% of the original data, significantly reducing both scan time and computational load [140].

In conclusion, we have demonstrated a high-speed and long-range wide-field OCT/OCTA system for oral cavity imaging based on a 600kHz MEMS-VCSEL swept laser source, enabling an expanded FOV of 42 × 42 mm^2 and an extended imaging range of 36 mm for OCT and OCTA imaging without compromising scanning time. We introduced a concept of electrical dispersion and a global k-clock compensation approach to improve overall performance of the proposed imaging system. We demonstrated that the system provides visualization of both macroscopic and microscopic oral environments, offering a potential non-invasive approach for diagnosing and monitoring oral diseases. We expect the proposed system will provide new opportunities for wide-field imaging applications in dentistry and other clinical fields.

4 ADAPTIVE CONTOUR-TRACKING TO AID WIDE-FIELD SWEPT-SOURCE OPTICAL COHERENCE TOMOGRAPHY IMAGING OF LARGE OBJECT WITH UNEVEN SURFACE TOPOLOGY

4.1 Background and Motivation

The development of optical coherence tomography (OCT) technology has evolved from time-domain to spectral domain implementations, eventually leading to the development of swept source configurations (SS-OCT) [1,108]. SS-OCT has gained prominence due to its capability of higher imaging speed and longer ranging distance [37,87,141], finding widespread applications in biomedical imaging fields including ophthalmology [8–10], endoscopy [115,120], dermatology [14,116,142,143], dentistry [11,127,144,145], neuroscience [122,123,146], among others.

Recent technical advancements in SS-OCT have primarily focused on enhancing imaging speed and depth ranging [60,147]. The driving force behind this trend includes the growing demand in clinical medicine for rapid acquisition of high-quality images and the needs of biomedical research for observing tissue structures and functions over larger field of view. High-speed SS-OCT enables the efficient imaging of a broader range of tissue structures within a short timeframe, providing timely information to aid the clinical decision making [79]. Moreover, the evolution towards wider fields of view (FoV) and longer ranging distance facilitates a more comprehensive understanding of physiological and pathological processes,

proving valuable in applications such as comprehensive eye examinations [36,148], whole-brain vascular visualization in neuroscience [27,149], and large FoV skin imaging [31].

However, OCT imaging quality deteriorates with the increase of depth, particularly in the case of large-field imaging [87,150]. The primary factors affecting OCT imaging quality at the system level are defocus and system sensitivity roll-off [138,151,152]. Defocus occurs when the sample is not near the focal plane while sensitivity roll-off affects the imaging quality when the sample is located too far from the zero-path difference plane. In wide-field imaging, samples are more likely to be away from the focal plan or zero path difference plane, especially with irregularly shaped samples, such as gum-line in the oral cavity. As a result, some imaged regions may appear blurred due to either defocus effect or the tissue region of interest located at relatively deep imaging positions.

To address these challenges, dentists often require OCT systems with high-speed, long-range, and wide-field capabilities that also maintain excellent image quality at larger ranging depth positions. Some studies have explored improving image quality at deeper positions by optimizing the optical system, such as using longer focal length objective lenses (lower numerical aperture) for an increased confocal depth [148]. However, this approach trades the lateral resolution with the confocal depth. Other methods focus on reducing system sensitivity roll-off by optimizing the OCT data acquisition mode, mitigating sensitivity drop caused by k-clock nonlinearity in high-speed and long-ranging modes [31]. While these methods can reduce the rate of sensitivity drop, they do not eliminate system sensitivity roll-off. Commercial OCT systems often employ autofocus devices to find the optimal focal plane for imaging, using mechanical methods to adjust the focal plane. However, this process is typically slow [153].

Using a movable probe to adjust the distance or angle between the probe and the sample can enhance image quality, but this method is impractical when the distance cannot be freely adjusted and may introduce motion artifacts [154].

The introduction of tunable lens has significantly alleviated these issues [139,155]. Acousto-optic tunable lenses (AOTL) [156]and electrically tunable lenses (ETL) are widely used in OCT to optimize imaging quality [157]. AOTL achieves focal adjustment by inducing changes in refractive index through sound waves, while ETL adjusts the lens shape and curvature by altering the electric field. Studies have utilized tunable lenses to scan multiple times at the same B-scan position, adjusting focal length during each scan and fusing the resulting images to obtain final high-quality images across the entire depth range [138,155]. However, this method significantly increases imaging time and data volume that the system and computing must handle. Other studies have reported imaging samples by searching and selecting the optimal focal length throughout the entire focal range [81], but real-time focus adjustment significantly extends data acquisition time.

Although tunable lenses can alleviate defocusing effects, system sensitivity roll-off remains an issue, especially at relatively long-ranging distances where sensitivity loss can exceed 20 dB, affecting the efficient identification of tissue structures of interest and blood flow signals at deeper positions [138]. Simultaneously adjusting both the focus and optical pathlength difference between reference and sample arms, allowing the effective imaging window to adapt along the sample surface contour, may offer further opportunities for improving image quality at different depths. This adaptive contour-tracking and scanning (ACTS) strategy, based on dual adjustment of focus and optical delay line, does not require changes in spatial distance between

the system and the sample, overcoming some limitations above and reducing motion artifacts. However, it has not yet been reported in wide-field SS-OCT, and its performance improvements and challenges in practice remain unknown.

In this paper, we present the realization of an ACTS method through the automatic and joint control of ETL in the sample arm and adjustable optical delay line (AODL) in the reference arm. The method partitions the entire system's ranging distance into several segments determined by the confocal length of the SS-OCT system. It first acquires the surface contour within a large FoV of the sample by rapid pre-scanning in the slow scan direction. The system then analyzes the surface variations and generates a personalized scanning protocol. Subsequently, it uses a shorter ranging mode to adaptively image along the surface contour in the defined segments, employing multiple confocal functions to eliminate unevenness in image signal intensity caused by multiple focuses. We detail the implementation process of this strategy, emphasizing its limitations and potential improvements. Its feasibility is validated through phantom experiments and *in vivo* oral imaging. A comprehensive analysis from multiple perspectives, including image contrast, sensitivity, signal-to-noise ratio (SNR), imaging time, penetration depth, and storage space, is conducted to evaluate the benefits and costs of this method. The paper concludes with a discussion on the practical application value, applicable fields, and future development directions of this method.

4.2 Materials and Methods

4.2.1 System setup

A high speed, wide-field SS-OCT system was constructed to demonstrate the proposed ACTS strategy (Figure 4-1). The system employed a laser source operating at 600 kHz, with a central wavelength of 1310 nm and a 20 nm optical bandwidth, theoretically providing an axial resolution of approximately 41 μm in air. The laser output was split 99:1 to power both the OCT imaging system (99%) and an auxiliary Mach–Zehnder interferometer (MZI, 1%) that was used to generate a k-clock signal for OCT signal acquisition. The optical path difference (OPD) in the MZI was set at 72 mm. With the use of single-edge and double-edge sampling modes, the ranging distance of the system was 18 mm (short range mode) and 36 mm (long range mode), respectively. Note that this system was designed to interchangeably employ single-edge and dual-edge sampling modes when triggering and capturing the OCT interference signals of interest, where the short ranging mode significantly reduces the data volume that must handle, an important consideration for large field of view imaging.

n the OCT system, a 90:10 coupler splits the light beam into the reference arm (10%) and the sample arm (90%). In the sample arm, the light passed through a circulator (Thorlabs, USA) and was collimated using a fiber collimator, generating in a collimated beam with a diameter of approximately 2.8 mm. The beam then traversed through an ETL (Opotune Ltd) before being directed to a galvo mirror. The response time of the ETL is 2.5 ms, with a stabilization time of 15 ms. A f-theta lens with a focal length of 100 mm was employed in the sample arm to achieve a large FoV of up to 42×42 mm.

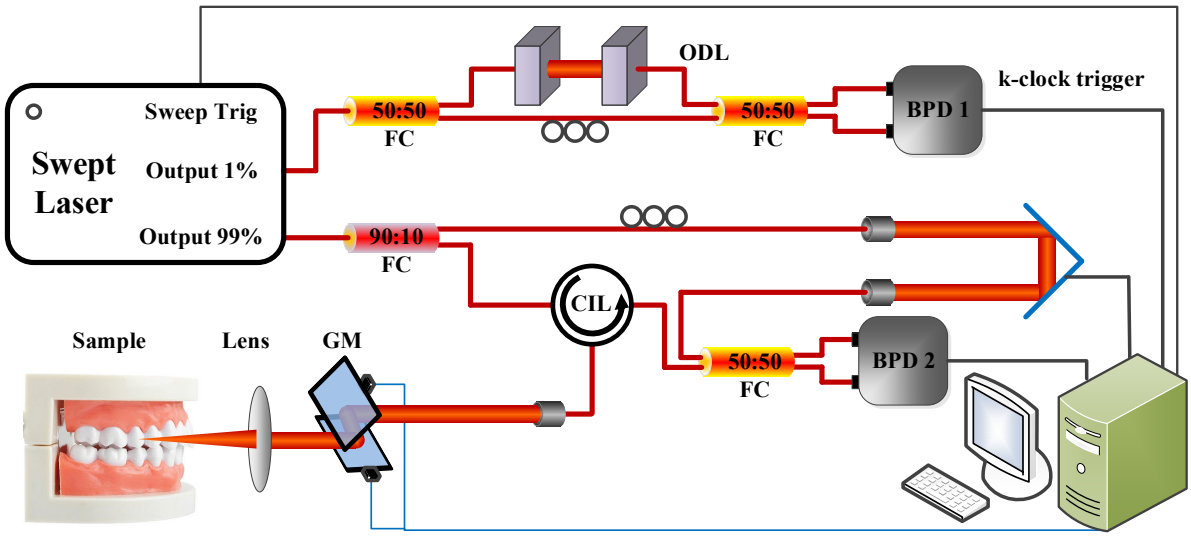

Figure 4-1. Schematic of the 600 kHz SS-OCT system. FC: fiber coupler; CIR: circulator; ODL: optical delay line; AODL: adjustable optical delay line. PC: polarization controller; BPD: balanced photodetector; ETL: Electrically Tunable Lenses. GM: galvanometer.

I In the reference arm, an electrically adjustable optic delay line (AODL) was used to align the optical pathlength with that of the sample arm. The response speed of the AODL is 6 mm/s. The backscattered light from the sample was directed to a 50:50 beam splitter through a circulator and combined with the light from the reference arm. Subsequently, the optical interference signal was converted to electrical signals through a balanced photodetector. The signal was then processed and collected using a digitizer (ATS 9630, AlazarTech, Canada). To ensure synchronized data collection, all hardware components, including ETL, galvo scanners, AODL, and digitizer, were synchronized using the laser sweep-trigger and controlled through a customized LabView program, including the procedures required by the ACTS (see below section).

4.2.2 Adaptive contour-tracking scanning

The purpose of ACTS is to enable the system to adaptively adjust the focal position relative to the sample of interest. This is achieved using an automated tunable lens that can alter the focal position during imaging, in conjunction with adjusting the reference optical delay line to ensure the sample of interest falls within the effective OCT imaging window. This adjustment is facilitated by near real-time feedback from the sample surface contour information, initially obtained through a rapid pre-scan of the sample. This strategy allows the effective OCT imaging window to follow changes in the sample contour, optimizing image quality within a wide FoV. Note that the effective OCT imaging window refers to the imaging depth range defined by the confocal depth of the system, over which range the lateral resolution remains relatively constant. Figure 4-2 illustrates the entire scanning strategy workflow.

Taking a phantom sample as an example (Figure 4-2A), the sample first undergoes a rapid pre-scan (Figure 4-2B), which involves a sparse scan along the slow scan direction (approximately 0.1sec for 20 B-frames) using the long-range scanning mode (36 mm). The primary purpose of this step is to determine the rough surface contour of the sample. The system processes the pre-scans by removing isolated points, yielding slow-axis B-scans (Figure 4-2C), with which the surface contour is then extracted. This contour information is used to partition the entire ranging distance (36mm) into several segments based on the system's confocal depth (Figure 4-2D). The intersections of the sample's surface contour with these segments indicate when the system's focus and AODL are required to adjust.

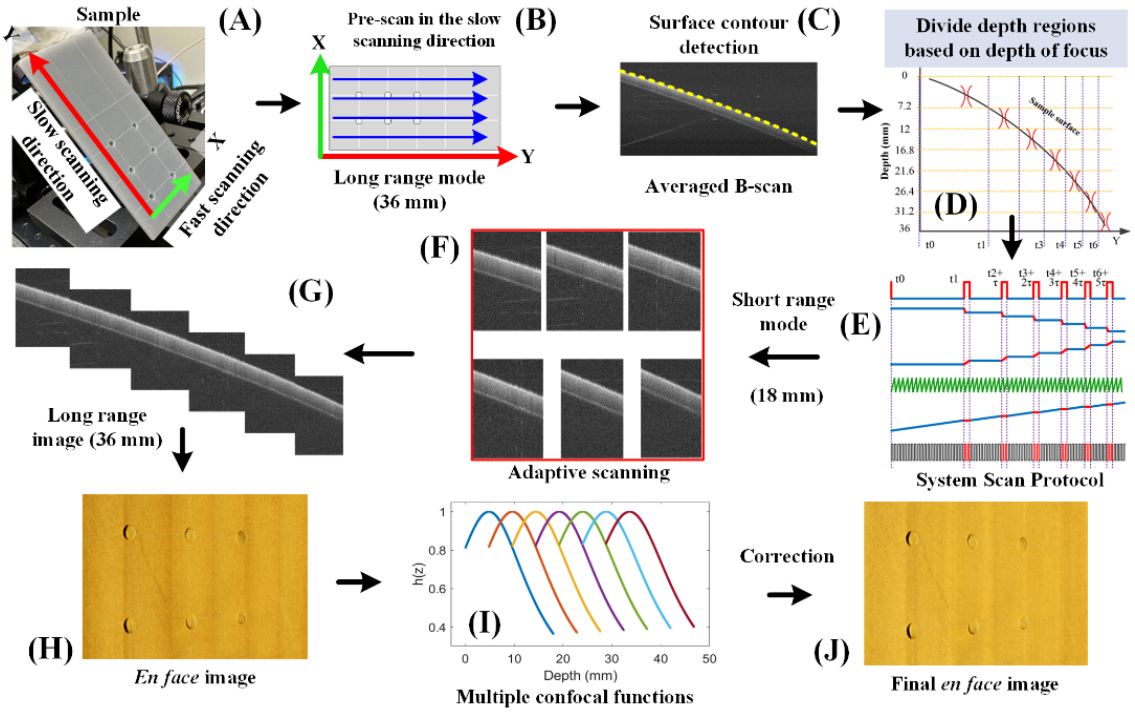

Figure 4-2. Flowchart of the adaptive contour tracking and scanning (ACTS) strategy. (A) Photograph showing a phantom sample of interest oriented in a big slope towards the slow scan direction. (B) Rapid pre-scan protocol where the fast axis (B-scan) marked as X and the slow axis marked as Y. (C) B-scan image along the Y-scan direction and the surface contour detection. (D) Dividing the entire ranging distance into segments based on the confocal depth of the system, and marking the time moment when the system is required to adjust the ETL and AODL. (E) Generation of scanning protocol for each segment. (F) Automatic stage-wise scanning to obtain 3D images for each segment. (G) Fusing the images at each segment to form final 3D image with increased ranging distance. (H) Depth-collapsed *en face* image of the final image. (I) Confocal functions of the system when imaging each individual segment. (J) Depth-collapsed *en face* image of the finally confocal-depth corrected 3D image.

Based on the response speed of the ETL and AODL, sufficient time is allocated for system to act to adjust, and an adaptive contour-tracking scanning protocol is then automatically generated (Figure 4-2E). Instructed by this protocol, the system the performs stage-wise scans of the sample using the short-range scanning mode (18 mm) (Figure 4-2F). By combining all stage-wise images based on the adjusted distance of the AODL (Figure 4-2G), a true 3D image

over a long ranging distance and the entire FoV is obtained (Figure 4-2H). At each segment (effective imaging window), the reflected light strength along the depth can be affected by the system confocal function, which requires compensation. Therefore in the last step of the processing, the confocal functions at each segment (Figure 4-2I) are used to compensate the light strengths in the OCT images, leading to final compensated wide field OCT image (Figure 4-2J). Detailed descriptions of each step are provided below.

4.2.3 Selection of focal length of objective lens

The ETL alters the focal length by altering the driving current (ranging from -290 mA to 290 mA). Increasing the current converges the light beam, while decreasing it diverges the beam. To maintain OCT system stability, high-speed galvo-scanner is typically smaller in size (3mm x 3mm in this study), which may not be enough to cover the entire diverging beam, leading to energy loss. To address this issue, we tested the energy loss after the galvo-mirror due to the ETL with a function of the driving currents. Because of the inherent properties of the electroactive deformable material in ETL, the ability to alter focal length differs when the driving current increases compared to when it decreases. Figure 4-3A illustrates the measured light energy after the galvo-mirror during the processes of increasing and decreasing driving currents. The green area marks the region where the system can maintain relatively high energy, within 1/3 of the maximum energy loss.

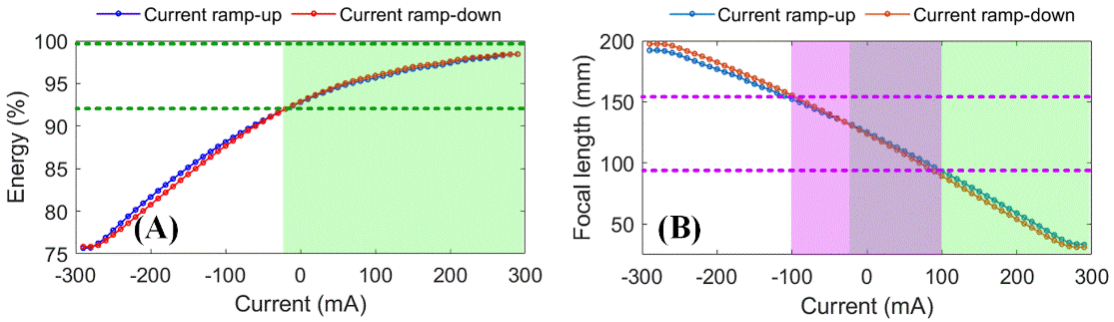

Figure 4-3. Selection of focal length range of lens group that determines the system numerical aperture (NA). (A) The measured light energy as a function of the driving current, either increasing (blue) or decreasing (red) current. The marked green area represents the region where the system can maintain relatively high energy utilization. (B) The focal length as a function of increasing (blue) or decreasing (red) driving current. The gray-purple area represents the range where the system can maintain stable and optimal operation, in terms of both efficient usage of the light beam and the confocal depth.

The ability of the ETL to alter focal length exhibits a smaller range when the current increases compared to when the current decreases. This characteristic can impact on the overall system performance. We tested the alternation of focal length determined by the lens system composed of ETL and f-theta lens together (which determines the eventual imaging NA), as shown in Figure 4-3B. When the current varies within the range of -100 to 100 mA (marked purple), the focal length is least affected by either increasing or decreasing the driving current. The marked green area (from ~-10 mA to 300 mA) indicates the region where the system possesses minimal energy loss. The overlap between these two regions represents the selected focal length range in this study. As a result, the tuning range for the focal length is selected from 95mm to 130mm.

4.2.4 Generation of scanning protocol and control signal

The ACTS strategy divides the entire imaging depth range into depth segments, each segment corresponding to the effective imaging window. When the sample transitions from one depth segment to another, the system needs to adjust the focal length and the reference optical delay line. This adjustment is crucial to maintain high resolution throughout the entire depth range. Therefore, determining each segment is of great importance. In this study, the segments are determined based on the confocal depth (Rayleigh length). Long-range mode was employed during the pre-scanning process to determine the indicative profile of the sample. In this mode, the entire ranging depth is 36 mm, and the minimum focal length obtained from the previous section is 95 mm. The lateral resolution at the beam waist is approximately 55 μm, corresponding to a Rayleigh length of 2.4 mm, i.e., a confocal depth of 4.8mm (effective imaging window). In OCT imaging, the sample position is typically maintained at a certain distance from the zero optical path planes to avoid image wrapping. In this study, we reserved a buffer zone of one Rayleigh length. The remaining 33.6mm was divided into 7 segments, each 4.8mm (Figure 4-4A).

In Figure 4-4A, the black curve represents the sample surface contour obtained from the fast pre-scan. This contour covers all 7-depth segments, which provide the time stamps where the horizontal coordinate indicates the time points at which the system is required to adjust the focus and reference optical delay line. For each time stamp, an additional time interval, τ, is added to the time stamps, determined by the response and stabilization time required for ETL and AODL to act. This process generates the control signal sequence shown in the first row

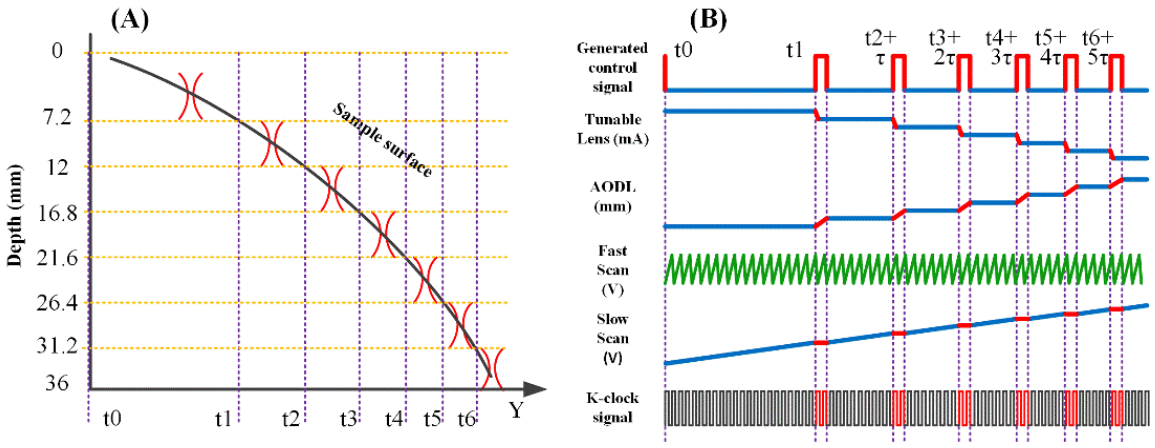

Figure 4-4. Schematic diagram of control signal and scanning protocol generation. (A) Determination of time stamps t0, t1, … t6. The black curve represents the sample's surface contour. The orange line indicates depth segments determined by the confocal depth (7 segments in this case). The purple vertical lines give the time stamps where it requires the system to activate the ETL and AODL to adjust the focal length and reference optical delay line. (B) Generation of control signal and scanning protocols for each segment in (A). The positions marked red denote the time stamps to inform the system to adjust and the time duration, τ, required for the ETL and AODL to act. From top to bottom, 1) control time sequence generated to inform the system when to adjust the ETL and AODL, 2) corresponding driving current to drive the tunable lens at each defined segment, 3) corresponding curve to tell the AODL where to move, 4) driving voltage to drive the galvo-scanner in fast-scan axis (B-scan), 5) driving voltage to drive the galvo-scanner in slow-scan axis (C-scan), and 6) k-clock trigger signals for data acquisition generated by the auxiliary MZI.

of Figure 4-4B. Data acquisition was initiated with the control signal set to a low level and ceased upon its transition to a high level, optimizing the efficiency of data streaming. Due to the significantly faster response of the ETL compared to the AODL, the selection of τ is dominated by the AODL. It takes 0.8s for the AODL to move 4.8mm. Thus, to ensure system stability, τ = 1.5s (including start-up and stop time) was allocated. The controlling and scanning protocol are then automatically generated based on this process (Figure 4-4B) where the control signals are given for tunable lens, AODL, fast scan, slow scan, and k-clock for data acquisition, respectively. This protocol finally instructs the system to perform the adaptive scans of the

sample. We refer to this method of dynamically tracking the imaging window along the sample surface contour as adaptive contour tracking and scanning (ACTS).

To demonstrate the system's performance, the ACTS scanning protocol was designed to include 1500 × 1500 A-lines in OCT imaging mode and 1500 × 1500 × 4 A-lines in OCT angiography (OCTA) mode, covering an approximately 42 × 42 mm² field of view. In addition to provide a large field of view, this scanning protocol achieves a frame rate of approximately 300 Hz, similar to conventional OCT devices, which enhances contrast for OCTA imaging, enabling detailed visualization of vascular structures in the oral cavity.

4.2.5 System performance evaluation

This study employed two scanning modes, the long-range and short-range modes, with ranging distance of 36 mm and 18 mm, respectively. These were achieved by employing either k-clock dual-edge triggering or single-edge triggering. Traditional OCT often uses the long-range mode to cover large variations in sample contours in wide field imaging applications. However, ACTS allows the effective imaging window to slide along the sample surface contour for sampling and scanning, eliminating the need for an excessively long imaging range to cover the entire sample structure. Therefore, the long range scanning mode is only used to obtain the surface profile of the sample, while the short-range scanning mode (18mm) is used for actual OCT imaging of the sample.

We analyzed the system sensitivity roll-off curves for both scanning modes under two conditions: with and without an objective lens. Without an objective lens, the system only has the ETL installed but in a "sleeping" state (i.e., incident and exit light are both parallel). The

roll-off curve was obtained by moving a reflector (as the sample) placed in the sample arm. In this situation, system sensitivity is only related to the ranging distance (i.e., OPD). With an objective lens, the system sensitivity is related not only to the ranging distance but also to the focal position. To highlight the advantages brought by the joint adjustment of focus and AODL, we compared the roll-off curves with the situation where only the focal length was altered without altering the OPD.

Figure 4-5A and 5C illustrate the roll-off curves of the system without an objective lens in the long-range and short-range modes, respectively. The 3dB roll-off distances are 13 mm and 7 mm, and the stable axial resolution distances are 28 mm and 13 mm, respectively. It is evident that in the short-range mode, the roll-off rate of system sensitivity and axial resolution is much faster than that in the long-range mode. Figure 4-5B and D show the roll-off curves of the system with an objective lens installed in the long-range and short-range modes. It can be observed that, in the presence of an objective lens, the focus is the primary factor affecting the system's sensitivity. The system can maintain high sensitivity only within the confocal depth, highlighting the importance of dynamic focusing in maintaining the imaging quality.

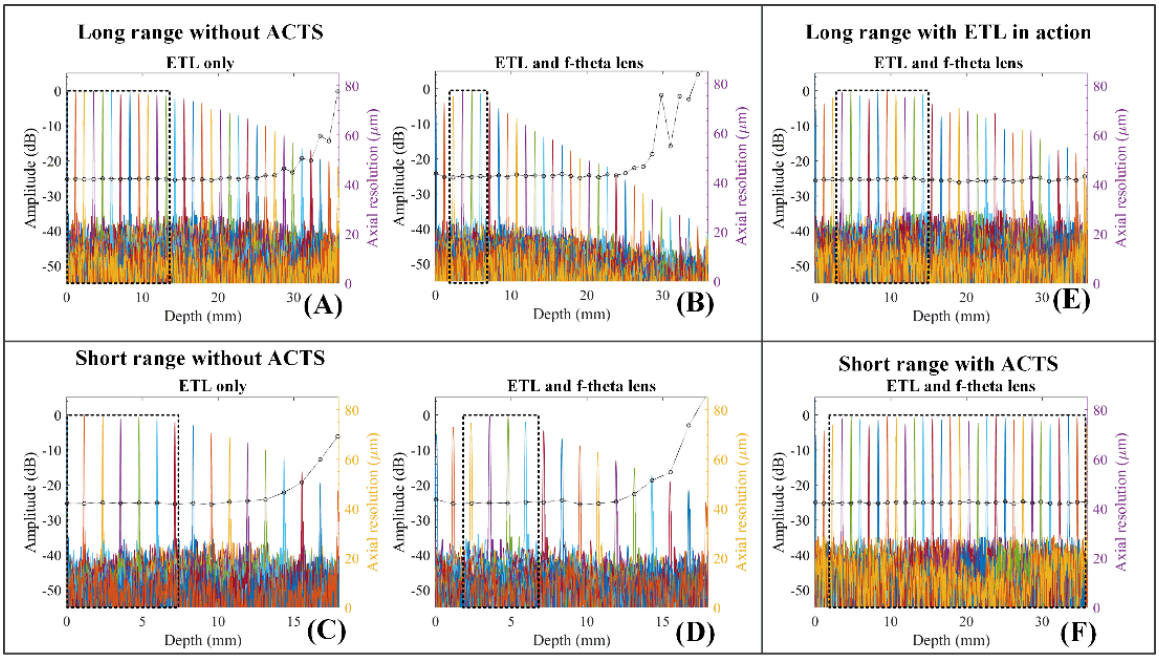

Figure 4-5. Sensitivity and axial resolution in different ranging-modes. (A, C) Roll-off curves of the system without objective lens and ACTS in the long-range and short-range modes. The black square box outlines the depth range where the sensitivity drop is less than 3dB. (B, D) Roll-off curves of the system with an objective lens but without ACTS in the long-range and short-range modes. (E) Roll-off curve of the system with an objective lens and ETL modulation in the long-range mode. (F) Roll-off curve of the system with ACTS in the short-range mode.

Figure 4-5E displays the roll-off curve under the condition of only adjusting the system's focal length (i.e., dynamic focusing). Compared to Figure 4-5C, the system's sensitivity and axial resolution have been greatly improved, especially in the deeper regions. However, the system sensitivity roll off is not eliminated. The decline of the sensitivity is similar to that in Figure 4-5A, indicating that the OPD is the main factor responsible for deteriorating the system sensitivity.

Figure 4-5F presents the system's roll-off curve obtained using the proposed ACTS. Throughout the entire depth range of 36mm, both sensitivity and axial resolution are maintained at a consistently high level. It is worth noting that each mirror reflection signal in Figure 4-5F

is obtained through the short-range acquisition mode, and almost the entire depth range is within the 3dB roll-off range.

4.2.6 Elimination of multiple confocal effects

As seen from the previous section, the sensitivity roll-off curves with the objective lens exhibit a significant degradation across the entire imaging depth range, affecting imaging contrast. Due to the focus adjustment along the entire depth range, the signal strength in the slow scan direction fluctuates when the ACTS is in action (Figure 4-6A). In this study, a multi-confocal function was employed to compensate for this effect. Confocal function, $h(z)$, and Rayleigh length, zR, are described as:

$$h_m(z) = \left[\left(\frac{z - zf_m}{\alpha z R_m}\right)^2 + 1\right]^{-1} \tag{4-1}$$

$$zR_m = \pi n \left(\frac{1}{2}\Delta X_m\right)^2 / \lambda \tag{4-2}$$

where, z represents depth, measured in mm. m represents the depth-segment number. zf_m denotes the focus position. α is used to distinguish specular reflection (α=1) from diffuse reflection (α=2) [158]. n is the refractive index, ΔX_m is the lateral resolution. λ is the central wavelength of the light source.

We used Zemax software to simulate the focusing process of the lens system (ETL and objective lens) as a function of focal length (Figure 4-6B). The ETL was designed with a static offset and a current-controlled lens, allowing for a dynamic focal tuning range from -666 mm to 286 mm. The objective f-theta lens (f = 100 mm and d = 75 mm) was positioned at a fixed

distance of 50 mm from the ETL, as per our OCT prototype configuration. The system input was specified as a collimated beam with a wavelength of 1310 nm. During the simulation, we adjusted the ETL focal length to control the entire system focal length within the range of 95 mm to 130 mm and measured the corresponding spot sizes.

Figure 4-6C shows the curve of the system's lateral resolution as a function of the focal length. In Figure 4-6D, the variation of Rayleigh length with focal length, calculated using equation 4-2, is presented. Figure 4-6E illustrates the single-focus confocal function, while Figure 4-6F represents the multi-focus confocal function curve when the focal position is adjusted from 4.8 to 33.6 mm. For the OCT scans at each depth-segment, we used the corresponding confocal function h_m(z) to correct it along the depth direction. This involved dividing each point of the A-scan signal by the corresponding confocal function curve, resulting in a more uniform sensitivity across the entire ranging distance of 36 mm (Figure 4-5F).

4.2.7 Imaging quality evaluation

In order to quantify the improvement of the ACTS on image quality, we adopted three metrics: contrast, signal-to-noise ratio (SNR), and penetration depth for quantitative comparison. Image contrast is commonly used to describe the difference in grayscale values between the target region and the background region, calculated by.

$$C = \frac{I_{target} - I_{background}}{I_{target} + I_{background}} \tag{4-3}$$

where I_{target} and $I_{background}$ represent the signal intensities in the target and background regions, respectively. In practical applications, taking a phantom sample as an example, the target region

is defined as the area below the sample surface to a depth of 2 mm, roughly corresponding to the penetration depth of SS-OCT in the phantom.

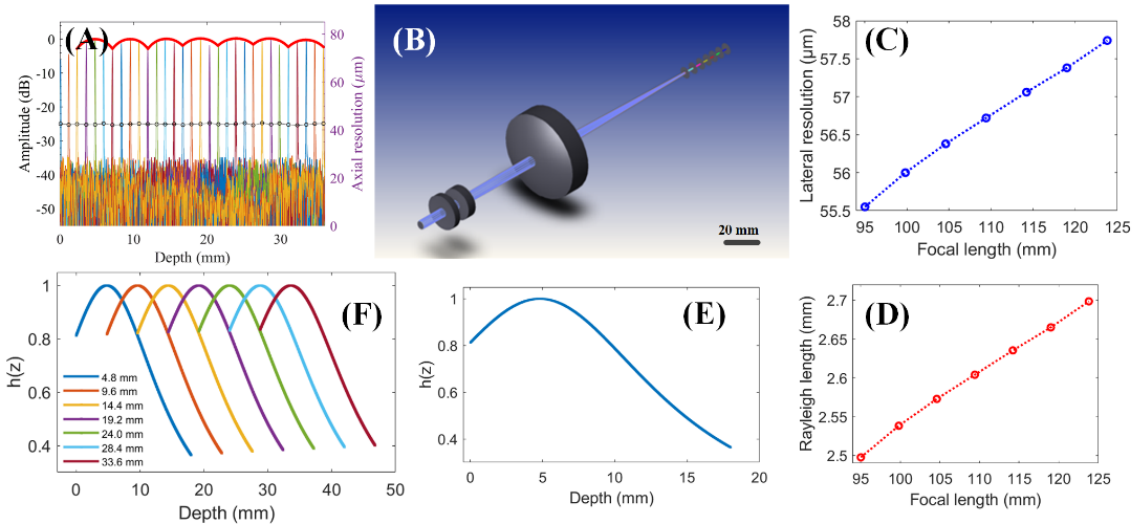

Figure 4-6. The Generation of the multi-confocal function. (A) Roll-off curve obtained by the adaptive contour tracking scanning strategy. The red curve represents the envelope of sensitivity. (B) Simulation of the focusing process of the lens system using Zemax software. (C) Lateral resolution as a function of the focal lengths of lens system. (D) Rayleigh length as a function of the focal lengths. (E) single-focus confocal function. (F) multi-focus confocal function curve when the focal position is adjusted from 4.8 to 33.6 mm.

SNR represents the relative strength between signal and noise in an image, calculated by

$$SNR = 10 \times \log_{10}\left(\frac{P_{Signal}}{P_{noise}}\right) \tag{4-4}$$

where P_{signal} represents signal power, calculated by $\sum I_{signal}^2/N_{signal}$ with I_{signal} being the signal intensity. P_{noise} represents noise power, calculated by $\sum[I_{noise} - M_{noise}]^2/N_{noise}$ with I_{noise} being the noise signal and M_{noise} representing the mean of the noise. N_{signal} and N_{noise} are the number of signal pixels and noise pixels in the region of interest.

Penetration depth is evaluated by thresholding the SNR. This involves establishing a specific SNR threshold, whereby pixels in the image surpassing this threshold are categorized as signal, while those falling below the threshold are designated as noise. The calculated thickness measured between the sample surface and the thresholded boundary serves as an indicator of the system's penetration depth for that specific sample.

4.3 Results

4.3.1 Phantom study

The feasibility of the ACTS strategy was tested (Figure 4-7) using flat and right-angled objects that were 3D printed, with their photographs shown in Figure 4-7A and F, respectively. The sample was scanned with the OCT beam pointing to it from the left. Figure 4-7B and G show the imaging results of the two samples along the slow scan direction using traditional OCT in long-range mode. The ranging distance was 36mm, and the focal plane was positioned at 4.8mm away from the zero-delay line plane. It can be observed that the imaging quality at the focal plane is high, but as the imaging depth increases, the image quality significantly deteriorates. This is a direct result of both the confocal depth and the system sensitivity roll off. Figure 4-7D and I depict the 3D images obtained by traditional OCT, showing a gradual decrease in image brightness, contrast, and clarity with increasing ranging depth.

Figure 4-7C and H show the B-scans in the slow scan direction obtained by the ACTS, where the short-range scanning mode was employed. The effective imaging window adaptively adjusted along the sample surface contour, providing exceptionally high imaging quality at all

depth positions. Figure 4-7E and J depict the 3D images obtained by the ACTS, with signal strength remaining consistent with increasing depth.

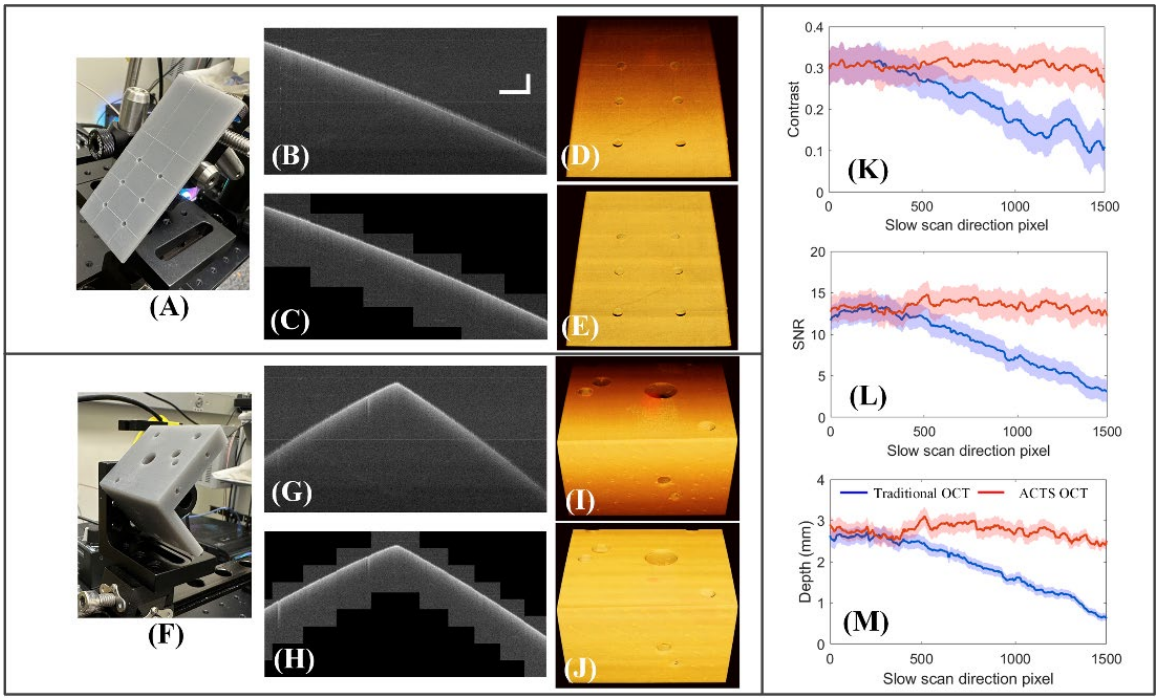

Figure 4-7. Imaging the phantom samples. (A, F) Photographs of the flat and right-angled samples. (B, G) B-scan images in the slow-scan axis obtained by traditional OCT. (C, H) B-scan results in the slow-scan direction obtained by adaptive contour tracking OCT. (D, I) 3D imaging results obtained by traditional OCT. (E, J) 3D imaging results obtained by adaptive contour tracking OCT. (K, L, M) Statistical results of image contrast, signal-to-noise ratio, and penetration depth in the slow-scan direction for the flat sample. Scale bar in (B) = 5mm

For a more intuitive comparison between the two imaging methods, we statistically analyzed the image contrast, signal-to-noise ratio, and penetration depth using the first sample, as shown in Figure 4-7K, L, and M, respectively. The blue curve represents the results of traditional OCT, while the red curve represents the results of the ACTS. The shaded areas indicate their respective standard deviations. The statistical results demonstrate that for traditional OCT, compared to shallow positions, the image contrast decreases from 0.3 to 0.1 at deeper positions

(a decrease of 67%); the signal-to-noise ratio decreases from 13 dB to 3 dB (a decrease of 77%); and the penetration depth decreases from 2.6 mm to 0.7 mm (a decrease of 73%). In contrast, the ACTS does not show a significant decrease over the entire depth range. Importantly, the data volume was only half that of traditional OCT. However, a price paid here is an increase in total imaging time by 7.5s (5 adjustments, each lasting 1.5s). The second sample (Figure 4-7F) required a total of 9 adjustments, resulting in an additional time consumption of 13.5s.

4.3.2 in-vivo imaging oral cavity

Next, we applied the proposed ACTS strategy for wide-field imaging of the human oral cavity. We defined the direction with significant physiological curvature (i.e., left-right direction) as the slow scan direction and the up-down direction of the teeth as the fast scan direction. For comparison, we also imaged the oral cavity by using the traditional OCT scan protocol with a long-range scan mode and with the focus adjusted to a position that was approximately located at the canine tooth.

Figure 4-8 shows the imaging results of the oral cavity in one human subject with the conventional OCT scan protocol that provides both the volumetric structural (Figure 4-8A) and microvascular (Figure 4-8B) information. The scan field of view was 42mm x 42mm, covering upper and lower right quadrant of the total 12 teeth, where there is a significant curvature in the gumline. The imaging time for structural scan alone was 4.75 sec, and that for both structural and blood flow imaging (OCTA scan protocol) was 19 sec. It is apparent that the image quality for both the structural and blood flow OCT images decreases with the increase of ranging distance, where the contrast at the regions near molar teeth are diminishing (pointed by white

arrows). In addition, the vessels appeared blurred due to the defocus of the OCT beam at those regions. This is because the regions near molar teeth are located away from the focal and zero-delay line planes, causing blurring and reduced contrast and signal strength in the final images. For better scrutinizing the results, the microvascular image is zoomed for upper (Figure 4-8C) and lower gum (Figure 4-8D) regions, where the challenges of wide field of view imaging of uneven samples are clearly appreciated.

In contrast, ACTS OCT maintains high resolution and signal strength throughout the entire FoV (Figure 4-9). The issues observed in the conventional scan protocol are mostly mitigated. Note that in ACTS strategy, the number of segments for effective imaging window was determined to be 5 in the rapid pre-scan mode for this subject. And compared to the conventional OCT scans (Figure 4-8), the imaging time consumed an additional 7.5 sec of acquisition time, due to the need of moving from one segment to another.

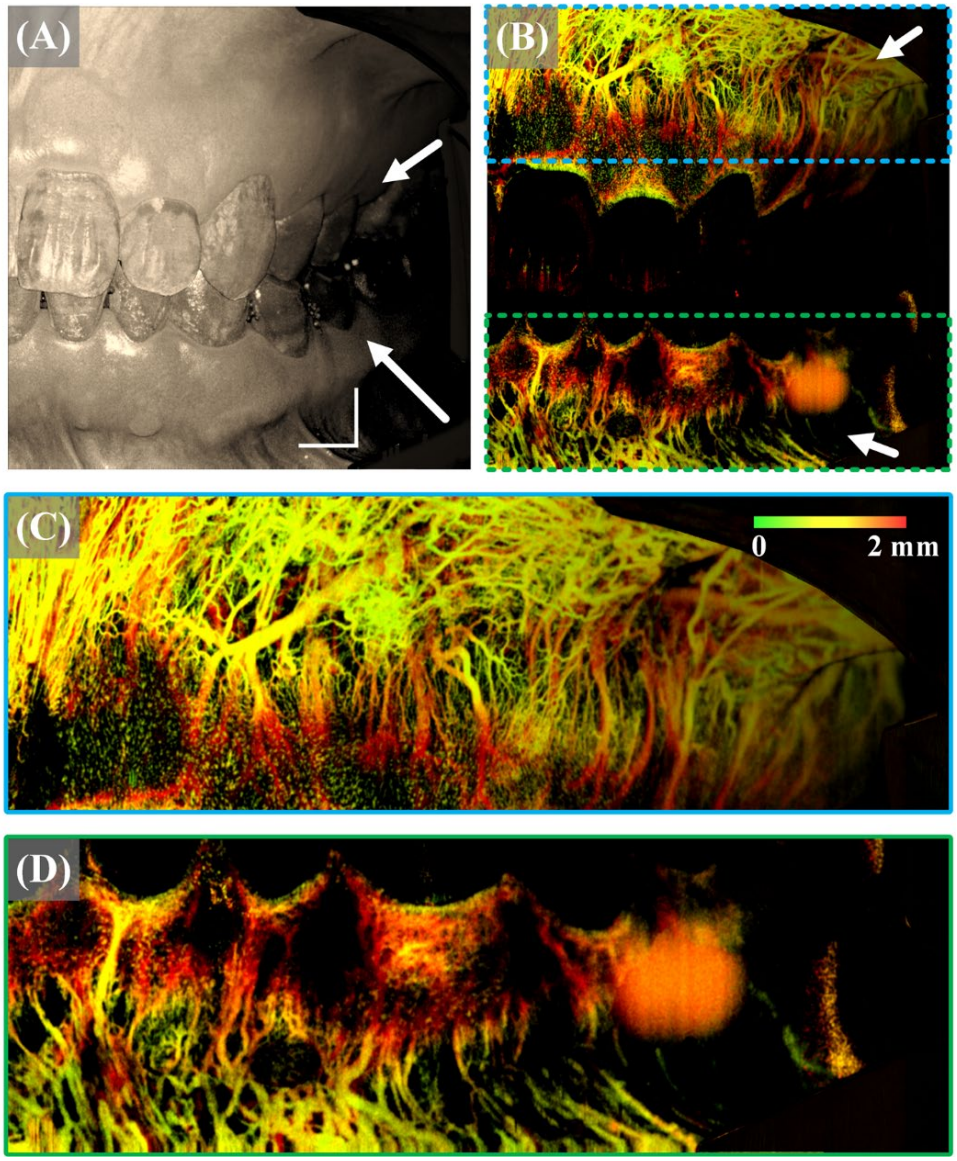

Figure 4-8. *In vivo* imaging of the human oral cavity using conventional OCT scan protocol with the long-ranging mode (36 mm). (A) 3D rendering of OCT structural information showing upper and lower right quadrant of the oral cavity, covering a total of 12 teeth. (B) corresponding microvascular image within gingival tissue. It is apparent that the regions of incisor teeth are seen with excellent quality while those near the molar teeth (pointed by white arrows) are diminished in imaging quality in both the structural and microvascular images due to significant curvatures from the incisor to molar teeth. (C) and (D) are zoomed images of the upper and lower gingival regions marked as blue and green boxes in (B), for scrutinization. Scale bar in (A) = 5 mm.

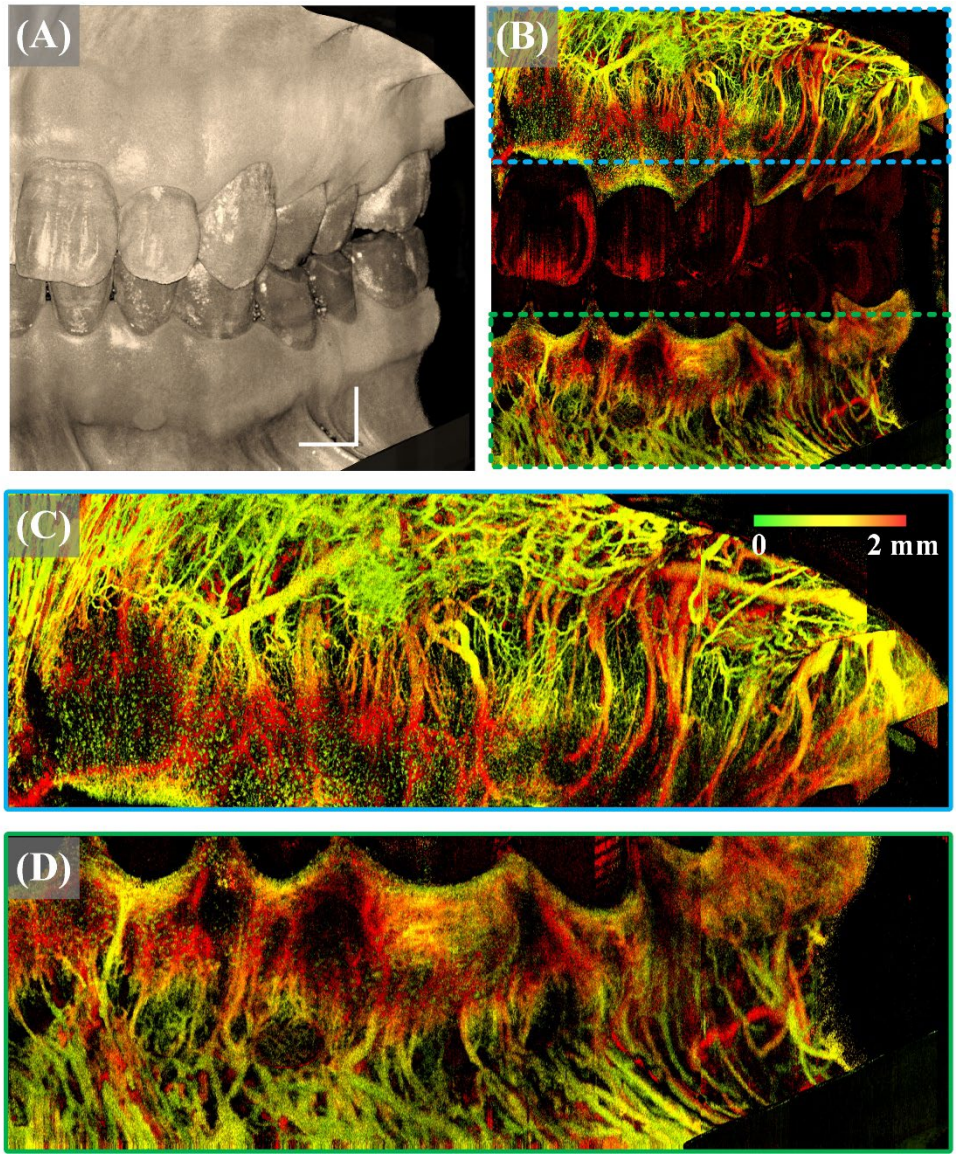

Figure 4-9. *In vivo* imaging of the human oral cavity using the proposed ACTS strategy with the short-ranging mode (18 mm). (A) 3D rendering of OCT structural information showing upper and lower right quadrant of the oral cavity, covering a total of 12 teeth. (B) the corresponding microvascular image within gingival tissue. It is apparent that the ACTS OCT maintains high resolution and signal strength throughout the entire FoV. For better appreciation of the ACTS advantages, (C) and (D) are zoomed images of the upper and lower gingival regions marked as blue and green boxes in (B), respectively, for scrutinization. Scale bar in (A) = 5 mm.

Such wide field imaging could be useful in aiding the clinical diagnosis of oral diseases. For example, OCT structural information may be used to detect tooth structures, including enamel

and dentin, aiding in the detection of pathologies such as caries, tooth fractures, and enamel wear. OCTA image provides information about the gingival vascular system, which may be used to assess the blood flow in the gums, improving our understanding of inflammation, gum diseases, and blood flow recovery after gum repair surgeries. It may also be envisioned that OCT can be used in conjunction with other imaging modalities, for example 3-shape topological tool [159] or simply a camera image, to provide complementary information in aiding clinical decision making. In this case, OCT images may be fused together with the images provided by other imaging technologies to present to dentists for better scrutinization of the relationships between topology, microstructural and microvasculature within the oral cavity. Figure 4-10 provides such an example that fuses the OCT structural (Figure 4-10A) and microvascular (Figure 4-10B) images with the camera RGB photo of the oral cavity. Note here that the teeth information was extracted from the 3D OCT structural image and retained (Figure 4-10A) for image fusing purpose in this exercise. We believe this comprehensive image could be useful to provide dental professionals with convenient and comprehensive oral health information.

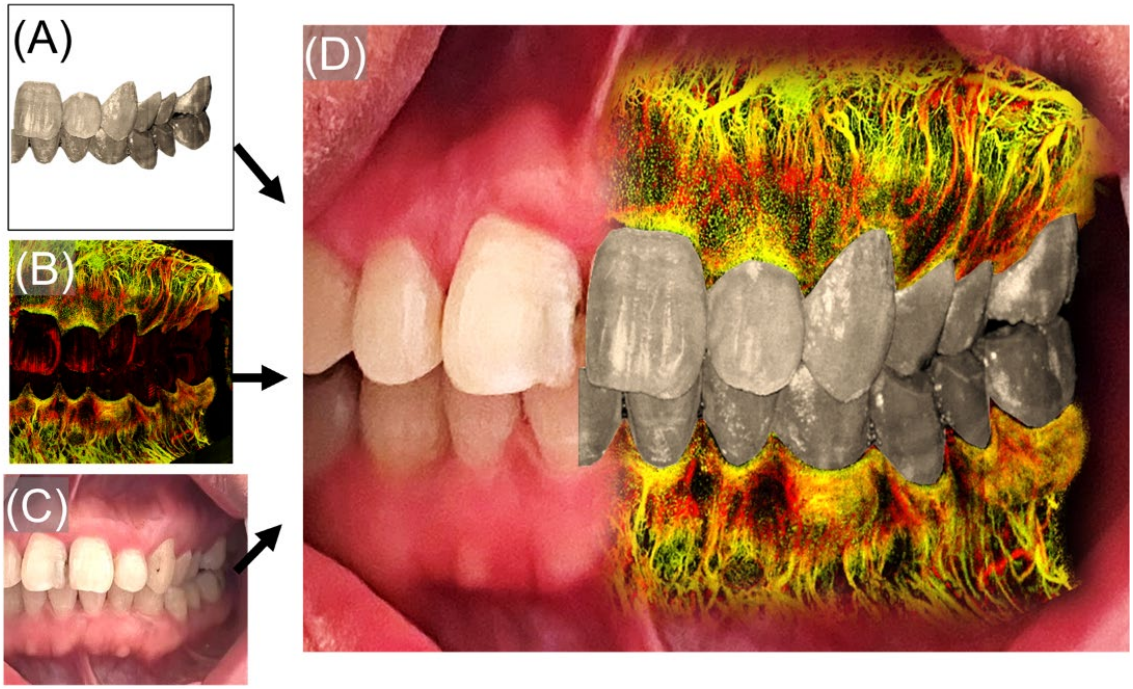

Figure 4-10. Example of fusing and registering OCT and OCTA images with RGB photograph of the oral cavity. (A) Extracted teeth information from 3D OCT structures, (B) OCTA microvascular image, and (C) photograph of the oral cavity. (D) Fused and registered final image of the RGB photo, OCT structures and OCTA blood flows.

4.4 Discussion and Conclusion

This study has described an adaptive contour tracking strategy for wide field OCT imaging of large samples with uneven surface contours and demonstrated its feasibility through verification in phantoms and *in vivo* experiments. In the phantom experiments, we quantified image contrast, signal-to-noise ratio, and penetration depth. Compared to traditional OCT imaging, the ACTS OCT imaging significantly improves imaging quality at deeper locations. In the *in vivo* demonstrations, we also observed visual improvement in both structural and blood flow signals with the ACTS strategy, especially for long ranging distance regions. ACTS prevents

deterioration of image quality with increasing imaging distance, maintaining high contrast and signal-to-noise ratio at both shallow and deep locations.

Another advantage of the ACTS strategy is the adaptive adjustment of the imaging window along the sample contour, which offers the potential to achieve an extended working range with a reduced system-ranging distance. Each incremental scan requires only half of the spectral sampling rate to meet the requirements. The system in this study adopts the k-clock triggering acquisition method. Without compromise of the performance in k-clock acquisition card, there is a competitive mechanism among sweep speed, bandwidth, and spectral sampling rate, which correspond to OCT parameters such as imaging speed, axial resolution, and imaging range. If the short-range mode is used, the burden on spectral sampling rate is relaxed. The released parameter space can then be utilized by the other two parameters. In other words, the system can choose a light source with a faster sweep speed or a wider bandwidth to improve imaging speed and axial resolution. Additionally, the reduction in spectral sampling rate means an increase in data transfer speed, saving storage space and computational power.

The adjustment of focus and reference optical delay line requires additional time, which is the primary cost of the ACTS strategy. The electro-controlled tunable ODL used in this system has a relative low response speed, approximately 6 mm/s. Each adjustment distance of 4.8 mm takes about 0.8 seconds. Due to the unstable start and stop processes of AODL, more time needs to be reserved, bringing the total time for each modulation to about 1.5 seconds. The additional imaging time required depends on the number of depth segments. The good news is that electro-controlled refractive index ODL modulation devices [160] or voice coil motor [161] systems are now available on the market with faster response speeds. If the system adopts these

components to adjust the optical path length of the system's reference arm, the additional imaging time consumption can be significantly reduced. Another alternative approach is to leverage the state-of-the-art integrated photonics circuit strategy [162,163], where multiple optical pathlength delay lines may be fabricated within a chip for rapid and programmable switching of the desired optical delay lines.

Another aspect of the ACTS strategy that can be improved is the pre-scan section. In this study, we used 20 B-scans along the slow axis as the pre-scan, taking approximately 0.1 seconds. Although it did not consume much imaging time, its limitation lies in the fact that the pre-scan needs to use the long-range mode to detect the surface contour across the entire field of view of the sample. As mentioned earlier, the actual imaging process for ACTS OCT only requires the short-range mode, and the released burden on spectral sampling rate can be used to improve imaging speed or axial resolution. However, if the pre-scan needs to use the long-range mode, the pressure on the spectral sampling rate of the system cannot be released, which affecting the further improvement of system performance. Additionally, even if the long-range mode is used, there is a limitation on the maximum contour variation that the system can accept for the sample (36 mm in this study). If the variation of the sample's contour along the slow axis is greater than 36 mm, the system cannot fully cover it. One improvement approach is to use other devices such as structured light illumination or stereo cameras strategy instead of OCT for slow-axis pre-scanning to detect the sample's contour. This solution can release the pressure on OCT's spectral sampling rate and is applicable to samples with larger surface variations. Of course, the detection algorithm for surface contours based on structured light illumination and stereo

cameras also needs to be upgraded as the hardware system improves. Algorithms based on deep learning may be a good choice.

The main limitation of the ACTS strategy lies in the difficulty of real-time adjustment of surface contour variations along the fast-scanning direction, especially in high-speed imaging modes. The system in this study employed a 600 kHz swept-source, completing a cross-sectional image comprising 1500 A-scans in just 2.5 ms. Therefore, current ETL and AODL technologies may not be capable of real-time adjustments along the fast axis. One feasible solution is to adopt an orthogonal scanning strategy, conducting separate adaptive scans along the fast axis (X-axis) and slow axis (Y-axis) directions. Subsequently, data fusion through post-processing could potentially achieve high-quality signals across the entire imaging field.

Currently, we consider the ACTS strategy to be most suitable for the wide field imaging in dentistry due to the significant physiological curves along the horizontal direction in the oral cavity, while the vertical direction remains relatively flat. The wide-field OCT's structural imaging provides clear visualization of the internal microstructure of hard tissues, accurately displaying the distribution and morphology of tissues such as enamel and dentin. This is helpful for diagnosing dental diseases and assessing the health status of tooth structures. Additionally, OCTA offers a detailed three-dimensional presentation of the soft tissue vascular network. In oral medicine, OCTA may be used to observe the distribution of gingival vessels, microcirculation, and to assess periodontal lesions. The fused image shown in Figure 4-10D provides comprehensive oral information for clinical professionals, aiding them in quickly and comprehensively appreciating oral health conditions.

Additionally, we believe the ACTS strategy is also applicable to ophthalmology. Although ETL has been widely used in ophthalmic OCT, AODL's adaptive adjustment ensures that the region of interest consistently falls into the imaging range with the highest sensitivity, which is beneficial for improved quality of ophthalmic OCT imaging. It would be also applicable for dermatology or plastic surgery, where a large field of view is often needed.

To conclude, we have shown that the proposed ACTS strategy significantly improves the wide FoV imaging quality of samples with an uneven surface contour. By employing a high-speed AODL and a pre-scanning scheme, this strategy requires minimal additional time consumption while alleviating spectral sampling rate pressure, thereby enhancing the overall performance of OCT.

5 HIGH-SPEED, WIDE-FIELD FIBER-BASED PS-OCT SYSTEM WITH REAL-TIME SURFACE STOKES FEEDBACK FOR CIRCULAR INPUT POLARIZATION

5.1 Background and Motivation

Optical Coherence Tomography (OCT) is a non-invasive, high-resolution imaging modality that enables cross-sectional visualization of biological tissues by detecting backscattered light through low-coherence interferometry [4,46,151]. It offers micrometer-scale spatial resolution and millimeter-scale penetration depth, making it an indispensable tool in ophthalmology [8,9,164], dermatology [14,18,165], dentistry [30,166,167], and numerous other clinical and research applications [26,168,169]. Its capability for real-time, label-free imaging has led to widespread clinical translation. As an extension of conventional OCT, Polarization-Sensitive OCT (PS-OCT) leverages polarization contrast to extract additional tissue-specific structural and compositional information [59,170]. PS-OCT enables three-dimensional imaging of birefringent structures, providing insight into the microstructural organization of anisotropic biological tissues such as tendon, muscle, mineralized tissue, retinal nerve fiber layers, and scar tissue [59,171]. These birefringence-based contrasts have proven valuable for diagnosing and monitoring various pathological conditions, including dental caries [127,172], intravascular abnormal [115,119], glaucoma [173,174], fibrosis [175], and pulmonary diseases [176].

Over the past decade, PS-OCT systems have evolved from free-space optical configurations to fiber-based implementations to enhance system compactness, robustness, and clinical applicability [177,178]. Fiber-based PS-OCT, particularly in handheld configurations, offers the potential for broader clinical deployment due to its flexibility and ease of integration [179,180]. However, several persistent challenges continue to hinder their broader adoption. A primary limitation is the uncontrolled variation in the state of polarization (SOP) within the sample arm, typically caused by fiber bending or scan alignment during imaging [57,181]. Such instability disrupts the intended circular input polarization, resulting in relative rather than absolute optic axis measurements and compromising the accuracy and reproducibility of birefringence mapping [182,183].

Fiber-based PS-OCT systems generally adopt either dual-input or single-input illumination schemes [184,185]. Dual-input designs, using sequential orthogonal probing or polarization multiplexing, offer a predefined orthogonal polarization state of probing light incident on the sample and can derive absolute birefringence measurements [184,186]. However, these configurations introduce greater system complexity and may reduce imaging speed, limiting their clinical practicality. In contrast, single-input systems are more compact, faster and easier to implement, but are more susceptible to SOP change, thereby restricting their output to relative polarization measurements [183].

To compensate for SOP variability in single-input systems, recent work has proposed using calibration structuressuch as ring-shaped birefringent targets placed at the probe's

distal end, for absolute SOP referencing [183]. While effective, these methods introduce several drawbacks, including reduced imaging depth and field of view, mandatory physical contact with the sample, and the need for complex post-processing to digitally calibrate the target and the tissue. These challenges are further exacerbated in wide-field imaging, where the sample surface is often highly curved or irregular [ref]. Additionally, the computational burden increases significantly with larger datasets inherent to wide-field scans [187].

Another critical factor that degrades the accuracy of fiber-based PS-OCT is polarization mode dispersion (PMD). PMD results from birefringence and asymmetric stress within the optical fiber, causing wavelength-dependent group delay differences between orthogonal polarization modes [188]. In systems employing broadband swept-source lasers, this leads to SOP distortion across the spectrum and compromises the fidelity of measured retardation and optic axis orientation [184]. A common mitigation strategy is spectral binning, which partitions the spectrum into narrower bands for separate processing [186]. Although this approach is relatively simple to implement and effective in suppressing PMD artifacts, it is computationally intensive and may reduce sensitivity. Other solutions involve hardware-based polarization compensation or advanced calibration routines, but these often increase system complexity and cost [117,189].

In this work, we present a high-speed, wide-field, fiber-based PS-OCT system that addresses these challenges through two key innovations. First, we introduce a real-time surface Stokes vector feedback mechanism to dynamically stabilize the circular input

polarization. By analyzing the Stokes vector of light backscattered from the tissue surface, our system actively compensates for SOP fluctuations in the sample arm, maintaining a stable and uniform circular polarization state without the need for reference targets or post-processing corrections. Second, to mitigate PMD, we employ a relatively narrow optical bandwidth swept-source laser, which reduces group delay dispersion between orthogonal polarization modes. This design choice balances axial resolution with reduced PMD sensitivity, simplifying data processing and improving measurement stability.

We validated our system using repeated phantom scans with intentional manual SOP perturbations, achieving an overall 6.52° variation in birefringence measurement, thereby demonstrating the effectiveness and robustness of our surface-based SOP feedback method. Furthermore, we performed *in vivo* imaging of the human oral cavity, obtaining depth-resolved birefringence maps of both teeth and gingiva. These results confirm the system's capability for robust and accurate polarization imaging over uneven and clinically relevant tissue surfaces. This approach not only simplifies the system architecture but also enhances polarization measurement reliability in complex geometries, enabling practical and scalable wide-field PS-OCT imaging for clinical applications.

5.2 Materials and Methods

5.2.1 System setup

To demonstrate the proposed dynamic circular input polarization strategy using surface Stokes vector feedback, we developed a high-speed, wide-field, all-single-mode fiber-based PS-OCT prototype system. The system employs a swept-source laser operating at 600 kHz with a central wavelength of 1310 nm and a spectral tuning range of 20 nm. The relatively narrow bandwidth was deliberately chosen for three main reasons: 1) To enable an extended imaging range of approximately 18 mm, which is critical for accommodating uneven surfaces in wide-field imaging within the constraints of available sampling rates; 2) To mitigate polarization mode dispersion (PMD) in the fiber-based system, thereby avoiding the need for post-acquisition spectral binning; 3)To maintain an acceptable axial resolution of approximately 37.8 μm in air (~28.4 μm in tissue), which is well matched to the lateral resolution and sufficient for wide-field structural and polarization imaging.

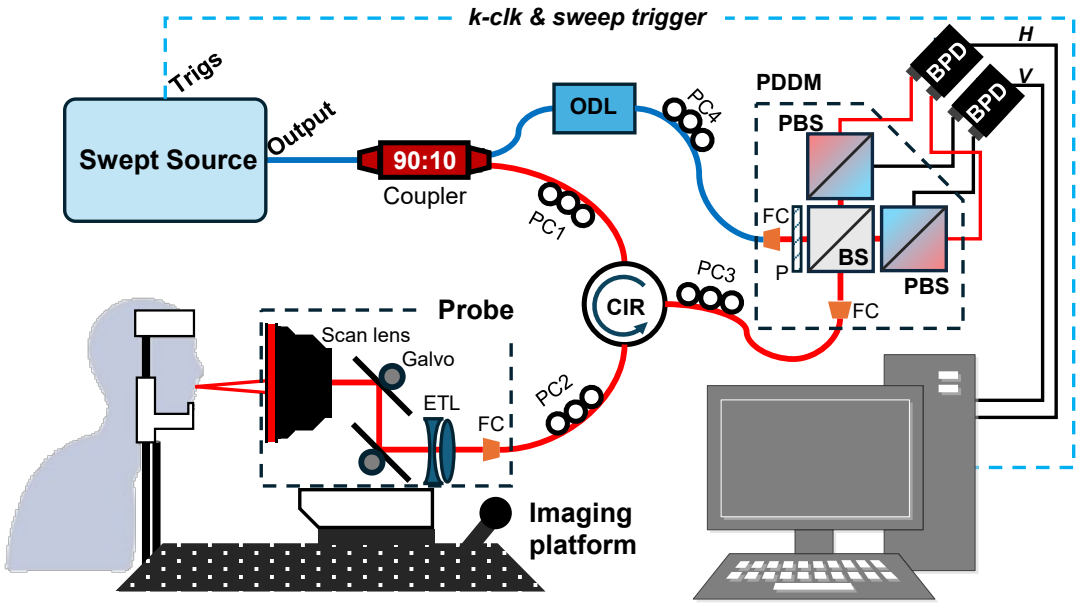

Figure 5-1 Schematic of the high-speed, wide-field, single-input fiber-based PS-OCT system. PC: polarization controller; CIR: circulator; FC: fiber collimator; ETL: electrically tunable lens; ODL: optical delay line; PDDM: polarization-diverse detection module; BS: beam splitter; PBS: polarization beam splitter; P: polarizer; BPD: balanced photodetector; H: horizontal polarization component; V: vertical polarization component.

The system is built on a Mach–Zehnder interferometer configuration (Figure 5-1). The laser output is split by a 90:10 fiber coupler (TW1300R2A2, Thorlabs, USA), sending 90% of the light to the sample arm and 10% to the reference arm. In the sample arm, a fiber-based circular polarizer (CIR-1310-50-APC, Thorlabs, USA) is used to circulate the input light and returned scattering with high efficiency. The light is then collimated by a fiber collimator (F260APC-C, Thorlabs, USA), yielding a beam with a diameter of approximately 2.8 mm. This beam is directed to a pair of galvanometric scanners (6210H, Cambridge Technology Inc., USA) via an electrically tunable lens (Optotune Ltd.), which enables dynamic focal adjustment to help locate and scan the target region. A scan lens with a 100 mm focal length focuses the beam onto the sample,

achieving a field of view (FOV) up to 40 × 40 mm² with a lateral resolution of ~57 μm in air (~42.9 μm in tissue).

In the reference arm, patch fibers and an electrical optical delay line (ODL) are used to match the optical path length with the sample arm. The backscattered light from the sample, returned via the circulator, and the delayed reference light are combined in a polarization-diverse detection module (PDDM). A 50:50 beam splitter (BS) directs the combined light to two polarization beam splitters (PBS), which separate the signals into orthogonal linear polarization components (horizontal and vertical). These components are converted to electrical signals using two balanced photodetectors (BPDs).

A dual-channel digitizer (ATS9360, AlazarTech Inc., Canada) with an integrated k-clock from laser is used for synchronized acquisition of the two polarization-resolved interferograms. To optimize interference efficiency and enable robust birefringence detection, four fiber-based polarization controllers (PCs) are strategically placed in both sample and reference arms to allow fine adjustment of the system's polarization states. Additional implementation details are provided in the subsequent sections. A customized LabVIEW-based software interface was developed for system synchronization, scan control, real-time imaging preview and data acquisition.

5.2.2 System calibration and surface stokes feedback

To ensure accurate birefringence detection and optimal interference efficiency, four polarization controllers (PCs) are strategically placed within the system to manage the

state of polarization (SOP) across both sample and reference arms. The calibration procedure is performed as follows:

1. Adjust PC1 to minimize the insertion loss in the circulator: PC1 is used to optimize light transmission through the fiber circulator. The paddles of PC1 are adjusted to vary the input SOP, while monitoring the optical power at port 2 of the circulator. The goal is to maximize the output power, thereby minimizing insertion loss due to SOP misalignment.

2. Adjust PC2 to generate a circular polarization at the sample interface: PC2 controls the SOP of light incident on the sample. Using a polarimeter (PAX1000IR2, Thorlabs), the output polarization from the sample arm is monitored. The paddles of PC2 are adjusted until a right-handed circular SOP is achieved, ensuring consistent polarization illumination for birefringence sensitivity.

3. Adjust PC3 to balance the polarization-diverse detection channels: To ensure accurate and efficient polarization-diverse detection, a mirror is placed at the sample plane to reflect the circularly polarized beam back into the detection path. PC3 is then adjusted to maximize the contrast between the two orthogonal interferograms. In this implementation, we maximized the vertical channel while minimizing the horizontal channel, thereby optimizing signal separation.

4. Adjust PC4 to maximize the interference efficiency in the reference arm: A linear polarizer oriented at 45° is inserted in the reference arm before

recombination with the sample signal. This ensures equal optical power in both orthogonal polarization channels. The paddles of PC4 are tuned to maximize the interference amplitude in both channels simultaneously, enabling symmetric and high-efficiency detection.

Once the polarization controllers are properly adjusted, the system is calibrated and ready for birefringence imaging. During practical imaging, most optical paths remain stable, except for the single-mode fiber (SMF) linking the main system to the handheld probe. This segment, referred to as the probing SMF in this work, is particularly susceptible to perturbation when the probe is moved or reoriented to locate the imaging target. Such perturbations alter the input SOP at the sample surface, degrading polarization sensitivity and leading to inconsistent birefringence measurements.

While polarimeters can be used to verify the SOP at the probe output during calibration, they are impractical for real-time monitoring during in-vivo imaging due to concerns over patient comfort and imaging efficiency. To address this, we propose a surface Stokes vector feedback strategy, which leverages the backscattered light from the sample surface to infer the SOP of the probing beam in real time. This feedback mechanism enables pre-scan adjustment to recover and stabilize the circular input SOP before data acquisition begins. The concept is modeled in Figure 5-2A. We assume that the reflected signal from the sample surface undergoes minimal sample-induced birefringence and preserves the SOP of the incident beam. As such, the light experiences a round-trip through the probing SMF, from circulator output to sample and back. The probing SMF can thus be modeled as an effective "virtual layer" on top of the sample.

As the light exiting the circulator and detected by the PDDM, the polarization transformation induced by the probing SMF can be visualized and characterized on the Poincaré sphere using the surface-reflected Stokes vector. By manually tuning PC2 before imaging and monitoring the corresponding changes in the surface Stokes vector, the SOP at the sample interface can be adjusted to restore circular polarization, thereby ensuring robust and consistent polarization-sensitive imaging.

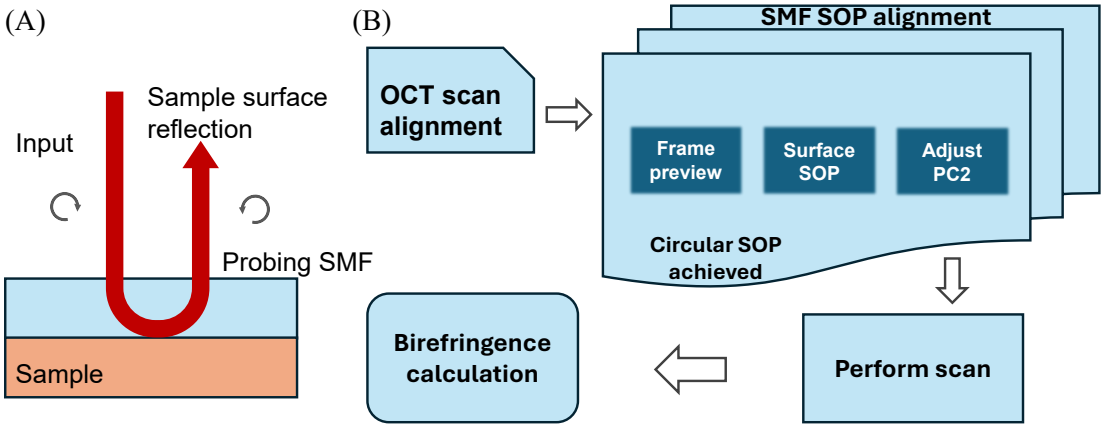

Figure 5-2 Sample arm modeling and imaging workflow. (A) Modeling sample arm state of polarization detection and (B) System workflow of PS-OCT data acquisition and birefringence imaging, integrating surface Stokes vector feedback for SOP stabilization.

The overall system workflow incorporating surface Stokes vector feedback is illustrated in Figure 5-2B. After initial system calibration, imaging begins by positioning the handheld probe to locate the region of interest (ROI), which is similar to the standard OCT imaging workflow. Prior to initiating a full 3D scan, SOP alignment of the probing SMF is performed to ensure circular polarization at the sample interface. This is particularly important after repositioning the probe, which may induce SOP variations due to fiber bending. A preview scan is first conducted to capture a cross-

sectional image of the sample. From this image, the sample surface is segmented, and the Stokes vector near the center of the field of view is extracted.

This surface Stokes vector is then plotted on the Poincaré sphere in real time. The paddles of PC2 are adjusted until the measured Stokes vector indicates a right-handed circular SOP, confirming that the probing beam at the sample interface has returned to the desired polarization state. Once this condition is satisfied, the wide-field 3D scan is

extract birefringence information, including local retardation and optic axis orientation. This surface-guided SOP correction mechanism ensures consistent polarization input and repeatable measurements across sessions, improving imaging reliability in real wide-field imaging scenarios.

5.2.3 PS-OCT imaging scanning protocol and data acquisition

To evaluate the feasibility and performance of the proposed system with surface Stokes vector feedback, both phantom and *in vivo* imaging experiments were conducted under standardized protocols.

Phantom Imaging: a 3D-printed ring-shaped phantom made from polylactic acid (PLA) was used to validate the system's ability to detect well-defined birefringence patterns. The phantom was designed with its optical fast axis oriented circumferentially, creating a known birefringence distribution suitable for polarization mapping. The outer diameter of the ring was 36 mm. A volumetric scan consisting of 1500 × 1500 A-lines was performed over the phantom, with a scan time of approximately 5 seconds using

raster scan with a duty cycle of 80%. The phantom study was conducted to assess the SOP stability and birefringence detection capabilities of the system under controlled conditions.

In vivo Imaging and Ethics Approval: to demonstrate the clinical applicability of the system, *in vivo* imaging was performed on healthy human volunteers, targeting the oral cavity region. The imaging probe was mounted onto a movable slit-lamp platform that offered three degrees of freedom, allowing fine positioning of the target area.

All *in vivo* procedures were conducted in compliance with the Declaration of Helsinki and the Health Insurance Portability and Accountability Act. The study received ethical approval from the Institutional Review Board (IRB) of the University of Washington. Written informed consent was obtained from all participants prior to imaging.

In vivo imaging protocol: powered by the high-speed 600 kHz swept-source laser, A scan protocol of 1500 × 1500 A-lines covering an area of ~40 × 40 mm^2, completed within ~5 seconds. During scanning, subjects were seated comfortably and asked to rest their head on a chin support to minimize motion. The movable slit-lamp platform was manipulated to align the imaging window with the anatomical region of interest. Once the region was within range, the surface Stokes vector feedback loop was initiated. A short preview scan was used to segment the sample surface and monitor the Stokes vector at the center of the field. Polarization Controller 2 was then adjusted to achieve right-handed circular SOP, as visualized on the Poincaré sphere, ensuring consistent and

high-fidelity birefringence measurements. Subjects were instructed to remain as still as possible throughout the scan. For oral cavity imaging, a mouth opener was used to maximize exposure of intraoral structures and facilitate wide-field OCT acquisition.

5.2.4 Data processing and birefringence calculation

To achieve real-time SOP monitoring and extract depth-resolved birefringence measurements, the acquired OCT signals were processed through several stages, including dispersion compensation, Fourier transformation, Stokes vector computation, and polarization state analysis.

For surface Stokes vector monitoring, the raw spectral interferograms from the two orthogonal detection channels were first apodized with a window function and corrected for dispersion mismatch. The resulting spectra were converted to complex depth-domain signals via inverse Fourier transform. The SOP of the backscattered signal from the sample surface was described using the Stokes parameters, calculated from the horizontal and vertical polarization channels as follows [190]:

$$S = \begin{pmatrix} S_0 \\ S_1 \\ S_2 \\ S_3 \end{pmatrix} = \begin{pmatrix} I \\ Q \\ U \\ V \end{pmatrix} = \begin{pmatrix} |E_x|^2 + |E_y|^2 \\ |E_x|^2 - |E_y|^2 \\ 2|E_x||E_y| \cdot cos\delta \\ 2|E_x||E_y| \cdot sin\delta \end{pmatrix} \quad (5\text{-}1)$$

Where Ex and Ey represent the complex amplitudes of the orthogonal polarization components, and δdenotes the phase delay between them. In our implementation, we assume S0=1for SOP visualization on the Poincaré sphere, since the normalized condition $S0^2=S1^2+S2^2+S3^2$ inherently holds. The sample surface was segmented based

on the intensity envelope (Stokes S0), and a 10-pixel wide region at the center of the field of view was extracted. The corresponding ten Stokes vectors were averaged and normalized to improve robustness against noise. This averaged vector was then visualized on the Poincaré sphere to monitor the SOP at the sample interface in real time. Figure 5-3A and B show the OCT structural images of the 3D-printed phantom from horizontal and vertical channels, respectively. Figure 5-3C displays the RGB-coded Stokes vector image, where Q, U, and V are mapped to red, green, and blue channels, respectively. Figure 5-3D shows the extracted SOPs from the surface region plotted on the Poincaré sphere, blue dots represent individual pixel vectors, while the bold red dot shows the averaged SOP. With a workstation equipped with an AMD Ryzen 7 5800X CPU and 64 GB RAM, our custom software achieved real-time SOP monitoring at up to 24 frames per second, enabling efficient and responsive adjustment of the probing SMF polarization state

To retrieve depth-resolved polarization parameters, the two orthogonal spectral signals were processed to generate complex A-lines following windowing and dispersion correction. Stokes vectors were calculated for each pixel throughout the depth profile. Using the structural OCT signal (S0), the tissue surface was segmented, and all subsequent Stokes vectors were flattened with respect to the surface to ensure accurate depth referencing for polarization analysis. To reduce speckle noise, a 4×4 pixel spatial averaging filter was applied to the cross-sectional Q, U, and V components of the Stokes vectors. Birefringence parameters, including local optic axis and phase retardation, were then computed using a discrete differential geometry (DDG)-based

polarization state tracking algorithm [191], which traces the evolution of polarization states along depth to extract high-fidelity birefringence metrics.

5.3 Results

5.3.1 Real-time input SOP monitoring and local axis detection

To demonstrate the capability of our system to monitor and control the input state of polarization (SOP) in real time, we first evaluated how the surface-reflected Stokes vectors from the sample can be used to track and adjust the SOP of the probing beam.

Stokes vectors extracted from the surface of a ring-shaped PLA birefringence phantom were plotted on the Poincaré sphere during a stepwise manual adjustment of PC2, which controls the probing SMF. The goal was to tune an arbitrary SOP to a right-handed circular SOP. As shown in Figure 5-3E, four consecutive adjustments were performed, and the resulting trajectory of the SOP on the Poincaré sphere is displayed. The blue, red, yellow, and purple dots denote intermediate SOPs during each adjustment step, and gray arrows indicate the convergence trend toward circular polarization.

As the SOP of the probing beam varied, corresponding changes were observed in the RGB color-coded Stokes vector maps, as shown in Figure 5-3F–H. These reflect the evolution of the Q, U, and V components of the surface Stokes vectors, confirming the system's ability to detect and respond to input polarization changes. This result validates the effectiveness of our surface Stokes vector feedback strategy as a real-time tool for stabilizing the circular input SOP prior to scanning.

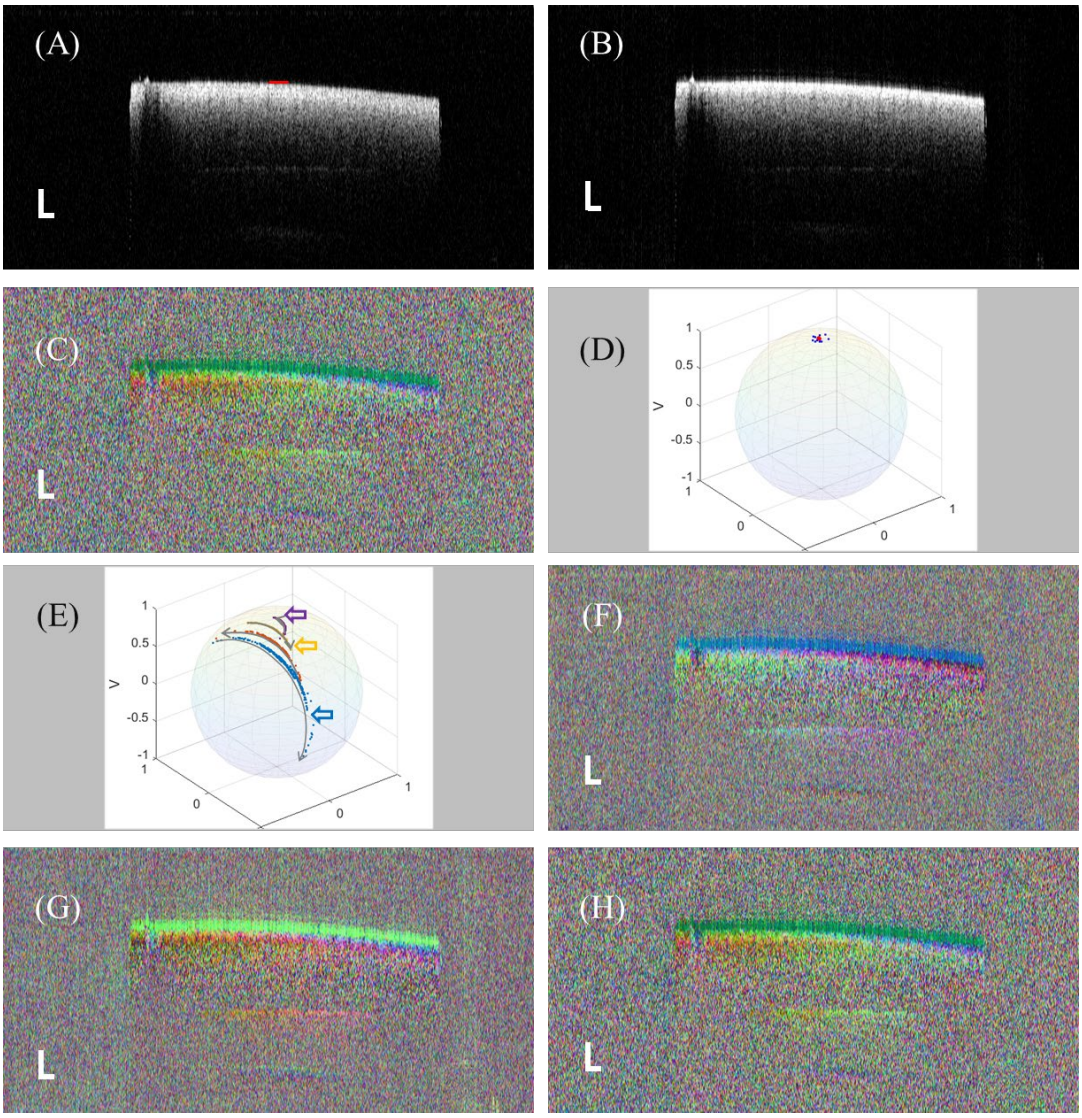

Figure 5-3 Stokes vector extraction and real-time monitoring of the sample arm SOP. (A) OCT image of the 3D-printed phantom from the horizontal channel. (B) Corresponding vertical channel image. (C) RGB-coded Stokes image using Q, U, and V as red, green, and blue channels, respectively. (D) Poincaré sphere visualization of Stokes vectors from 10 surface pixels (blue dots), with the averaged SOP shown as a bold red dot. (E) Real-time SOP trajectory during manual adjustment of the probing SMF polarization state. Different colored dots represent SOP states at different timepoints, and gray arrows indicate the convergence trend toward circular polarization. (F–H) Stokes vector displays corresponding to different SOP states marked by blue, yellow, and purple arrows in (E). All scale bars denote 1 mm.

To evaluate the impact of input SOP on birefringence accuracy, we imaged the phantom under two conditions: (1) with a circular input SOP achieved through surface-based feedback control, and (2) with an elliptical SOP representing a typical uncorrected polarization state. As shown in Figure 5-4A, the phantom consists of a 3D-printed PLA ring with its fast axis oriented circumferentially, generating a known birefringence distribution. The OCT structural en face projection is displayed in Figure 5-4B. The input SOPs used for the two scans are plotted on the Poincaré sphere in Figure 5-4C, with the circular SOP marked in purple and the elliptical SOP marked in blue. The resulting local axis orientation maps are shown in Figure 5-4D (circular SOP) and Figure 5-4E (elliptical SOP). The circular input produced a smooth, symmetrical distribution of axis orientations consistent with the phantom geometry, while the elliptical input introduced distortions and biased orientations, particularly visible as reddish regions indicating angular drift.

To quantitatively assess detection accuracy, we extracted local axis orientations along a 90-degree arc on the phantom circumference (0°–90° in Cartesian coordinates), denoted by the white dashed arc in Figure 5-4F. The extracted axis orientations are plotted in Figure 5-4F, where the purple and blue dashed lines represent measurements under circular and elliptical SOPs, respectively. Linear fits (solid lines) reveal the angular trends. Under circular input SOP, the detected orientation ranges from approximately –5° to 90°, closely matching the actual arc geometry. In contrast, the elliptical input SOP yields a distorted orientation range of –45° to 30°, with an initial bias far from zero and a total detection span (~75°) notably smaller than the expected

90° arc. These findings confirm that non-circular input SOPs lead to significant orientation bias and inaccurate estimation of the true angular span. In contrast, the real-time surface Stokes vector feedback enables the circular input illumination, thereby ensuring accurate and robust birefringence detection.

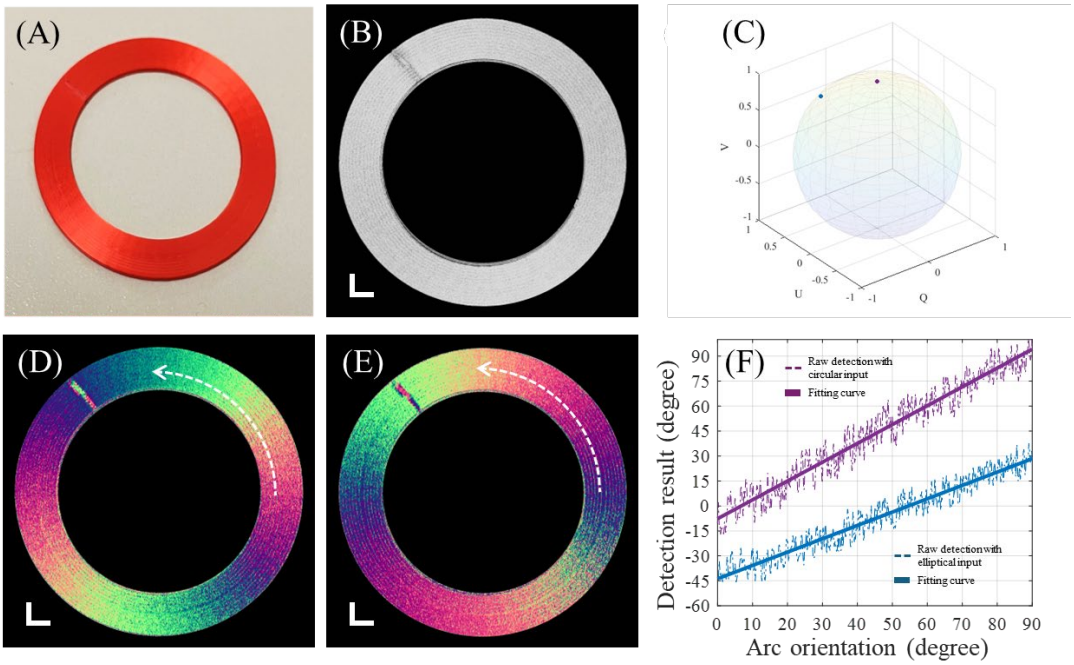

Figure 5-4 Depth-resolved local axis detection under varying input SOPs. (A) Photograph of the 3D-printed PLA birefringence phantom. (B) En face structural OCT projection of the phantom. (C) Poincaré sphere showing the two input SOPs: circular (purple dot) and elliptical (blue dot). (D–E) Depth-resolved local axis orientation maps acquired under circular (D) and elliptical (E) input SOPs. (F) Extracted local axis orientation along a 90° arc (indicated by the white dashed curve) in (D) and (E), with dashed lines showing measured angles and solid lines indicating linear fits. All scale bars denote 3 mm.

5.3.2 Evaluation of SOP monitoring repeatability

To evaluate the repeatability and robustness of our real-time SOP monitoring and correction strategy based on surface Stokes vector feedback, we conducted a series of

controlled phantom imaging experiments. A ring-shaped birefringent phantom was imaged in three independent sessions. Prior to each session, the probing SMF was intentionally perturbed to simulate practical handling-induced SOP variation. After perturbation, the input SOP was adjusted using surface Stokes vector feedback to restore a circular SOP before beginning each scan.

Figure 5-5A–C show the resulting local axis orientation maps from the three independent measurements. Each image displays a consistent central-symmetric pattern along the phantom's circumference, with a gradual change in orientation which is consistent with the phantom's geometry. Visually, the local axis distributions across all three trials are highly consistent, demonstrating the repeatability of the SOP stabilization process.

To quantitatively assess performance, we extracted the local axis orientations along a 90-degree arc (from 0° to 90° in Cartesian coordinates), indicated by the white dashed arc in each map. The extracted orientation values from the three trials were averaged, and the mean and standard deviation were calculated for each position along the arc. The results are plotted in Figure 5-5D, where the solid purple line indicates the mean local axis orientation, and the light purple ribbon represents ±1 standard deviation. The orientation values start near 0° and increase gradually to ~90°, matching the known birefringent profile of the phantom. The narrow spread across the repeated measurements reflects excellent measurement consistency. To further validate reproducibility, we computed the intra-class correlation coefficient (ICC) for the repeated orientation measurements, yielding a value of 0.935, which indicates excellent

repeatability of the SOP correction and local axis detection. These findings confirm that our surface Stokes vector feedback strategy provides stable and reproducible input SOP correction, enabling consistent and accurate polarization-sensitive imaging in fiber-based PS-OCT systems.

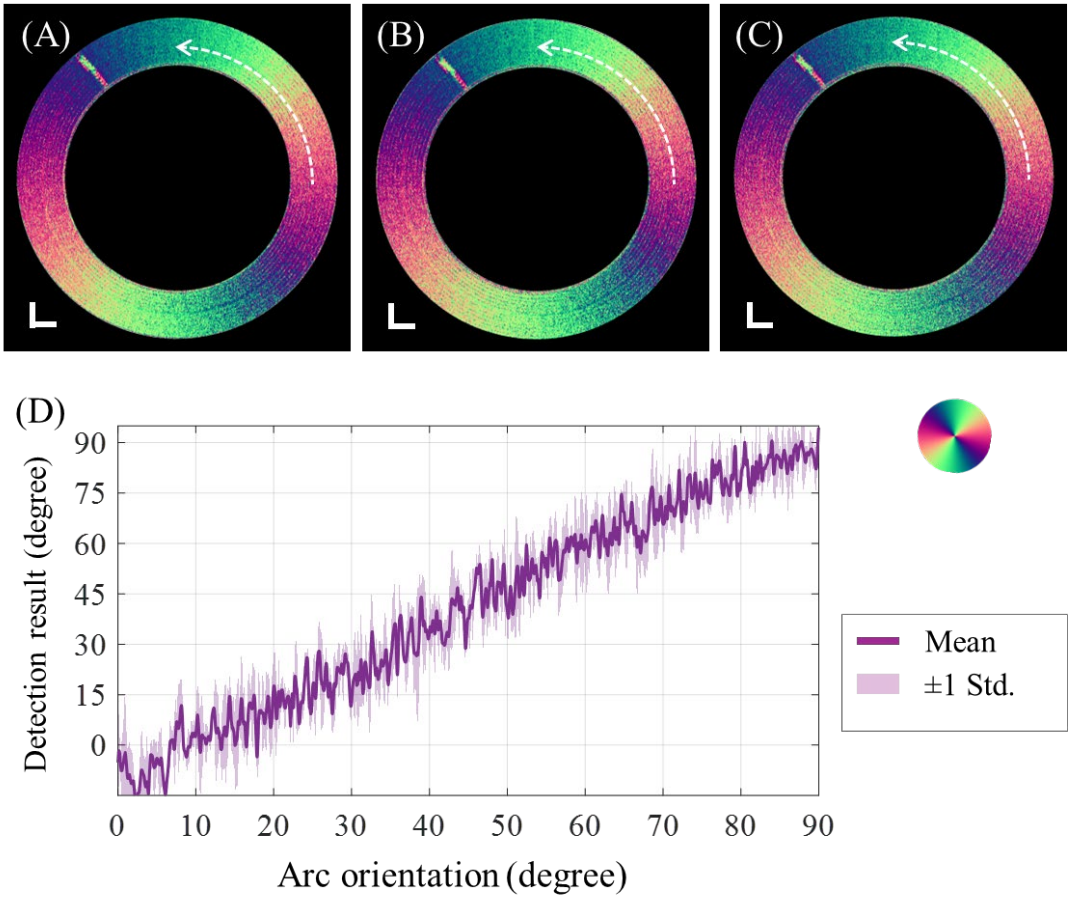

Figure 5-5 Phantom local axis detection across repeated measurements. (A–C) Local axis orientation maps from three independent imaging sessions using surface Stokes feedback after deliberate SOP perturbation. (D) Statistical results of local axis orientation along a 90° arc (white dashed curve in A–C). The solid purple line shows the average detection, and the light purple band represents ±1 standard deviation across the three trials. All scale bars denote 3 mm.

5.3.3 Wide-field *in vivo* PS-OCT imaging of the human oral cavity

In vivo imaging of the human oral cavity was conducted using the proposed wide-field fiber-based PS-OCT system, enabled by real-time SOP stabilization via surface Stokes vector feedback. Figure 5-6A presents a 3D-rendered volume of the anterior oral cavity, acquired in a single wide-field scan covering 40 × 40 mm². The image reveals detailed structural features, including 13 teeth and surrounding soft tissues. The white and gray arrows indicate the growth directions of the four central incisors and adjacent side teeth, respectively. To assess tissue birefringence, Figure 5-6B shows an en face degree of polarization uniformity map computed at 100 μm below the tissue surface. DOPU reflects the stability of the detected polarization state and is modulated by tissue scattering and structural organization. A 5 × 5 window filter was applied to the Stokes vector for the DOPU computation, and the overall average DOPU across the oral cavity was 0.63, indicating a mix of ordered and disordered birefringent regions.

Figure 5-6C displays the en face optic axis orientation map at 100 μm below the tissue surface. The local axis map highlights variations in collagen fiber organization in soft tissue and hydroxyapatite crystal alignment in enamel. Both teeth and gingiva exhibit strong birefringence signals, but distinct orientation patterns are observed. The central incisors show more uniform and vertically aligned orientations, indicated by light green and yellow hues, consistent with their symmetrical growth patterns. In contrast, side teeth show more angular and heterogeneous orientation distributions, reflecting their oblique orientation and more complex anatomical structure. Furthermore,

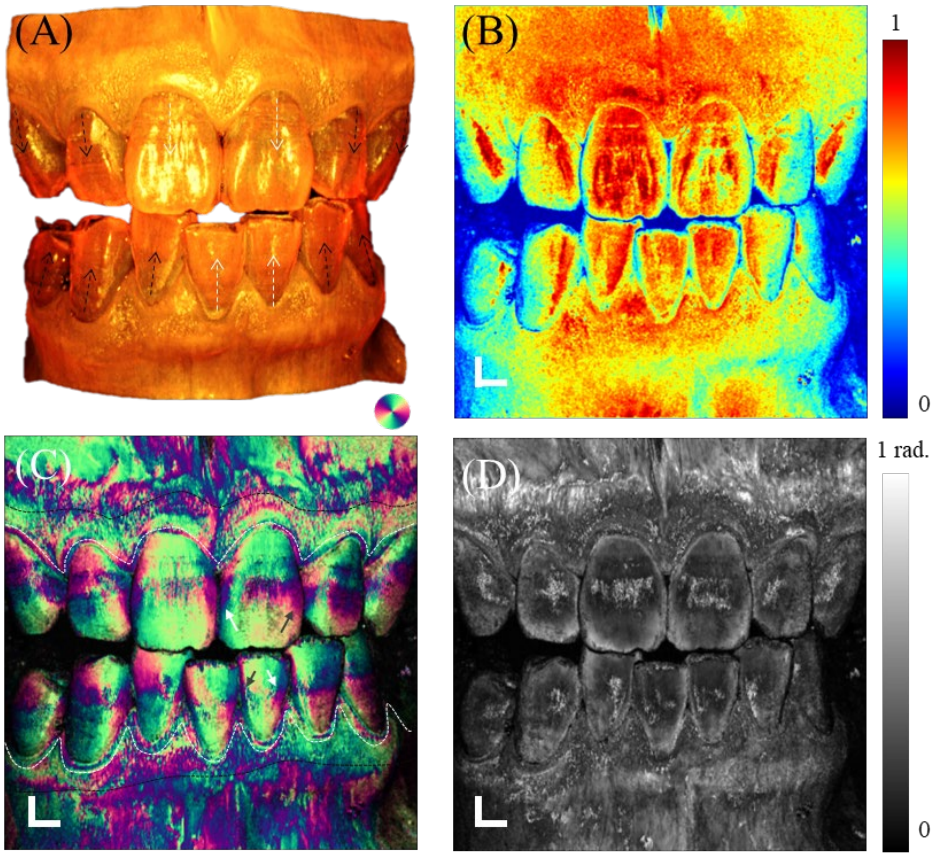

Figure 5-6 *In vivo* PS-OCT imaging reveals wide-field oral cavity anatomy and birefringence contrasts. (A) 3D rendering of anterior oral cavity volume. White arrows indicate incisor growth direction; gray arrows indicate side teeth growth angles. (B) En face DOPU map at 100 μm depth, computed with 5 × 5 Stokes vector filtering. (C) Reconstructed 3D optic axis orientation map at 100 μm depth. White and gray arrows point to edge variations in axis orientation. White dashed lines denote free gingiva and attached gingiva boundary, and black dashed lines denote the attached gingiva and mucosa boundary. (D) Phase retardation map at 100 μm depth. All scale bars denote 3 mm.

at the edges of central incisors, asymmetric optical axis distributions are observed: the upper teeth show dark green and magenta on the left and light magenta and yellow on the right, while the bottom teeth exhibit the reversed pattern. This suggests localized differences in hydroxyapatite crystal orientation, particularly at the dental edge region. Figure 5-6D shows the corresponding phase retardation map, where the enamel edges

exhibit higher phase delays than the central regions, consistent with increased enamel thickness near the dental edge [192], indicating the potential of PS-OCT as a tool for evaluating enamel morphology and integrity.

In addition to capturing wide-field structure and polarization contrasts, the system also enables localized assessment of dental health. Figure 5-7A displays an averaged en face structural projection of the oral cavity. A zoom-in view of the central incisors is shown in Figure 5-7B–D, corresponding to the red box in Figure 5-7A. The local optic axis orientation map (Figure 5-7B) includes vector overlays on a 130 μm grid, allowing better visualization of enamel fiber direction at macro scale. The white arrows point to the upper margin of the bottom central incisor, where disrupted orientation patterns are observed, suggesting possible early-stage enamel lesions. These regions also exhibit reduced retardation in the corresponding phase map (Figure 5-7C) and correlate with subtle morphological abnormalities in the structural projection (Figure 5-7D).

Beyond hard tissues, the wide-field birefringence imaging also provides valuable information about oral soft tissue organization. As shown in Figure 5-6B–D, both gingiva and mucosa exhibit strong birefringence signatures. The gingival region shows a higher average DOPU (~0.74) compared to adjacent alveolar mucosa, indicating a more stable and ordered fiber structure. In the optic axis map, the attached gingiva displays more scattered orientation patterns, compared with mucosa. Phase retardation in the gingiva is more uniform than in the mucosa, which reflects differences in collagen density, vascularity, and mechanical properties. To further investigate gingival birefringence, Figure 5-7E–G provide a close-up view of the central upper gingiva,

corresponding to the green box in Figure 5-7A. A narrow color band within the free gingiva is observed in the optic axis map (Figure 5-7E), indicating relatively uniform collagen orientation. The phase retardation map (Figure 5-7F) further shows a more uniform distribution in free gingiva region, indicating homogeneously distributed birefringence in this region. Structurally, the OCT projection (Figure 5-7G) and corresponding clinical photograph (Figure 5-7H) reveal that the free gingiva appears smoother and more connective, while the attached gingiva exhibits a stippled, pillar-like architecture with distinct microstructural cavities, features likely contributing to the observed birefringence heterogeneity.

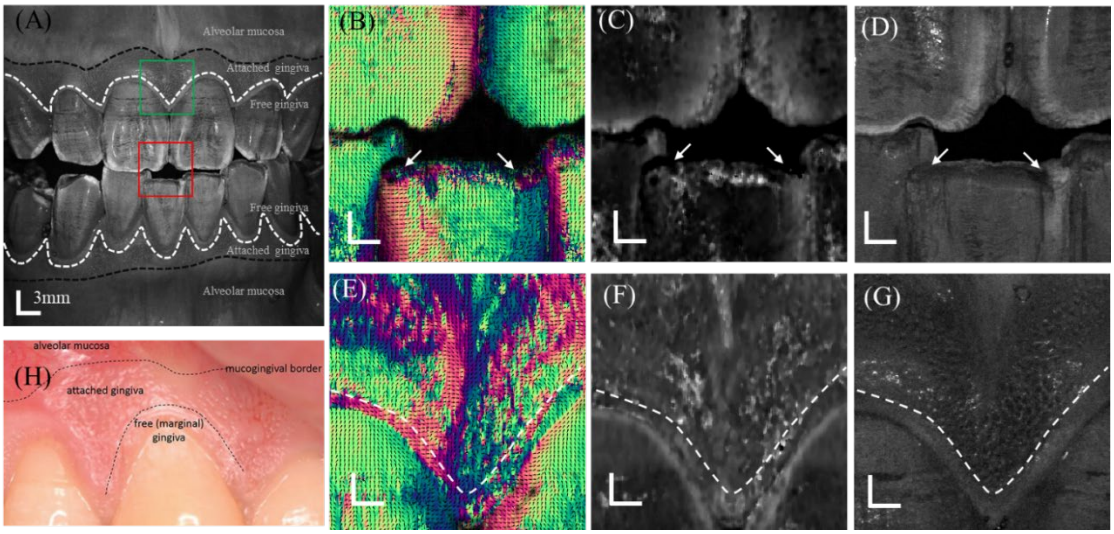

Figure 5-7 Localized PS-OCT mapping of enamel integrity and gingival birefringence. (A) En face structure of the entire oral cavity from average projection. (B–D) Zoom-in views of the central incisors: local axis orientation (B), phase retardation (C), and structural (D) from the red box in (A). White arrows mark potential enamel lesion regions. (E–G) Zoom-in views of central upper gingiva: axis orientation (E), retardation (F), and structure (G) from the green box in (A). Dashed curve marks the boundary between free and attached gingiva. (H) Clinical photograph of typical human gingiva showing morphology differences. Small black arrows in (B) and (E) denote fiber orientation trends over 130 μm scale. All scale bars in (B–G) are denoting 1 mm.

5.4 Discussion and Conclusion

In this study, we developed and demonstrated a high-speed, wide-field, single-input fiber-based PS-OCT system for *in vivo* imaging of the human oral cavity. The system incorporates a real-time surface Stokes vector feedback mechanism to dynamically stabilize the input polarization state at the sample interface, addressing a long-standing challenge in single-fiber PS-OCT design. By integrating this feedback strategy with a high-speed 600 kHz swept source and optimized system architecture, we achieved robust birefringence measurements over a 40 × 40 mm² field of view, enabling detailed structural and polarization-resolved imaging of both teeth and gingival tissues.

Single-input PS-OCT architectures offer distinct advantages over dual-input systems, particularly in terms of system simplicity, compactness, and scanning speed. However, they are also more susceptible to input SOP drift [183], especially in handheld or wide-field configurations. Prior solutions have relied on reference targets or digital post-correction, which complicate probe design or require additional processing [181,183]. Our proposed method utilizes the sample surface-reflected Stokes vectors as a reliable real-time feedback to guide SOP alignment before each scan. This eliminates the need for external polarimetry hardware, simplifies the user workflow, and enables fast, repeatable polarization control. Phantom experiments demonstrated a median angular standard deviation of 6.52° in repeated local axis orientation measurements, providing enough precision and repeatability across multiple sessions in real clinical settings.

This strategy is enabled by the physical principle that the surface reflection, particularly from shallow tissue depths (<100 μm), undergoes minimal birefringence-induced SOP transformation, and therefore preserves the probing beam's incident polarization state [179,184]. In weakly birefringent or isotropic tissues, this reflection offers a near-direct measurement of the input SOP. Even in birefringent tissues such as enamel or gingiva, the shallow surface backscatter arises from a thin optical path with limited retardation and depolarization. As a result, the Stokes vector measured at the surface can be used as a proxy for the input SOP, enabling accurate alignment to a circular polarization state prior to deeper volumetric imaging. This rationale supports the generalizability of the surface Stokes feedback mechanism across a wide range of tissue types and anatomical sites.

A key challenge in fiber-based PS-OCT is polarization mode dispersion (PMD), which distorts the measured polarization states and introduces depth-dependent phase errors. PMD arises from birefringence in fibers and optical components, including fiber couplers and circulators, and is especially problematic in systems using broadband light sources. To mitigate this, we adopted a relatively narrowband (20 nm) high-speed swept source, which balances axial resolution (~37.8 μm in air) with PMD suppression. Although this resolution is lower than ultra-broadband sources, it is still significantly higher than conventional clinical imaging modalities such as X-ray and ultrasound imaging [30,137]. Importantly, the system achieved a polarization extinction ratio exceeding 200, surpassing conventional PS-OCT implementations [178]. While circulators introduce PMD due to the round-trip passage of backscattered light, our

architecture and calibration approach help to contain its effects within acceptable limits without requiring additional polarization compensation stages.

Wide-field imaging brings additional challenges to PS-OCT performance. As the scanning angle increases, the effective SOP of the probing beam can vary across the field due to fiber birefringence and non-normal incidence at the sample surface. This variation can degrade the uniformity of polarization sensitivity, particularly at peripheral regions of the scan. In our design, real-time feedback-based SOP correction was performed before each scan, which mitigates but does not fully eliminate such spatially varying artifacts. Potential future improvements may include field-dependent compensation, or localized SOP tracking during scan acquisition to further enhance wide-field fidelity.

Our i*n vivo* results demonstrate the potential of this system for comprehensive assessment of oral health, offering co-registered structural and functional contrast. The optic axis orientation and phase retardation maps captured fine variations in enamel crystal alignment, detected localized enamel damage, and visualized birefringent properties of gingival tissue, including distinctions between free and attached gingiva. These findings align with previous reports of the diagnostic value of PS-OCT in oral applications and suggest its utility in detecting early-stage enamel lesions, periodontal conditions, and soft tissue morphology changes with micrometer-scale precision [12,111].

In conclusion, we developed a robust and clinically adaptable wide-field PS-OCT system that incorporates real-time input SOP stabilization using surface Stokes vector feedback. The system enables repeatable and accurate birefringence imaging across large fields of view, while minimizing polarization mode dispersion through a balanced optical bandwidth design. By integrating hardware simplification, real-time SOP monitoring, and high-speed volumetric acquisition, the system supports practical, handheld-compatible *in vivo* imaging. This approach not only streamlines system complexity but also improves the reliability of polarization-sensitive measurements in anatomically complex and dynamic environments, advancing the clinical translation of wide-field PS-OCT for dental and soft tissue diagnostics.

6 SUMMARY

6.1 Work Summary

This study presents a comprehensive set of innovations in swept-source optical coherence tomography aimed at addressing four critical challenges that currently limit the clinical utility of OCT systems: restricted imaging depth, nonlinear phase distortion distortion in high speed and long raneg acquisition, imaging inconsistency over contoured surfaces, and polarization instability in fibered based PSOCT. By tackling these interrelated limitations through system-level solutions, the work advances OCT technology toward a more versatile, high-performance imaging platform capable of structural, angiographic, and birefringence-based functional imaging in real time.

In Chapter 2, we introduced a multi-channel delay sampling method to overcome the depth limitations inherent in high-speed SS-OCT systems. By splitting the analog interference signal into two time-delayed channels and calibrating their phase relationship in k-space, we effectively doubled the axial imaging depth from 18 mm to 36 mm without altering the k-clock trigger or reducing system speed. This technique provides a scalable solution for extending imaging range in swept-source systems constrained by digitizer bandwidth or k-clock resolution.

In Chapter 3, we addressed the issue of nonlinear phase distortion and spatial warping that occur in high-speed, wide-field OCT imaging due to the finite analog bandwidth and dispersion in electronic components. We introduced the concept of electrical

dispersion, characterized its effects, and proposed a global k-space compensation strategy. In addition, we developed a vector field-based distortion correction algorithm to restore geometric accuracy in large-area scans. These innovations improve both spectral linearity and spatial fidelity, as demonstrated in volumetric imaging of the anterior oral cavity.

Chapter 4 focused on improving imaging quality across uneven or highly contoured surfaces, such as dental arches or facial skin. In these regions, fixed optical focus and depth of field often result in degraded signal-to-noise ratio and image sharpness at the periphery of the scan. To address this, we implemented an adaptive contour tracking and scanning method, which integrates a real-time surface profiling algorithm with an electrically tunable lens and an adjustable optical delay line. This strategy dynamically maintains focus and optimal imaging conditions throughout the entire scan, thereby enhancing both structural and OCTA image consistency.

In Chapter 5, we extended the imaging capabilities of the system to include polarization-sensitive OCT using a single-input fiber-based configuration. A key challenge in this setup is maintaining a stable incident state of polarization, especially during wide-field or handheld imaging. To solve this, we developed a real-time surface Stokes vector feedback mechanism, which continuously monitors the back-reflected polarization state and actively compensates for SOP fluctuations. This innovation enables stable circular polarization delivery, facilitating robust birefringence imaging across complex sample geometries and extended scan areas.

Collectively, the methods developed in this thesis enable an OCT system that operates at 600 kHz A-line rate, delivers a ~ 42 × 42 mm² lateral field of view, achieves 36 mm axial imaging depth, and supports multi-modal imaging including structural OCT, angiography, and birefringence mapping. Each component of the system has been validated through ex vivo and *in vivo* imaging studies, with a focus on oral cavity applications. The combination of hardware advances, optical calibration, and algorithmic correction contributes to a robust and flexible high speed functinal OCT framework suitable for clinical translation.

6.2 Future Perspectives

While this thesis establishes a high-speed, long-range, wide-field, and functionally capable OCT system, several technical and translational aspects remain to be explored to further enhance its performance, robustness, and clinical applicability. To meet the demands of real-time clinical use, further acceleration of data processing and visualization is critical. One promising direction is the implementation of GPU-based real-time volume reconstruction. Leveraging parallel computing can significantly reduce the computational bottleneck associated with large 3D OCT/OCTF datasets, particularly under high-speed acquisition protocols [193].

Another important direction is the integration of 3D stereo vision and robotic arm systems with the OCT scanning apparatus[194,195]. In the current adaptive scanning strategy, the imaging range is constrained by the OCT pre-scan capabilities and the mechanical limits of the manual scanning interface. By incorporating a 3D structured-

light or stereo vision system, it becomes possible to obtain global surface contour information over a much larger field. This data can then be used to guide a robotic arm equipped with the OCT probe, enabling intelligent path planning and optimized probe positioning relative to complex or irregular anatomical structures. Such a system would significantly extend the effective working distance and imaging coverage of the OCT system, allowing adaptive scanning to be performed over full facial surfaces, intraoral regions, or other anatomically challenging areas with improved precision and repeatability.

In addition, the current system architecture trades off spatial resolution for imaging range and field of view. To mitigate this compromise, deep learning-based super-resolution techniques could be introduced. These approaches can reconstruct fine structural details from undersampled or resolution-limited OCT volumes, potentially recovering detail lost during high-speed scanning or under large field configurations [196,197].

To facilitate the clinical translation of the proposed OCT system, expanded *in vivo* studies are essential to evaluate the system's performance across a range of clinically relevant use cases. Applications such as periodontitis assessment, where changes in gingival thickness, vascularity, and connective tissue birefringence are critical diagnostic markers, represent ideal targets for high-resolution, functional OCT. Similarly, anterior segment imaging of the eye can benefit from the system's speed and non-contact design, enabling detailed visualization of the cornea, iris, and iridocorneal angle for glaucoma screening or pre-surgical evaluation.

To enable broader clinical adoption, future work should also explore the integration of ultracompact optical and electronic components, including MEMS scanners, miniaturized optics, and fiber-coupled detection. These developments would support the creation of portable or handheld OCT probes, which are particularly suited for intraoral, dermatological, and point-of-care imaging scenarios. Handheld operation would also be facilitated by the system's real-time processing capabilities and SOP stabilization features.

Moreover, combining the OCT system with machine vision and robotic arm technologies offers a pathway to fully automated or semi-automated scanning, particularly in intraoperative or image-guided surgical environments. The integration of robotic arms with real-time stereo or structured-light vision systems can enable intelligent probe placement, adaptive trajectory control, and repeatable, operator-independent scans over large or complex anatomical surfaces. Such a combination would be especially useful in guided interventions involving the oral cavity, craniofacial regions, or orthopedic procedures.

Lastly, the system's high A-line rate opens new opportunities for visualizing dynamic biological processes. One compelling application is the volumetric imaging of the trabecular meshwork in the anterior eye, a critical structure involved in aqueous humor drainage. By capturing volumetric datasets at high speed, it becomes feasible to monitor the biomechanical motion of the trabecular meshwork in response to

physiological pressure fluctuations or pharmacological interventions, offering new insights into glaucoma pathogenesis and treatment efficacy.

REFERENCES

1. J. Boer, R. Leitgeb, and M. Wojtkowski, "Twenty-five years of optical coherence tomography: the paradigm shift in sensitivity and speed provided by Fourier domain OCT," Biomed. Opt. Express **8**(7), 3248–3280 (2017).

2. M. Adhi and J. S. Duker, "Optical coherence tomography–current and future applications," Current opinion in ophthalmology **24**(3), 213 (2013).

3. A. F. Fercher, W. Drexler, C. K. Hitzenberger, and T. Lasser, "Optical coherence tomography-principles and applications," Reports on progress in physics **66**(2), 239 (2003).

4. P. H. Tomlins and R. K. Wang, "Theory, developments and applications of optical coherence tomography," J. Phys. D: Appl. Phys. **38**(15), 2519–2535 (2005).

5. S. Aumann, S. Donner, J. Fischer, and F. Müller, "Optical coherence tomography (OCT): principle and technical realization," High resolution imaging in microscopy and ophthalmology: new frontiers in biomedical optics 59–85 (2019).

6. A. H. Kashani, C.-L. Chen, J. K. Gahm, F. Zheng, G. M. Richter, P. J. Rosenfeld, Y. Shi, and R. K. Wang, "Optical coherence tomography angiography: a comprehensive review of current methods and clinical applications," Progress in retinal and eye research **60**, 66–100 (2017).

7. J. Campbell, M. Zhang, T. Hwang, S. Bailey, D. Wilson, Y. Jia, and D. Huang, "Detailed vascular anatomy of the human retina by projection-resolved optical coherence tomography angiography," Scientific reports **7**(1), 1–11 (2017).

8. S. Song, K. Zhou, J. J. Xu, Q. Zhang, S. Lyu, and R. Wang, "Development of a clinical prototype of a miniature hand-held optical coherence tomography probe for prematurity and pediatric ophthalmic imaging," Biomed. Opt. Express **10**(5), 2383 (2019).

9. T. Adejumo, T.-H. Kim, D. Le, T. Son, G. Ma, and X. Yao, "Depth-resolved vascular profile features for artery-vein classification in OCT and OCT angiography of human retina," Biomedical Optics Express **13**(2), 1121–1130 (2022).

10. T. T. Hormel and Y. Jia, "OCT angiography and its retinal biomarkers," Biomedical Optics Express **14**(9), 4542–4566 (2023).

11. N. Le, J. Lu, P. Tang, K.-H. Chung, H. Subhash, L. Kilpatrick-Liverman, and R. K. Wang, "Intraoral optical coherence tomography and angiography combined with autofluorescence for dental assessment," Biomed. Opt. Express **13**(6), 3629 (2022).

12. N. M. Le, S. Song, H. Zhou, J. Xu, Y. Li, C.-E. Sung, A. Sadr, K.-H. Chung, H. M. Subhash, L. Kilpatrick, and R. K. Wang, "A noninvasive imaging and measurement using optical coherence tomography angiography for the assessment of gingiva: An *in vivo* study," J. Biophotonics **11**(12), e201800242 (2018).

13. A. M. Lee, L. Cahill, K. Liu, C. MacAulay, C. Poh, and P. Lane, "Wide-field *in vivo* oral OCT imaging," Biomedical optics express **6**(7), 2664–2674 (2015).

14. Y. Shi, J. Lu, N. Le, and R. K. Wang, "Integrating a pressure sensor with an OCT handheld probe to facilitate imaging of microvascular information in skin tissue beds," Biomedical Optics Express **13**(11), 6153–6166 (2022).

15. L. An, J. Qin, and R. K. Wang, "Ultrahigh sensitive optical microangiography for *in vivo* imaging of microcirculations within human skin tissue beds," Optics express **18**(8), 8220–8228 (2010).

16. P. Gong, L. Chin, S. Es' haghian, Y. M. Liew, F. M. Wood, D. D. Sampson, and R. A. McLaughlin, "Imaging of skin birefringence for human scar assessment using polarization-sensitive optical coherence tomography aided by vascular masking," Journal of biomedical optics **19**(12), 126014–126014 (2014).

17. J. Lu, A. J. Deegan, Y. Cheng, S. P. Mandell, and R. K. Wang, "OCT-Based Angiography and Surface Topography in Burn-Damaged Skin," Lasers in Surgery and Medicine **53**(6), 849–860 (2021).

18. E. C. Sattler, R. Kästle, and J. Welzel, "Optical coherence tomography in dermatology," Journal of biomedical optics **18**(6), 061224 (2013).

19. M. J. Gora, M. J. Suter, G. J. Tearney, and X. Li, "Endoscopic optical coherence tomography: technologies and clinical applications," Biomedical optics express **8**(5), 2405–2444 (2017).

20. W. Kang, H. Wang, Z. Wang, M. W. Jenkins, G. A. Isenberg, A. Chak, and A. M. Rollins, "Motion artifacts associated with *in vivo* endoscopic OCT images of the esophagus," Optics express **19**(21), 20722–20735 (2011).

21. T. S. Kirtane, M. S. Wagh, and others, "Endoscopic optical coherence tomography (OCT): advances in gastrointestinal imaging," Gastroenterology research and practice **2014**, (2014).

22. J. Zhang, T. Nguyen, B. Potsaid, V. Jayaraman, C. Burgner, S. Chen, J. Li, K. Liang, A. Cable, G. Traverso, and others, "Multi-MHz MEMS-VCSEL swept-source optical coherence tomography for endoscopic structural and angiographic imaging with miniaturized brushless motor probes," Biomedical Optics Express **12**(4), 2384–2403 (2021).

23. M. Terashima, H. Kaneda, and T. Suzuki, "The role of optical coherence tomography in coronary intervention," The Korean journal of internal medicine **27**(1), 1 (2012).

24. B. Baumann, A. Woehrer, G. Ricken, M. Augustin, C. Mitter, M. Pircher, G. G. Kovacs, and C. K. Hitzenberger, "Visualization of neuritic plaques in Alzheimer's disease by polarization-sensitive optical coherence microscopy," Scientific Reports **7**(1), 43477 (2017).

25. B. Dubois, H. H. Feldman, C. Jacova, H. Hampel, J. L. Molinuevo, K. Blennow, S. T. DeKosky, S. Gauthier, D. Selkoe, R. Bateman, and others, "Advancing

research diagnostic criteria for Alzheimer's disease: the IWG-2 criteria," The Lancet Neurology **13**(6), 614–629 (2014).

26. M. Ibne Mokbul, "Optical coherence tomography: basic concepts and applications in neuroscience research," Journal of medical engineering **2017**, (2017).

27. Y. Jia and R. K. Wang, "Label-free *in vivo* optical imaging of functional microcirculations within meninges and cortex in mice," Journal of neuroscience methods **194**(1), 108–115 (2010).

28. L. Brumaire, Y. He, I. Tsui, and I. D. Pluym, "Pregnancy associated hypertension screening with optical coherence tomography angiography," American Journal of Obstetrics & Gynecology **228**(1), S685 (2023).

29. C. Pole and others, "Utility of optical coherence tomography angiography in pregnancy-associated central serous chorioretinopathy," American Journal of Ophthalmology Case Reports **20**, 100979 (2020).

30. S. Ali, S. B. S. Gilani, J. Shabbir, K. S. Almulhim, A. Bugshan, and I. Farooq, "Optical coherence tomography's current clinical medical and dental applications: a review," F1000Research **10**, (2021).

31. S. Song, J. Xu, and R. K. Wang, "Long-range and wide field of view optical coherence tomography for *in vivo* 3D imaging of large volume object based on akinetic programmable swept source," Biomed. Opt. Express **7**(11), 4734 (2016).

32. F. Soecknick, K. Breher, Z. Nafar, S. Kubach, J. Straub, S. Wahl, and F. Ziemssen, "The clinical evaluation of a widefield lens to expand the field of view in optical coherence tomography (OCT-A)," Sci Rep **14**(1), 6936 (2024).

33. T. Klein and R. Huber, "High-speed OCT light sources and systems," Biomedical optics express **8**(2), 828–859 (2017).

34. S. Ni, X. Wei, R. Ng, S. Ostmo, M. F. Chiang, D. Huang, Y. Jia, J. P. Campbell, and Y. Jian, "High-speed and widefield handheld swept-source OCT angiography with a VCSEL light source," Biomedical optics express **12**(6), 3553–3570 (2021).

35. E. P. Grijalva, A. M. Jiménez, A. Bradu, A. Fernandez, B. Meyer, A. Jensen, E. Semenova, T. Ansbæk, K. Yvind, and A. Podoleanu, "Novel 1.6 MHz swept source for real-time volumetric in-vivo OCT imaging of the human retina," in *Optical Coherence Tomography and Coherence Domain Optical Methods in Biomedicine XXVII* (SPIE, 2023), **12367**, pp. 8–12.

36. J. P. Kolb, T. Klein, C. L. Kufner, W. Wieser, A. S. Neubauer, and R. Huber, "Ultra-widefield retinal MHz-OCT imaging with up to 100 degrees viewing angle," Biomedical Optics Express **6**(5), 1534–1552 (2015).

37. J. Xu, W. Wei, S. Song, X. Qi, and R. K. Wang, "Scalable wide-field optical coherence tomography-based angiography for *in vivo* imaging applications," Biomed. Opt. Express **7**(5), 1905 (2016).

38. V. F. Ferrario, C. Sforza, C. E. Poggio, G. Serrao, and A. Colombo, "Three-dimensional dental arch curvature in human adolescents and adults," American journal of orthodontics and dentofacial orthopedics **115**(4), 401–405 (1999).

39. F. D. Uzuner, B. I. Aslan, and M. Dinçer, "Dentoskeletal morphology in adults with Class I, Class II Division 1, or Class II Division 2 malocclusion with increased overbite," American Journal of Orthodontics and Dentofacial Orthopedics **156**(2), 248–256 (2019).

40. S. Wisetchat, K. A. Stevens, and S. R. Frost, "Facial modeling and measurement based upon homologous topographical features," Plos one **19**(5), e0304561 (2024).

41. B. Bengtsson, S. Andersson, and A. Heijl, "Performance of time-domain and spectral-domain Optical Coherence Tomography for glaucoma screening," Acta Ophthalmol **90**(4), 310–315 (2012).

42. J. Zhang, V. Mazlin, K. Fei, A. C. Boccara, J. Yuan, and P. Xiao, "Time-domain full-field optical coherence tomography (TD-FF-OCT) in ophthalmic imaging," Therapeutic Advances in Chronic Disease **14**, 204062232311701 (2023).

43. A. J. Bard, F.-R. F. Fan, D. T. Pierce, P. R. Unwin, D. O. Wipf, and F. Zhou, "Chemical imaging of surfaces with the scanning electrochemical microscope," Science **254**(5028), 68–74 (1991).

44. A. F. Fercher, W. Drexler, C. K. Hitzenberger, and T. Lasser, "Optical coherence tomography-principles and applications," Reports on progress in physics **66**(2), 239 (2003).

45. M. H. Freeman, *Optics* (Butterworth-Heinemann, 1990).

46. D. P. Popescu, L.-P. Choo-Smith, C. Flueraru, Y. Mao, S. Chang, J. Disano, S. Sherif, and M. G. Sowa, "Optical coherence tomography: fundamental principles, instrumental designs and biomedical applications," Biophysical reviews **3**, 155–169 (2011).

47. C.-L. Chen and R. K. Wang, "Optical coherence tomography based angiography," Biomedical optics express **8**(2), 1056–1082 (2017).

48. B. E. Bouma, S.-H. Yun, B. J. Vakoc, M. J. Suter, and G. J. Tearney, "Fourier-domain optical coherence tomography: recent advances toward clinical utility," Current opinion in biotechnology **20**(1), 111–118 (2009).

49. Z. Yaqoob, J. Wu, and C. Yang, "Spectral Domain Optical Coherence Tomography: a Better OCT Imaging Strategy," BioTechniques **39**(sup6), 2 (2005).

50. Z. Michalewska, J. Michalewski, and J. Nawrocki, "Swept-source OCT," Retina Today 50–56 (2013).

51. J. F. De Boer, B. Cense, B. H. Park, M. C. Pierce, G. J. Tearney, and B. E. Bouma, "Improved signal-to-noise ratio in spectral-domain compared with time-domain optical coherence tomography," Optics letters **28**(21), 2067–2069 (2003).

52. M. Sehi, D. S. Grewal, C. W. Sheets, and D. S. Greenfield, "Diagnostic ability of Fourier-domain vs time-domain optical coherence tomography for glaucoma detection," American journal of ophthalmology **148**(4), 597–605 (2009).

53. M. Hagen-Eggert, P. Koch, and G. Hüttmann, "Analysis of the signal fall-off in spectral domain optical coherence tomography systems," in *Optical Coherence Tomography and Coherence Domain Optical Methods in Biomedicine XVI* (SPIE, 2012), **8213**, pp. 161–167.

54. "Understanding MEMS-VCSEL Bandwidth Definitions.pdf," (n.d.).

55. S. Moon and E. S. Choi, "VCSEL-based swept source for low-cost optical coherence tomography," Biomedical optics express **8**(2), 1110–1121 (2017).

56. J. Le Gouët, D. Venkatraman, F. N. Wong, and J. H. Shapiro, "Experimental realization of phase-conjugate optical coherence tomography," Optics letters **35**(7), 1001–1003 (2010).

57. X. Liu, M. Ke, X. Yao, J. Chua, L. Schmetterer, and B. Tan, "Stable complex conjugate artifact removal in OCT using circularly polarized light as reference," Optics Letters **45**(14), 3977–3980 (2020).

58. W. Choi, B. Potsaid, V. Jayaraman, B. Baumann, I. Grulkowski, J. J. Liu, C. D. Lu, A. E. Cable, D. Huang, and J. S. Duker, "Phase-sensitive swept source OCT imaging of the human retina with a VCSEL light source," Optics letters **38**(3), 338 (2013).

59. J. F. De Boer, C. K. Hitzenberger, and Y. Yasuno, "Polarization sensitive optical coherence tomography–a review," Biomedical optics express **8**(3), 1838–1873 (2017).

60. S. Song, J. Xu, S. Men, T. T. Shen, and R. K. Wang, "Robust numerical phase stabilization for long-range swept-source optical coherence tomography," Journal of biophotonics **10**(11), 1398–1410 (2017).

61. T. Klein and R. Huber, "High-speed OCT light sources and systems," Biomedical optics express **8**(2), 828–859 (2017).

62. B. Potsaid, I. Gorczynska, V. J. Srinivasan, Y. Chen, J. Jiang, A. Cable, and J. G. Fujimoto, "Ultrahigh speed spectral/Fourier domain OCT ophthalmic imaging at 70,000 to 312,500 axial scans per second," Optics express **16**(19), 15149–15169 (2008).

63. L. An, P. Li, T. T. Shen, and R. Wang, "High speed spectral domain optical coherence tomography for retinal imaging at 500,000 A-lines per second," Biomedical optics express **2**(10), 2770–2783 (2011).

64. K. Wang, G. Huang, Z. Ding, and L. Wang, "High-speed spectral-domain optical coherence tomography at 830nm wavelength," in *Optics in Health Care and Biomedical Optics III* (SPIE, 2008), **6826**, pp. 77–85.

65. S. H. Yun, G. J. Tearney, B. E. Bouma, B. H. Park, and J. F. de Boer, "High-speed spectral-domain optical coherence tomography at 1.3 μm wavelength," Optics express **11**(26), 3598–3604 (2003).

66. B. Lee, S. Chen, E. M. Moult, Y. Yu, A. Y. Alibhai, N. Mehta, C. R. Baumal, N. K. Waheed, and J. G. Fujimoto, "High-speed, ultrahigh-resolution spectral-domain OCT with extended imaging range using reference arm length matching," Translational vision science & technology **9**(7), 12–12 (2020).

67. D. J. Fechtig, B. Grajciar, T. Schmoll, C. Blatter, R. M. Werkmeister, W. Drexler, and R. A. Leitgeb, "Line-field parallel swept source MHz OCT for structural and functional retinal imaging," Biomedical optics express **6**(3), 716–735 (2015).

68. V. P. Pandiyan, X. Jiang, A. Maloney-Bertelli, J. A. Kuchenbecker, U. Sharma, and R. Sabesan, "High-speed adaptive optics line-scan OCT for cellular-resolution optoretinography," Biomedical Optics Express **11**(9), 5274–5296 (2020).

69. X. Jiang, T. Liu, V. P. Pandiyan, E. Slezak, and R. Sabesan, "Coarse-scale optoretinography (CoORG) with extended field-of-view for normative characterization," Biomedical Optics Express **13**(11), 5989–6002 (2022).

70. R. Huber, "Fourier domain mode locking (FDML): A new laser operating regime and applications for biomedical imaging, profilometry, ranging and sensing," in *Advanced Solid-State Photonics* (Optica Publishing Group, 2009), p. MA1.

71. W. Wieser, B. R. Biedermann, T. Klein, C. M. Eigenwillig, and R. Huber, "Multi-megahertz OCT: High quality 3D imaging at 20 million A-scans and 4.5 GVoxels per second," Optics express **18**(14), 14685–14704 (2010).

72. T. Klein, W. Wieser, C. M. Eigenwillig, B. R. Biedermann, and R. Huber, "Megahertz OCT for ultrawide-field retinal imaging with a 1050nm Fourier domain mode-locked laser," Optics express **19**(4), 3044–3062 (2011).

73. Y. Takubo, T. Shirahata, and S. Yamashita, "Optimization of a dispersion-tuned wavelength-swept fiber laser for optical coherence tomography," Applied optics **55**(27), 7749–7755 (2016).

74. S. Tozburun, M. Siddiqui, and B. J. Vakoc, "A rapid, dispersion-based wavelength-stepped and wavelength-swept laser for optical coherence tomography," Optics express **22**(3), 3414–3424 (2014).

75. T. S. Kim, J. Joo, I. Shin, P. Shin, W. J. Kang, B. J. Vakoc, and W.-Y. Oh, "9.4 MHz A-line rate optical coherence tomography at 1300 nm using a wavelength-swept laser based on stretched-pulse active mode-locking," Scientific reports **10**(1), 9328 (2020).

76. V. Jayaraman, G. D. Cole, M. Robertson, A. Uddin, and A. Cable, "High-sweep-rate 1310 nm MEMS-VCSEL with 150 nm continuous tuning range," Electron. Lett. **48**(14), 867 (2012).

77. R. Huber, M. Wojtkowski, and J. G. Fujimoto, "Fourier Domain Mode Locking (FDML): A new laser operating regime and applications for optical coherence tomography," Optics express **14**(8), 3225–3237 (2006).

78. C. Jirauschek and R. Huber, "Wavelength shifting of intra-cavity photons: Adiabatic wavelength tuning in rapidly wavelength-swept lasers," Biomedical Optics Express **6**(7), 2448–2465 (2015).

79. S. Chen, B. Potsaid, Y. Li, J. Lin, Y. Hwang, E. M. Moult, J. Zhang, D. Huang, and J. G. Fujimoto, "High speed, long range, deep penetration swept source OCT for structural and angiographic imaging of the anterior eye," Scientific reports **12**(1), 992 (2022).

80. E. A. Proano Grijalva, A. Martinez Jimenez, A. Bradu, A. Fernandez Uceda, B. Ole Meye, A. Jensen, E. Semenova, T. Ansbaek, K. Yvind, and A. Podoleanu, "Novel 1.6 MHz swept source for realtime volumetric in-vivo OCT imaging of the human retina," (2023).

81. G. Liu, J. Yang, J. Wang, Y. Li, P. Zang, Y. Jia, and D. Huang, "Extended axial imaging range, widefield swept source optical coherence tomography angiography," Journal of biophotonics **10**(11), 1464–1472 (2017).

82. S. Song, J. Xu, and R. K. Wang, "Flexible wide-field optical micro-angiography based on Fourier-domain multiplexed dual-beam swept source optical coherence tomography," Journal of Biophotonics **11**(3), e201700203 (2018).

83. K. Mori, J. Kanno, and P. L. Gehlbach, "Retinochoroidal morphology described by wide-field montage imaging of spectral domain optical coherence tomography," Retina **36**(2), 375–384 (2016).

84. R. J. Zawadzki, S. S. Choi, A. R. Fuller, J. W. Evans, B. Hamann, and J. S. Werner, "Cellular resolution volumetric *in vivo* retinal imaging with adaptive optics–optical coherence tomography," Optics express **17**(5), 4084–4094 (2009).

85. Y. Li, G. Gregori, B. L. Lam, and P. J. Rosenfeld, "Automatic montage of SD-OCT data sets," Optics express **19**(27), 26239–26248 (2011).

86. M. Gawęcki and K. Kiciński, "Advantages of the Utilization of Wide-Field OCT and Wide-Field OCT Angiography in Clinical Practice," Diagnostics **14**(3), 321 (2024).

87. Z. Wang, B. Potsaid, L. Chen, C. Doerr, H.-C. Lee, T. Nielson, V. Jayaraman, A. E. Cable, E. Swanson, and J. G. Fujimoto, "Cubic meter volume optical coherence tomography," Optica **3**(12), 1496–1503 (2016).

88. J. G. Fujimoto, W. Drexler, J. S. Schuman, and C. K. Hitzenberger, "Optical Coherence Tomography (OCT) in ophthalmology: introduction.," Optics express **17**(5), 3978–3979 (2009).

89. M. L. Gabriele, G. Wollstein, H. Ishikawa, L. Kagemann, J. Xu, L. S. Folio, and J. S. Schuman, "Optical coherence tomography: history, current status, and laboratory work," Investigative ophthalmology & visual science **52**(5), 2425–2436 (2011).

90. S. K. Nadkarni, M. C. Pierce, B. H. Park, J. F. de Boer, P. Whittaker, B. E. Bouma, J. E. Bressner, E. Halpern, S. L. Houser, and G. J. Tearney, "Measurement of collagen and smooth muscle cell content in atherosclerotic plaques using polarization-sensitive optical coherence tomography," Journal of the American College of Cardiology **49**(13), 1474–1481 (2007).

91. B. E. Bouma, M. Villiger, K. Otsuka, and W.-Y. Oh, "Intravascular optical coherence tomography," Biomedical optics express **8**(5), 2660–2686 (2017).

92. Y.-Q. Xiong, Y. Mo, Y.-Q. Wen, M.-J. Cheng, S.-T. Huo, X.-J. Chen, and Q. Chen, "Optical coherence tomography for the diagnosis of malignant skin tumors: a meta-analysis," Journal of biomedical optics **23**(2), 020902–020902 (2018).

93. H. D. Lee, G. H. Kim, J. G. Shin, B. Lee, C.-S. Kim, and T. J. Eom, "Akinetic swept-source optical coherence tomography based on a pulse-modulated active mode locking fiber laser for human retinal imaging," Scientific reports **8**(1), 17660 (2018).

94. A. T. Zavareh and S. Hoyos, "Kalman-based real-time functional decomposition for the spectral calibration in swept source optical coherence tomography," IEEE Transactions on Biomedical Circuits and Systems **14**(2), 257–273 (2019).

95. M. Cao, F. Xu, H. Jia, L. Zhou, E. Ji, and J. Wu, "A Multiple Interpolation Algorithm to Improve Resampling Accuracy in Data Triggers," Electronics **12**(6), 1291 (2023).

96. J. Xi, L. Huo, J. Li, and X. Li, "Generic real-time uniform K-space sampling method for high-speed swept-Source optical coherence tomography," Optics express **18**(9), 9511–9517 (2010).

97. K. Liang, Z. Wang, O. O. Ahsen, H.-C. Lee, B. M. Potsaid, V. Jayaraman, A. Cable, H. Mashimo, X. Li, and J. G. Fujimoto, "Cycloid scanning for wide field optical coherence tomography endomicroscopy and angiography *in vivo*," Optica **5**(1), 36–43 (2018).

98. H.-C. Lee, O. O. Ahsen, K. Liang, Z. Wang, C. Cleveland, L. Booth, B. Potsaid, V. Jayaraman, A. E. Cable, H. Mashimo, and others, "Circumferential optical coherence tomography angiography imaging of the swine esophagus using a micromotor balloon catheter," Biomedical optics express **7**(8), 2927–2942 (2016).

99. A. López-Marín, G. Springeling, R. Beurskens, H. van Beusekom, A. F. van der Steen, A. D. Koch, B. E. Bouma, R. Huber, G. van Soest, and T. Wang, "Motorized

capsule for shadow-free OCT imaging and synchronous beam control," Optics Letters **44**(15), 3641–3644 (2019).

100. Z. Gong, Y. Shi, and R. K. Wang, "De-aliased depth-range-extended optical coherence tomography based on dual under-sampling," Optics Letters **47**(11), 2642–2645 (2022).

101. A. Zhang, Q. Zhang, C.-L. Chen, and R. K. Wang, "Methods and algorithms for optical coherence tomography-based angiography: a review and comparison," Journal of biomedical optics **20**(10), 100901–100901 (2015).

102. C. C. Mota, L. O. Fernandes, R. Cimoes, and A. S. Gomes, "Non-invasive periodontal probing through Fourier-domain optical coherence tomography," Journal of periodontology **86**(9), 1087–1094 (2015).

103. M. Machoy, J. Seeliger, L. Szyszka-Sommerfeld, R. Koprowski, T. Gedrange, and K. Woźniak, "The use of optical coherence tomography in dental diagnostics: a state-of-the-art review," Journal of healthcare engineering **2017**(1), 7560645 (2017).

104. M. Siddiqui, A. S. Nam, S. Tozburun, N. Lippok, C. Blatter, and B. J. Vakoc, "High-speed optical coherence tomography by circular interferometric ranging," Nature photonics **12**(2), 111–116 (2018).

105. J. Ong, A. Zarnegar, G. Corradetti, S. R. Singh, and J. Chhablani, "Advances in optical coherence tomography imaging technology and techniques for choroidal and retinal disorders," Journal of Clinical Medicine **11**(17), 5139 (2022).

106. J. Chhablani and S. R. Singh, *Optical Coherence Tomography Imaging: Advances in Ophthalmology* (MDPI-Multidisciplinary Digital Publishing Institute, 2023).

107. J. D. Li, C. Viehland, A.-H. Dhalla, R. Trout, W. Raynor, A. N. Kuo, C. A. Toth, L. M. Vajzovic, and J. A. Izatt, "Visualization of surgical maneuvers using intraoperative real-time volumetric optical coherence tomography," Biomedical Optics Express **14**(7), 3798–3811 (2023).

108. M. Klufts, A. M. Jiménez, S. Lotz, M. A. Bashir, T. Pfeiffer, A. Mlynek, W. Wieser, A. Chamorovskiy, A. Bradu, A. Podoleanu, and others, "828 kHz retinal imaging with an 840 nm Fourier domain mode locked laser," Biomedical Optics Express **14**(12), 6493–6508 (2023).

109. P. J. Rosenfeld, Y. Cheng, M. Shen, G. Gregori, and R. K. Wang, "Unleashing the power of optical attenuation coefficients to facilitate segmentation strategies in OCT imaging of age-related macular degeneration: perspective," Biomedical optics express **14**(9), 4947–4963 (2023).

110. T. Murata, T. Hirano, H. Mizobe, and S. Toba, "OCT-angiography based artificial intelligence-inferred fluorescein angiography for leakage detection in retina," Biomedical Optics Express **14**(11), 5851–5860 (2023).

111. Y. Shimada, A. Sadr, Y. Sumi, and J. Tagami, "Application of Optical Coherence Tomography (OCT) for Diagnosis of Caries, Cracks, and Defects of Restorations," Curr Oral Health Rep **2**(2), 73–80 (2015).

112. Y.-S. Hsieh, Y.-C. Ho, S.-Y. Lee, C.-C. Chuang, J. Tsai, K.-F. Lin, and C.-W. Sun, "Dental optical coherence tomography," Sensors **13**(7), 8928–8949 (2013).

113. J. Welzel, "Optical coherence tomography in dermatology: a review," Skin Research and Technology: Review article **7**(1), 1–9 (2001).

114. J. Lu, A. J. Deegan, Y. Cheng, S. P. Mandell, and R. K. Wang, "OCT-Based Angiography and Surface Topography in Burn-Damaged Skin," Lasers in Surgery and Medicine **53**(6), 849–860 (2021).

115. J. Bec, X. Zhou, M. Villiger, J. A. Southard, B. Bouma, and L. Marcu, "Dual modality intravascular catheter system combining pulse-sampling fluorescence lifetime imaging and polarization-sensitive optical coherence tomography," Biomedical Optics Express **15**(4), 2114–2132 (2024).

116. M. Gao, D. Guo, J. Wang, Y. Tan, K. Liu, L. Gao, Y. Zhang, Z. Ding, Y. Gu, and P. Li, "High-accuracy noninvasive continuous glucose monitoring using OCT angiography-purified blood scattering signals in human skin," Biomedical Optics Express **15**(2), 991–1003 (2024).

117. D. C. Adams, A. Majid, and M. J. Suter, "Polarization mode dispersion correction in endoscopic polarization-sensitive optical coherence tomography with incoherent polarization input states," Biomedical Optics Express **13**(6), 3446–3460 (2022).

118. T. Wang, T. Pfeiffer, A. Akyildiz, H. M. van Beusekom, R. Huber, A. F. van der Steen, and G. Van Soest, "Intravascular optical coherence elastography," Biomedical Optics Express **13**(10), 5418–5433 (2022).

119. G. L. Jones, Q. Xiong, X. Liu, B. E. Bouma, and M. Villiger, "Single-input polarization-sensitive optical coherence tomography through a catheter," Biomedical Optics Express **14**(9), 4609–4626 (2023).

120. Y. Liu, H. Zhang, and X. Li, "Technologies for depth scanning in miniature optical imaging systems," Biomedical Optics Express **14**(12), 6542–6562 (2023).

121. H. Luo, S. Li, S. Kou, Y. Lin, I. S. Hagemann, and Q. Zhu, "Enhanced 3D visualization of human fallopian tube morphology using a miniature optical coherence tomography catheter," Biomedical Optics Express **14**(7), 3225–3233 (2023).

122. X. Guo, X. Li, X. Wang, M. Li, X. Dai, L. Kong, Q. Hao, J. Zhao, Y. Huang, and L. Sun, "Wearable optical coherence tomography angiography probe for freely moving mice," Biomedical Optics Express **14**(12), 6509–6520 (2023).

123. S. Burhan, N. Detrez, K. Rewerts, P. Strenge, S. Buschschlüter, J. Kren, C. Hagel, M. M. Bonsanto, R. Brinkmann, and R. Huber, "Phase unwrapping for MHz optical coherence elastography and application to brain tumor tissue," Biomedical Optics Express **15**(2), 1038–1058 (2024).

124. S. P. Hsu, M.-H. Lin, C.-F. Lin, T.-Y. Hsiao, Y.-M. Wang, and C.-W. Sun, "Brain tumor grading diagnosis using transfer learning based on optical coherence tomography," Biomedical Optics Express **15**(4), 2343–2357 (2024).

125. A. E. Heidari, S. P. Sunny, B. L. James, T. M. Lam, A. V. Tran, J. Yu, R. D. Ramanjinappa, K. Uma, P. Birur, and A. Suresh, "Optical coherence tomography as an oral cancer screening adjunct in a low resource settings," IEEE Journal of Selected Topics in Quantum Electronics **25**(1), 1–8 (2018).

126. I. Hariri, A. Sadr, S. Nakashima, Y. Shimada, J. Tagami, and Y. Sumi, "Estimation of the enamel and dentin mineral content from the refractive index," Caries research **47**(1), 18–26 (2013).

127. P. Tang, N. Le, J. Lu, K.-H. Chung, H. Subhash, L. Kilpatrick-Liverman, and R. K. Wang, "Local axis orientation mapped by polarization sensitive optical coherence tomography provides a unique contrast to identify caries lesions in enamel," Biomed. Opt. Express **13**(8), 4247 (2022).

128. H. Nakagawa, A. Sadr, Y. Shimada, J. Tagami, and Y. Sumi, "Validation of swept source optical coherence tomography (SS-OCT) for the diagnosis of smooth surface caries in vitro," Journal of dentistry **41**(1), 80–89 (2013).

129. B. W. Colston, M. J. Everett, L. B. Da Silva, L. L. Otis, P. Stroeve, and H. Nathel, "Imaging of hard-and soft-tissue structure in the oral cavity by optical coherence tomography," Applied Optics **37**(16), 3582–3585 (1998).

130. D. Di Stasio, D. Lauritano, F. Loffredo, E. Gentile, F. Della Vella, M. Petruzzi, and A. Lucchese, "Optical coherence tomography imaging of oral mucosa bullous diseases: a preliminary study," Dentomaxillofacial Radiology **49**(2), 20190071 (2020).

131. M. DeCoro and P. Wilder-Smith, "Potential of optical coherence tomography for early diagnosis of oral malignancies," Expert review of anticancer therapy **10**(3), 321–329 (2010).

132. Y. Shimada, H. Nakagawa, A. Sadr, I. Wada, M. Nakajima, T. Nikaido, M. Otsuki, J. Tagami, and Y. Sumi, "Noninvasive cross-sectional imaging of proximal caries using swept-source optical coherence tomography (SS-OCT) *in vivo*," Journal of biophotonics **7**(7), 506–513 (2014).

133. Y. Shimada, A. Sadr, A. Nazari, H. Nakagawa, M. Otsuki, J. Tagami, and Y. Sumi, "3D evaluation of composite resin restoration at practical training using swept-source optical coherence tomography (SS-OCT)," Dental materials journal **31**(3), 409–417 (2012).

134. S. Moon and Z. Chen, "Phase-stability optimization of swept-source optical coherence tomography," Biomedical optics express **9**(11), 5280–5295 (2018).

135. X. Attendu, R. M. Ruis, C. Boudoux, T. G. Van Leeuwen, and D. J. Faber, "Simple and robust calibration procedure for k-linearization and dispersion

compensation in optical coherence tomography," Journal of biomedical optics **24**(5), 056001–056001 (2019).

136. M. Wojtkowski, V. J. Srinivasan, T. H. Ko, J. G. Fujimoto, A. Kowalczyk, and J. S. Duker, "Ultrahigh-resolution, high-speed, Fourier domain optical coherence tomography and methods for dispersion compensation," Optics express **12**(11), 2404–2422 (2004).

137. R.-A. Erdelyi, V.-F. Duma, C. Sinescu, G. M. Dobre, A. Bradu, and A. Podoleanu, "Optimization of X-ray investigations in dentistry using optical coherence tomography," Sensors **21**(13), 4554 (2021).

138. Y. Li, P. Tang, S. Song, A. Rakymzhan, and R. K. Wang, "Electrically tunable lens integrated with optical coherence tomography angiography for cerebral blood flow imaging in deep cortical layers in mice," Optics letters **44**(20), 5037–5040 (2019).

139. Y. K. Tao, S. K. Srivastava, and J. P. Ehlers, "Microscope-integrated intraoperative OCT with electrically tunable focus and heads-up display for imaging of ophthalmic surgical maneuvers," Biomedical optics express **5**(6), 1877–1885 (2014).

140. J. P. McLean and C. P. Hendon, "3-D compressed sensing optical coherence tomography using predictive coding," Biomedical Optics Express **12**(4), 2531–2549 (2021).

141. J. Xu, C. Zhang, J. Xu, K. Wong, and K. Tsia, "Megahertz all-optical swept-source optical coherence tomography based on broadband amplified optical time-stretch," Optics letters **39**(3), 622–625 (2014).

142. L. Waszczuk, J. Ogien, J.-L. Perrot, and A. Dubois, "Co-localized line-field confocal optical coherence tomography and confocal Raman microspectroscopy for three-dimensional high-resolution morphological and molecular characterization of skin tissues ex vivo," Biomedical optics express **13**(4), 2467–2487 (2022).

143. J. Liao, S. Yang, T. Zhang, C. Li, and Z. Huang, "Fast optical coherence tomography angiography image acquisition and reconstruction pipeline for skin application," Biomedical Optics Express **14**(8), 3899–3913 (2023).

144. S.-H. Kim, J. Kim, S. Yang, S.-H. Oh, S.-P. Lee, H. J. Yang, T.-I. Kim, and W.-J. Yi, "Automatic and quantitative measurement of alveolar bone level in OCT images using deep learning," Biomedical Optics Express **13**(10), 5468–5482 (2022).

145. J. Grundmann, J. Golde, S. Steuer, F. Tetschke, L. Kirsten, J. Walther, E. Koch, and C. Hannig, "Visualization of carious lesions with polarized and depolarized light microscopy," Biomedical Optics Express **15**(5), 3018–3036 (2024).

146. S. P. Hsu, M.-H. Lin, C.-F. Lin, T.-Y. Hsiao, Y.-M. Wang, and C.-W. Sun, "Brain tumor grading diagnosis using transfer learning based on optical coherence tomography," Biomedical Optics Express **15**(4), 2343–2357 (2024).

147. T.-A. Wang, M.-C. Chan, H.-C. Lee, C.-Y. Lee, and M.-T. Tsai, "Ultrahigh-resolution optical coherence tomography/angiography with an economic and compact supercontinuum laser," Biomedical Optics Express **10**(11), 5687–5702 (2019).

148. I. Grulkowski, J. J. Liu, B. Potsaid, V. Jayaraman, C. D. Lu, J. Jiang, A. E. Cable, J. S. Duker, and J. G. Fujimoto, "Retinal, anterior segment and full eye imaging using ultrahigh speed swept source OCT with vertical-cavity surface emitting lasers," Biomedical optics express **3**(11), 2733–2751 (2012).

149. V. S. Diogo, H. A. Ferreira, D. Prata, and A. D. N. Initiative, "Early diagnosis of Alzheimer's disease using machine learning: a multi-diagnostic, generalizable approach," Alzheimer's Research & Therapy **14**(1), 107 (2022).

150. J. Xu, S. Song, S. Men, and R. K. Wang, "Long ranging swept-source optical coherence tomography-based angiography outperforms its spectral-domain counterpart in imaging human skin microcirculations," Journal of biomedical optics **22**(11), 116007–116007 (2017).

151. S. Aumann, S. Donner, J. Fischer, and F. Müller, "Optical Coherence Tomography (OCT): Principle and Technical Realization," in *High Resolution Imaging in Microscopy and Ophthalmology*, J. F. Bille, ed. (Springer International Publishing, 2019), pp. 59–85.

152. A. Agrawal, T. J. Pfefer, P. D. Woolliams, P. H. Tomlins, and G. Nehmetallah, "Methods to assess sensitivity of optical coherence tomography systems," Biomed Opt Express **8**(2), 902–917 (2017).

153. P. Ortiz, M. Draelos, R. P. McNabb, A. N. Kuo, and J. Izatt, "Autofocusing and autoaligning robotic optical coherence tomography," Investigative Ophthalmology & Visual Science **62**(8), 2555–2555 (2021).

154. S. Donner, S. Bleeker, T. Ripken, M. Ptok, M. Jungheim, and A. Krueger, "Automated working distance adjustment enables optical coherence tomography of the human larynx in awake patients," Journal of Medical Imaging **2**(2), 026003–026003 (2015).

155. J. P. Su, Y. Li, M. Tang, L. Liu, A. D. Pechauer, D. Huang, and G. Liu, "Imaging the anterior eye with dynamic-focus swept-source optical coherence tomography," Journal of biomedical optics **20**(12), 126002–126002 (2015).

156. I. Grulkowski, K. Szulzycki, and M. Wojtkowski, "Microscopic OCT imaging with focus extension by ultrahigh-speed acousto-optic tunable lens and stroboscopic illumination," Optics Express **22**(26), 31746–31760 (2014).

157. S. T. Hsu, H. Gabr, C. Viehland, K. Sleiman, H. T. Ngo, O. M. Carrasco-Zevallos, L. Vajzovic, R. P. McNabb, S. S. Stinnett, J. A. Izatt, and others, "Volumetric measurement of subretinal blebs using microscope-integrated optical coherence tomography," Translational Vision Science & Technology **7**(2), 19–19 (2018).

158. D. J. Faber, F. J. Van Der Meer, M. C. Aalders, and T. G. van Leeuwen, "Quantitative measurement of attenuation coefficients of weakly scattering media using optical coherence tomography," Optics express **12**(19), 4353–4365 (2004).

159. R. Nedelcu, P. Olsson, I. Nyström, J. Rydén, and A. Thor, "Accuracy and precision of 3 intraoral scanners and accuracy of conventional impressions: A novel *in vivo* analysis method," Journal of dentistry **69**, 110–118 (2018).

160. T. Robinson, F. Consoli, S. Giltrap, S. Eardley, G. Hicks, E. Ditter, O. Ettlinger, N. Stuart, M. Notley, R. De Angelis, and others, "Low-noise time-resolved optical sensing of electromagnetic pulses from petawatt laser-matter interactions," Scientific reports **7**(1), 983 (2017).

161. G. Shan, Y. Li, L. Zhang, Z. Wang, Y. Zhang, and J. Qian, "Contributed Review: Application of voice coil motors in high-precision positioning stages with large travel ranges," Review of Scientific Instruments **86**(10), (2015).

162. M. C. Estevez, M. Alvarez, and L. M. Lechuga, "Integrated optical devices for lab-on-a-chip biosensing applications," Laser & Photonics Reviews **6**(4), 463–487 (2012).

163. K. Luke, P. Kharel, C. Reimer, L. He, M. Loncar, and M. Zhang, "Wafer-scale low-loss lithium niobate photonic integrated circuits," Optics Express **28**(17), 24452–24458 (2020).

164. Z. Gong, Y. Shi, J. Liu, R. Sabesan, and R. K. Wang, "Light-adapted flicker-optoretinography based on raster-scan optical coherence tomography towards clinical translation," Biomedical Optics Express **15**(10), 6036–6051 (2024).

165. S. Lotz, M. Göb, S. Böttger, L. Ha-Wissel, J. Hundt, F. Ernst, and R. Huber, "Large area robotically assisted optical coherence tomography (LARA-OCT)," Biomedical Optics Express **15**(6), 3993–4009 (2024).

166. A. K. Badhey, J. S. Schwarz, B. M. Laitman, B. M. Veremis, W. H. Westra, M. Yao, M. S. Teng, E. M. Genden, and B. A. Miles, "Intraoperative Use of Wide-Field Optical Coherence Tomography to Evaluate Tissue Microstructure in the Oral Cavity and Oropharynx," JAMA Otolaryngology–Head & Neck Surgery **149**(1), 71–78 (2023).

167. Y. Shi, J. Liu, and R. K. Wang, "High-speed, long-range and wide-field OCT for *in vivo* 3D imaging of the oral cavity achieved by a 600 kHz swept source laser," Biomedical Optics Express **15**(7), 4365–4380 (2024).

168. J. Tian, C. Li, Z. Qin, Y. Zhang, Q. Xu, Y. Zheng, X. Meng, P. Zhao, K. Li, S. Zhao, and others, "Coronary artery calcification and cardiovascular outcome as assessed by intravascular OCT and artificial intelligence," Biomedical Optics Express **15**(8), 4438–4452 (2024).

169. Z. Gong, Y. Shi, J. Liu, Y. Zhang, M. A. Johnstone, and R. K. Wang, "Volumetric imaging of trabecular meshwork dynamic motion using 600 kHz swept source optical coherence tomography," Biomedical Optics Express **16**(1), 267–281 (2024).

170. B. Baumann, "Polarization sensitive optical coherence tomography: a review of technology and applications," Applied Sciences **7**(5), 474 (2017).

171. P. Tang and R. K. Wang, "Polarization state tracing method to map local birefringent properties in samples using polarization sensitive optical coherence tomography," Biomedical Optics Express **11**(12), 6852–6863 (2020).

172. T. Louie, C. Lee, D. Hsu, K. Hirasuna, S. Manesh, M. Staninec, C. L. Darling, and D. Fried, "Clinical assessment of early tooth demineralization using polarization sensitive optical coherence tomography," Lasers in surgery and medicine **42**(10), 898–905 (2010).

173. M. Pircher, C. K. Hitzenberger, and U. Schmidt-Erfurth, "Polarization sensitive optical coherence tomography in the human eye," Progress in retinal and eye research **30**(6), 431–451 (2011).

174. R. R. Parakkel, D. Wong, C. Li, J. Cheong, M. E. Nongpiur, R. S. Chong, T. Aung, L. Schmetterer, X. Liu, and J. Chua, "Retinal nerve fiber layer damage assessment in glaucomatous eyes using retinal retardance measured by polarization-sensitive optical coherence tomography," Translational Vision Science & Technology **13**(5), 9–9 (2024).

175. E. Marjanovic, V. Sharma, L. Smith, C. Pinder, T. Moore, J. Manning, G. Dinsdale, M. Berks, V. Newton, S. Wilkinson, and others, "Polarisation-sensitive optical coherence tomography measurement of retardance in fibrosis, a non-invasive biomarker in patients with systemic sclerosis," Scientific Reports **12**(1), 2893 (2022).

176. M. Vaselli, K. Kalverda-Mooij, E. Thunnissen, M. W. Tanck, O. M. Mets, I. A. Van Den Berk, J. T. Annema, P. I. Bonta, and J. F. De Boer, "*In vivo* polarisation sensitive optical coherence tomography for fibrosis assessment in interstitial lung disease: a prospective, exploratory, observational study," BMJ open respiratory research **10**(1), e001628 (2023).

177. J. F. de Boer, C. K. Hitzenberger, and Y. Yasuno, "Polarization sensitive optical coherence tomography – a review [Invited]," Biomed. Opt. Express, BOE **8**(3), 1838–1873 (2017).

178. W. Trasischker, S. Zotter, T. Torzicky, B. Baumann, R. Haindl, M. Pircher, and C. K. Hitzenberger, "Single input state polarization sensitive swept source optical coherence tomography based on an all single mode fiber interferometer," Biomed. Opt. Express, BOE **5**(8), 2798–2809 (2014).

179. Z. Ding, C.-P. Liang, Q. Tang, and Y. Chen, "Quantitative single-mode fiber based PS-OCT with single input polarization state using Mueller matrix," Biomed. Opt. Express, BOE **6**(5), 1828–1843 (2015).

180. S. Moon, Y. Miao, and Z. Chen, "Fiber-based polarization-sensitive optical coherence tomography of a minimalistic system configuration," Optics Letters, Vol. 44, Issue 12, pp. 3150-3153 (2019).

181. S. Li, L. Hu, and J. Cao, "High-Sensitivity Polarization Sensitive Optical Coherence Tomography Based on Numerical Correction for Perfect Circularly Polarized Light," Applied Sciences **14**(6), 2525 (2024).

182. K. L. Lurie, T. J. Moritz, and A. K. Ellerbee, "Design considerations for polarization-sensitive optical coherence tomography with a single input polarization state," Biomed. Opt. Express, BOE **3**(9), 2273–2287 (2012).

183. P. Tang, R. K. Wang, and Q. Chao, "Digital calibration method to enable depth-resolved all-fiber polarization sensitive optical coherence tomography with an arbitrary input polarization state," Biomed. Opt. Express, BOE **15**(5), 3329–3343 (2024).

184. B. Braaf, K. A. Vermeer, M. de Groot, K. V. Vienola, and J. F. de Boer, "Fiber-based polarization-sensitive OCT of the human retina with correction of system polarization distortions," Biomed. Opt. Express, BOE **5**(8), 2736–2758 (2014).

185. Z. Wang, H.-C. Lee, O. O. Ahsen, B. Lee, W. Choi, B. Potsaid, J. Liu, V. Jayaraman, A. Cable, M. F. Kraus, K. Liang, J. Hornegger, and J. G. Fujimoto, "Depth-encoded all-fiber swept source polarization sensitive OCT," Biomed. Opt. Express, BOE **5**(9), 2931–2949 (2014).

186. M. Villiger, E. Z. Zhang, S. K. Nadkarni, W.-Y. Oh, B. J. Vakoc, and B. E. Bouma, "Spectral binning for mitigation of polarization mode dispersion artifacts in catheter-based optical frequency domain imaging," Opt. Express, OE **21**(14), 16353–16369 (2013).

187. J. Liu, Y. Shi, Z. Gong, Y. Zhang, and R. K. Wang, "Adaptive contour-tracking to aid wide-field swept-source optical coherence tomography imaging of large objects with uneven surface topology," Biomedical Optics Express **15**(8), 4891–4908 (2024).

188. J. P. Gordon and H. Kogelnik, "PMD fundamentals: Polarization mode dispersion in optical fibers," Proceedings of the National Academy of Sciences **97**(9), 4541–4550 (2000).

189. B. Baumann and A. Wöhrer, "Polarization-insensitive optical coherence tomography based on partly depolarized light," Opt. Lett., OL **48**(13), 3499–3502 (2023).

190. J. F. De Boer and T. E. Milner, "Review of polarization sensitive optical coherence tomography and Stokes vector determination," Journal of biomedical optics **7**(3), 359–371 (2002).

191. P. Tang, M. A. Kirby, N. Le, Y. Li, N. Zeinstra, G. N. Lu, C. E. Murry, Y. Zheng, and R. K. Wang, "Polarization sensitive optical coherence tomography with single

input for imaging depth-resolved collagen organizations," Light: Science & Applications **10**(1), 237 (2021).

192. N. T. IPLINSKY, L. G. GANDINI, A. S. GANDINI, A. T. BAGATINI, P. H. J. de OLIVEIRA, P. C. H. da SILVA, and A. SANTOS-PINTO, "Radiographic evaluation of enamel thickness of permanent teeth: relevance and applicability," Dental Press J Orthod **29**(3), e242422 (n.d.).

193. M. Wang, Y. Ling, Z. Dong, X. Yao, Y. Gan, C. Zhou, and Y. Su, "GPU-accelerated iterative method for FD-OCT image reconstruction with an image-level cross-domain regularizer," Opt. Express, OE **31**(2), 1813–1831 (2023).

194. Y. Huang, X. Li, J. Liu, Z. Qiao, J. Chen, and Q. Hao, "Robotic-arm-assisted flexible large field-of-view optical coherence tomography," Biomed. Opt. Express, BOE **12**(7), 4596–4609 (2021).

195. X. Li, Y. Huang, and Q. Hao, "Automated robot-assisted wide-field optical coherence tomography using structured light camera," Biomed. Opt. Express, BOE **14**(8), 4310–4325 (2023).

196. S. Cao, X. Yao, N. Koirala, B. Brott, S. Litovsky, Y. Ling, and Y. Gan, "Super-resolution technology to simultaneously improve optical & digital resolution of optical coherence tomography via deep learning," Annu Int Conf IEEE Eng Med Biol Soc **2020**, 1879–1882 (2020).

197. W. Lee, H. S. Nam, J. Y. Seok, W.-Y. Oh, J. W. Kim, and H. Yoo, "Deep learning-based image enhancement in optical coherence tomography by exploiting interference fringe," Communications Biology **6**(1), 464 (2023).

APPENDICES